March 2002 • NREL/ SR-520-31777

Subcontractor Report

Process Development and Basic Studies of Electrochemically Deposited CdTe-Based Solar Cells

Final Technical Report
15 May 1998—17 August 2001

V.I. Kaydanov and T.R. Ohno
Colorado School of Mines
Golden, Colorado

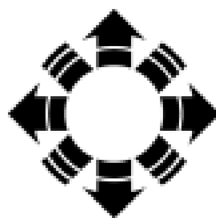

National Renewable Energy Laboratory

1617 Cole Boulevard
Golden, Colorado 80401-3393

NREL is a U.S. Department of Energy Laboratory
Operated by Midwest Research Institute • Battelle • Bechtel

Contract No. DE-AC36-99-GO10337

March 2002 • NREL/ SR-520-31777

Process Development and Basic Studies of Electrochemically Deposited CdTe-Based Solar Cells

Final Technical Report
15 May 1998—17 August 2001

V.I. Kaydanov and T.R. Ohno
Colorado School of Mines
Golden, Colorado

NREL Technical Monitor: Bolko von Roedern

Prepared under Subcontract No. XAK-8-17619-28

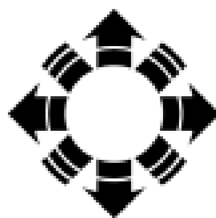

NREL

National Renewable Energy Laboratory

1617 Cole Boulevard
Golden, Colorado 80401-3393

NREL is a U.S. Department of Energy Laboratory
Operated by Midwest Research Institute • Battelle • Bechtel

Contract No. DE-AC36-99-GO10337

NOTICE

This report was prepared as an account of work sponsored by an agency of the United States government. Neither the United States government nor any agency thereof, nor any of their employees, makes any warranty, express or implied, or assumes any legal liability or responsibility for the accuracy, completeness, or usefulness of any information, apparatus, product, or process disclosed, or represents that its use would not infringe privately owned rights. Reference herein to any specific commercial product, process, or service by trade name, trademark, manufacturer, or otherwise does not necessarily constitute or imply its endorsement, recommendation, or favoring by the United States government or any agency thereof. The views and opinions of authors expressed herein do not necessarily state or reflect those of the United States government or any agency thereof.

Available electronically at http://www.osti.gov/bridge

Available for a processing fee to U.S. Department of Energy
and its contractors, in paper, from:

U.S. Department of Energy
Office of Scientific and Technical Information
P.O. Box 62
Oak Ridge, TN 37831-0062
phone: 865.576.8401
fax: 865.576.5728
email: reports@adonis.osti.gov

Available for sale to the public, in paper, from:

U.S. Department of Commerce
National Technical Information Service
5285 Port Royal Road
Springfield, VA 22161
phone: 800.553.6847
fax: 703.605.6900
email: orders@ntis.fedworld.gov
online ordering: http://www.ntis.gov/ordering.htm

Printed on paper containing at least 50% wastepaper, including 20% postconsumer waste

PREFACE

This project, “Process Development and Basic Studies of Electrochemically Deposited CdTe-Based Solar Cells”, which has been conducted at the Colorado School of Mines (CSM), is part of the NREL Thin-Film Partnership Program. The project addresses long-term research and development issues related to polycrystalline thin-film solar cells. Our general research approach is based on combining activities aimed at improvement of cell performance and stability with activities aimed at increasing our fundamental understanding of the properties of materials making up the cells: CdTe, CdS, multi-layer back contact, and transparent conducting oxide (TCO) front contact. We emphasize the relation between structural and electronic material properties and various processing procedures as well as the microscopic mechanisms responsible for the cell performance and its degradation.

There is a lack of knowledge and understanding of basic issues behind the CdTe/CdS cell performance and stability, such as the nature and electronic properties of impurities and defects that control the majority carrier concentration, mechanisms of the dopant compensation, recombination centers, their nature and properties, diffusion, electromigration and transformation of defects under various processing, stress, and operating conditions, etc. We believe that better basic understanding of the specific influence of polycrystallinity, especially for fine-grain materials characteristic of CdTe-based cells, is now one of the most important issues we must address. We need to clarify the role of grain boundaries (GB) in forming the film electronic properties as well as those of the p-n junction. It is important to study and understand the influence of the GB boundaries on the spatial distribution and migration of impurities and electrically active defects. To fulfill these tasks one needs to develop new methods and techniques (or adjust existing ones) for material characterization as well as more sophisticated approaches to the data analysis and modeling. This report presents studies relevant to the problems formulated above that were carried out at CSM during this project according to the Statement of Work and Tasks of the Subcontract.

Section 1 presents studies of CdTe films using the in-plane electrical characterization Impedance spectroscopy (IS) films - measurements of the complex impedance in a wide frequency range. These were aimed at studies of electronic properties of grain boundaries (GB). Validity of various physical and electrical models for the impedance analysis are discussed. Experimental studies demonstrated the presence of a potential barrier for holes in the GB region, which is responsible for a very high electrical resistance of films that depends exponentially on the barrier height. Lowering of the barrier under illumination provides a significant photoconductivity effect. It was shown that the space charge density (SCD) in the vicinity of GB was orders of magnitude greater than the grain bulk SCD. A high density of GB electronic states was estimated based on the bias-dependent capacitance measurements. It was found that the GB electronic properties depend on processing technology. The second part of the section presents Hall concentration and mobility studies. Combined Hall and IS measurements under varying illumination intensity (photo-Hall and photo-IS) reduced the GB influence and provided more realistic estimates of hole concentration and mobility in the grain bulk. In films with reduced hole concentration Hall effect is significantly influenced by photogenerated carriers which enabled estimation of electron mobility and effective lifetime. Using higher light intensities the same estimates could be made for the films in a practical doping level range ($\sim10^{14}$-10^{15} cm^{-3}).

Studies of band spectrum and electron scattering in transparent conducting oxides are presented in Section 2. We discuss here details and parameters of the spectrum and scattering that relate to the figure of merit for TCOs, formulate and provide theoretically basis for experimental method for their studies based on simultaneous measurements of various transport phenomena in stationary external fields and in ultrahigh frequency electromagnetic fields (optical characterization). This method provided information on the effective mass value, deviation from a parabolic spectrum, the shape of constant-energy surfaces, dominating scattering mechanism, and also contribution of grain boundaries to the film sheet resistance. A brief description of the principal features of the measurement equipment and experimental procedure are also presented in this section.

Studies of spectral dependencies of photocurrent and its spatial distribution over the cross section of the electrodeposited (ED) CdTe cell were performed using the near field scanning optical microscopy (NSOM) (Sec. 3). The instrumentation provided spatial resolution of ~1000 Å which was sufficient for revealing and mapping non-uniformities caused by the fine-granular structure of the CdTe absorber layer. Dependence of the $CdTe_{1-x}S_x$ bandgap on S composition enabled the microscopic identification of S-rich regions in the CdTe layer by combining NSOM with a tunable laser. S composition was found to be very non-uniform and greater along grain boundaries than in the grain centers, identifying grain boundaries as locations of enhanced interdiffusion. In some cross-sectional photocurrent images, enhancements in photocurrent were observed near grain boundaries for the photon energies not only below but also well above the CdTe bandgap. This non-trivial effect may provide some guidance about the complex influence of grain boundaries on cell performance.

Section 4 presents studies of deep traps in CdTe cells using DLTS (in collaboration with NREL) and admittance spectroscopy (AS) techniques. Cells were also characterized with J-V, C-V, C(V,T), C(V, f) measurements. It was found that the C-V profile changes significantly with temperature. Two possible mechanisms behind these changes were discussed: the temperature dependence of the free hole concentration, and high concentration of deep traps, whose contribution to the measured capacitance increases with temperature. One deep trap for electrons and four traps for holes were detected by DLTS studies. Concentration of traps is comparable to the free hole concentration detected by C-V measurements and depends strongly on the temperature of the Cu post-deposition annealing temperature. The latter also influences Cu concentration detected by SIMS measurements. It was found that the minority-carrier lifetime reduces with increasing concentration of Cu and of the traps located close to midgap. Admittance spectroscopy also revealed at least two single-level (or narrow-band) traps as well as a band (or bands) of very slow (hence deep) traps. The latter could be attributed to the GB electronic states. AS results also indicate high concentration of deep traps, probably exceeding the "C-V doping level".

Section 5 presents studies of degradation under stress conditions of the cells with differently processed CdTe and different back contacts. We compared cells based on CdTe prepared by First Solar, LLC, and on CdTe electrodeposited at CSM. Back contacts were of two types: Cu/ZnTe/Au and Cu/Au. It was shown that under the same stress conditions the degradation of the cell parameters occurs significantly different for the cells with differently prepared CdTe as

well as for different back contacts. Degradation of cells was accompanied and caused, at least partially, by significant changes in the cell doping profile, which probably indicates spatial redistribution of electrically active defects and very likely non-uniform changes in compensation degree. A strong influence of bias applied during stressing on the doping profile indicates a significant contribution of electromigration to this and perhaps to transformation of the defects in strong built-in electric fields. The section is concluded with an analysis of the problems to be addressed in continuing studies aimed at clarification of the degradation mechanisms and possible technical approaches to their solution.

Appendices present data on personnel involved in the studies, laboratory improvements, publications and presentations for the project period.

TABLE OF CONTENTS

PREFACE 3

TABLE OF CONTENTS 6
LIST OF FIGURES 9
LIST OF TABLES 10

1. ELECRONIC PROPERTIES OF Thin CdTe FILMS
   1.1 Impedance Spectroscopy of Grain Boundaries 11
      1.1.1 Physical and electrical models 11
      1.1.2 Experimental. Technical problems of measurement 16
      1.1.3 Major results of the GB studies 18
      1.1.4 Conclusions 20
   1.2 Hall Effect in Thin CdTe Polycrystalline Films 21
      1.2.1 Experimental details 21
      1.2.2 Measurements and discussion 22
      1.2.3 Conclusions 26

2. BASIC ELECTRONIC PROPERTIES OF THIN FILM TRANSPARENT CONDUCTIVE OXIDES
   2.1 Introduction 27
   2.2 Electron Parameters to be Determined 27
      2.2.1 Band model, the effective mass tensor, and density of states 27
      2.2.2 Carrier scattering, relaxation time, scattering parameter 30
      2.2.3 Influence of non-parabolicity 31
   2.3. Formulation of Experimental Methods
      2.3.1 Method of four coefficients (electron transport in stationary external fields) 33
      2.3.2 Optical characterization (ultra-high frequency electron transport) 36
      2.3.3 Evaluation of the grain boundary contribution to the film sheet resistance 37
   2.4 Experimental Studies of Thin TCO Films
      2.4.1 Tin oxide films doped with fluorine 39
      2.4.2 Application of the four-coefficient method. ZnO films 43
   2.5 Conclusions 46

3. NEAR FIELD SCANNING OPTICAL MICROSCOPY (NSOM) OF CdTe/CdS SOLAR CELLS
   3.1 Experimental Techniques and Procedures 47
   3.2 Experimental Results and Discussion 48
   3.3. Conclusions ` 52

4. DEEP TRAPS IN CdTe SOLAR CELLS 53
4.1 DLTS Studies of ED CdTe/CdS cells 53
4.2 Admittance Spectroscopy of Deep Traps in CdTe/CdS Solar Cells 60
4.3 Conclusions....................64

5. STUDY OF CELL DEGRADATION UNDER STRESS CONDITIONS
5.1 Stressing of Cells with the Vapor Transport Deposited CdTe and Cu/ZnTe/Au Back Contact 65
5.2 Comparison of Degradation in VaporTransport- and Electrodeposited CdTe Solar Cells with Cu/ZnTe/Au and Cu/Au Back Contacts 70
5.3 Discussion
5.3.1 Major results of this study. Role of electromigration 73
5.3.2 Some basic problems behind degradation mechanisms and possible approaches to their solution 74

6. REFERENCES 80

7. ACKNOWLEDGEMENTS.................... 85

8. APPENDICES
8.1 Personnel....................86
8.2 Laboratory Improvements....................88
8.3 Publications/Presentations. 89

LIST OF FIGURES

Figure 1.1 The simplest electrical model of a polycrystalline film 11

Figure 1.2 Experimental results for resistance of a CdTe layer in comparison with calculations 12

Figure 1.3 Measured and calculated capacitance for a CdTe layer................................13

Figure 1.4 Electrical model that includes capacitance of the intragrain material 14

Figure 1.5 Effect of bias voltage on measured film resistance and capacitance.............15

Figure 1.6 Modified electrical model for the polycrystalline film 16

Figure 1.7 Comparison of the frequency dependencies of R_p and R_s measured on CdTe film in dark and in light 18

Figure 1.8 Dependence of the GB “oscillating” capacitance on bias voltage between probes 20

Figure 1.9 Block diagram of a polycrystalline film with regularly arranged square shaped grains separated by GB regions of high resistivity 23

Figure 1.10 Dependence of Hall concentration and mobility on the GB region resistance and size 24

Figure 1.11 Dependence of Hall concentration and mobility on concentration of photogenerated electrons 25

Figure 2.1 Dependence of plasma frequency (a) and Seebeck coefficient (b) on electron concentration 40

Figure 2.2 Comparison of two types of geometry used for the N-E effect measurements. 44

Figure 3.1 Topography (a) and photocurrent (b-d) NSOM images taken on the cross section of a CdS/CdTe solar cell 49

Figure 3.2 The plot showing line traces taken from single scans across the grain outlined in Figure 3.1 51

Figure 4.1 The carrier concentration profile measured at room temperature for various post-Cu annealing temperatures 54

Figure 4.2 The carrier concentration-depth profile in the cell "150" as a function of temperature 55

Figure 4.3 SIMS data on the Cu concentration profile in the CdTe/CdS solar cells with the Cu/Au back contact annealed at different temperatures 59

Figure 4.4 Capacitance and conductance of a cell with the Cu/Au back contact measured at room temperature 62

Figure 4.5 The (dG/df) –f plot demonstrates two or maybe three peaks related to different trap states 63

Figure 5.1 Degradation of efficiency of various cells under FB and RB conditions 71

Figure 5.2 Changes in fill factor (FF) and open circuit voltage (V_{oc}) after stressing for 110 hours 72

Figure 5.3 Changes in doping profile for the FS-ZnTe and CSM (ED) cells after 110 hours of stressing 73

LIST OF TABLES

Table 1.1 Parameters measured and calculated for the CdTe:Cu film at different light intensities 22

Table 2.1 Comparison of the Hall and optical mobility values 41

Table 4.1 Device performance vs. Cu annealing temperature 53

Table 4.2 The trap levels and concentrations 57

Table 4.3 Lifetime determined using TRPL in dependence on the post-Cu annealing temperature 59

Table 5.1 Changes in the cell parameters as a function of the stress test conditions and length (duration) 66

Table 5.2 Stress tests under varied bias 69

1. ELECTRONIC PROPERTIES OF THIN CdTe FILMS

1.1 Impedance Spectroscopy of Grain Boundaries

Measurements of the complex impedance on polycrystalline films in a wide frequency range (impedance spectroscopy) are aimed at studies of electronic properties of grain boundaries (GB). These measurements characterize properties of a film as a whole. Then, based on some physical and electrical models we extract from these measurements the parameters averaged over numerous grain boundaries in a sample. The validity of the models used must always be examined. We need to analyze conditions under which a particular model is valid or at least provides reasonably small errors in the parameter estimates derived from the measurements.
In this section we present and discuss:

- physical and electrical models we use;
- issues related to the experimental techniques and procedures;
- some results obtained on CdTe thin films.

1.1.1 Physical and electrical models

<u>*The simplest model*</u>

The basic idea of the method is that a polycrystalline film is a two-phase material with very distinct electrical properties of each phases. One phase is the intragrain (IG) material and the other is represented by the GB regions with the potential barriers for the majority carriers. The GB is characterized by high resistance for the grain-to-grain carrier transport and also by capacitance provided by depleted semi-insulating layers adjacent to the GB. The grain is assumed to be electrically equivalent to a resistor, R_{IG}, whereas the GB is electrically modeled as a resistor, R_{GB}, in parallel with a capacitor, C_{GB} (Fig. 1.1). At low frequencies the film impedance is almost totally defined by the GB resistance. At high frequencies the GB capacitor effectively shunts the GB resistor, so that the measured resistance tends to the IG resistance.

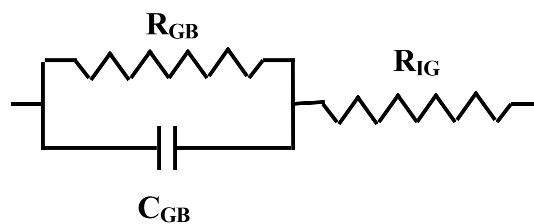

Fig. 1.1 The simplest electrical model of a polycrystalline film. Resistor R_{GB} and capacitor C_{GB} represent grain boundary. Resistor R_{IG} represents the intragrain material.

IS measurements were done with the HP4284a and HP4285a LCR meters that cover a combined frequency range of 20 Hz to 30 MHz. Data were taken and treated using a custom HP Vee program. Real and imaginary parts of impedance as a function of frequency were measured and displayed in the "s", or series, and "p", or parallel, modes. In particular, the "series resistance" represents the real part of impedance, R_s=Re(Z), and the "parallel" one the inverse of the admittance, R_p=1/Re(Y). The "series" and "parallel" capacitances relate respectively to

imaginary parts of impedance and admittance: $C_s=-[\omega Im(Z)]^{-1}$ and $C_p=Im(Y)/\omega$ where ω is the angular frequency. The data were compared to the calculated dependencies for a suitable electrical model of a film. For the electrical model in Fig. 1.1, the relations between the displayed R_p, C_p, R_s and C_s values, and the sample parameters, R_{GB}, C_{GB}, and R_{IG} are as follows:

$$R_p=R_{IG}+[R_{GB}/(1+\alpha)]\cdot\{1+\alpha/[1+(R_{IG}/R_{GB})(1+\alpha)]\} \quad (1.1)$$

$$R_s=R_{IG}+R_{GB}/(1+\alpha) \quad (1.2)$$

$$C_p=C_{GB}\cdot(1+\alpha)/\{[1+R_{IG}/R_{GB}(1+\alpha)]^2+\alpha\} \quad (1.3)$$

$$C_s=C\cdot(1+\alpha)/\alpha \quad (1.4)$$

where $\alpha=(R_{GB}C_{GB}\omega)^2$ and ω is the angular frequency.

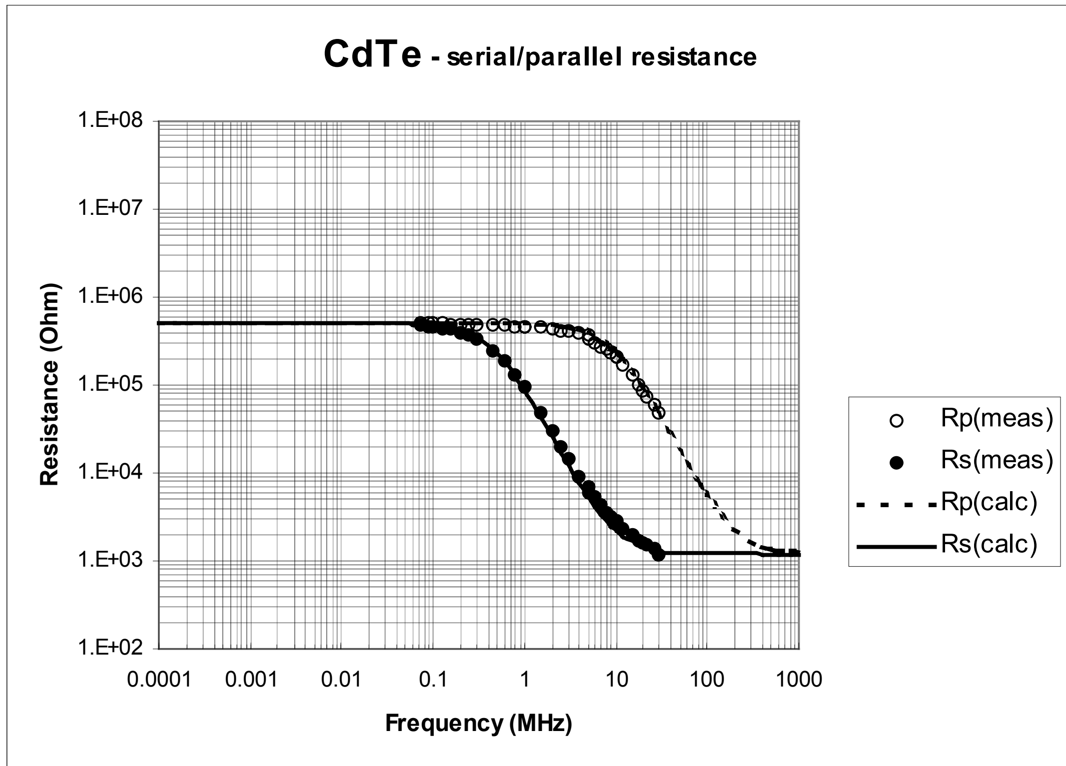

Fig. 1.2 Experimental results for resistance of a CdTe layer compared with calculations

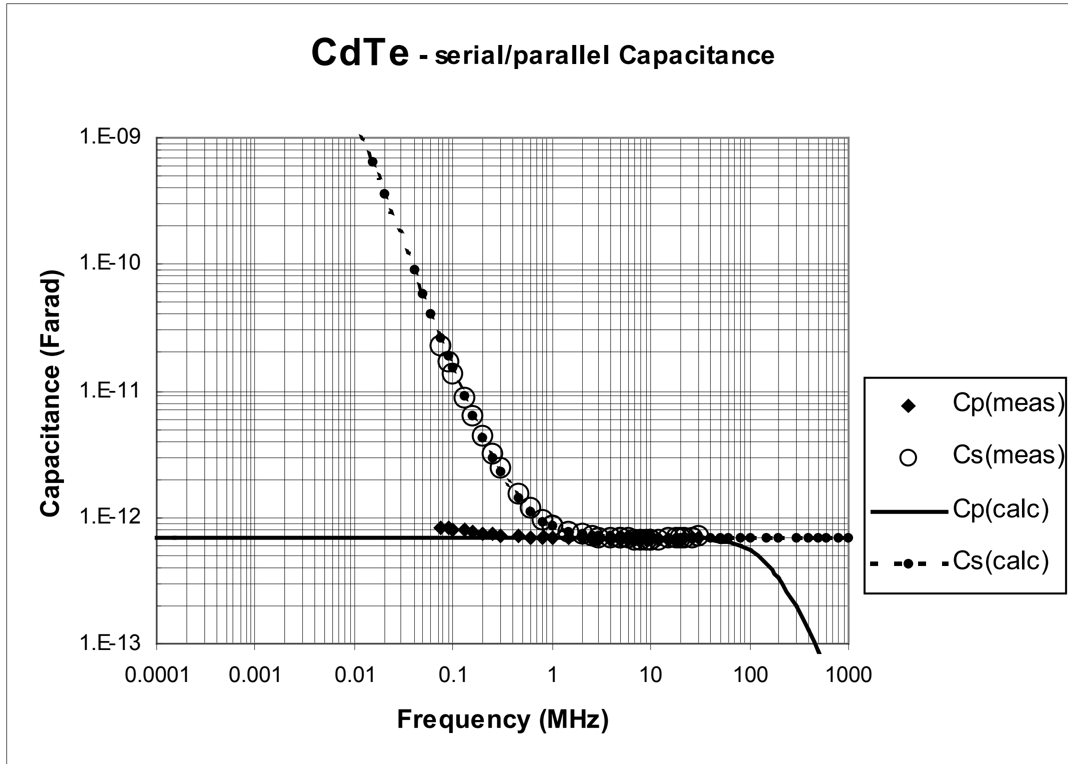

Fig.1.3 Measured and calculated capacitance for a CdTe layer

Figs. 1.2 and 1.3 show satisfactory fitting of experimental data and the dependencies calculated with Eqs. 1.1 – 1.4. In reality, the equivalent circuit of any polycrystalline sample should consist of numerous blocks like that at Fig. 1.1 connected in parallel and in series. Good fitting shows that using a single block model and "lumped" parameters is an acceptable procedure for these measurements, and a single block may represent adequately a polycrystalline sample composed of a lot of grains. The fitted results make it possible to extract lumped parameters, R_{GB}, C_{GB} and R_{IG} from the measurements. Incorporating more than one block yielded even better fits, which gives a simple means for evaluating the range of distribution of these parameters. Very good fitting was found when three blocks were incorporated with the same C_{GB} and R_{IG} values while R_{GB} values for the three blocks related to each other as 1:1.5:2. Since resistance of the GB depends exponentially on the barrier height, it may be concluded that standard deviation of the latter from the average is very small.

The same parameters, R_{GB}, C_{GB} and R_{IG}, can be provided by other frequency dependent measurements, e.g., Re(Z) and Im(Z) or |Z| and phase angle Θ. Which measurement is preferred depends on the relations between values of R_{GB}, C_{GB} and R_{IG}. A very helpful and attractive method is measurement of Im(Z) as a function of Re(Z) which yields a graph that has a semicircle shape. For the electrical circuit at Fig. 1.1, the maximum value of Im(Z) is equal to $R_{GB}/2$; intersection of the graph with the Re(Z) axis at high frequency yields the R_{IG} value, the angular frequency, ω_o, at which maximum Im(Z) is observed, provides the C_{GB} value: $C_{GB}=(R_{GB}\times\omega_o)^{-1}$.

The impedance spectroscopy method was recently proved to be effective for studies of grain boundaries in CdTe and CdS thin films on insulating substrates [1-4]. But it should be mentioned that application of the method is limited to films with high resistance grain boundaries. As seen from Eqs. 1.1 and 1.2, an effective shunting of the resistor R_{GB} by the capacitor C_{GB} takes place under condition: $\alpha=(R_{GB}C_{GB}\omega)^2 > 1$, that is when the characteristic frequency $\omega_{GB}=(R_{GB}C_{GB})^{-1}$ is smaller than the testing voltage frequency, ω.

Distributed capacitance in the grain bulk

In general, the real physical and hence electrical models should be more complex than those considered above. For example, if the grain bulk contains deep traps, they contribute to the measured capacitance due to their charging-discharging under an oscillating voltage ("oscillating capacitance"). This "oscillating" capacitance is connected in parallel to the IG resistance and may shunt it, leading to underestimation of R_{IG} and overestimation of the GB capacitance. Fig. 1.4 presents the electrical model for this case.

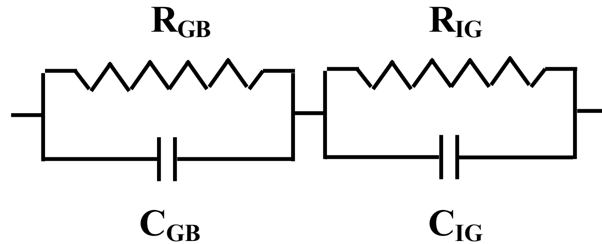

Fig. 1.4 Electrical model that includes capacitance of the intragrain material.

For most films we have studied so far $R_{IG} \ll R_{GB}$, and, according to our estimates, C_{IG} does not significantly exceed C_{GB}. That means that at intermediate and low frequencies the total measured impedance is dominated by grain boundaries. Only for frequencies above 10 MHz do we see small deviations of the measured parameters from those calculated with equations 1.1-1.4 that might be attributed to the influence of C_{IG}. This suggests that our pervious estimates of R_{IG} based on the simple model (Fig. 1.1) may not be accurate. As to the GB parameters obtained by fitting experimental and calculated data in the frequency range below 5-10 MHz, we believe they are reliable. However we had to take the effect of IG capacitance into account when studying the undoped CdTe films where the GB potential barriers were low, and the GB and IG resistances where comparable.

Oscillating capacitance of GB

We have found [3, 4] that the measured film resistance and capacitance change when a DC voltage is applied between the electrodes. As bias deviates from zero, capacitance increases and tends to saturate, and then decreases as bias voltage increases further. Dependence on bias weakens when the test signal frequency increases (see Fig. 1.5).

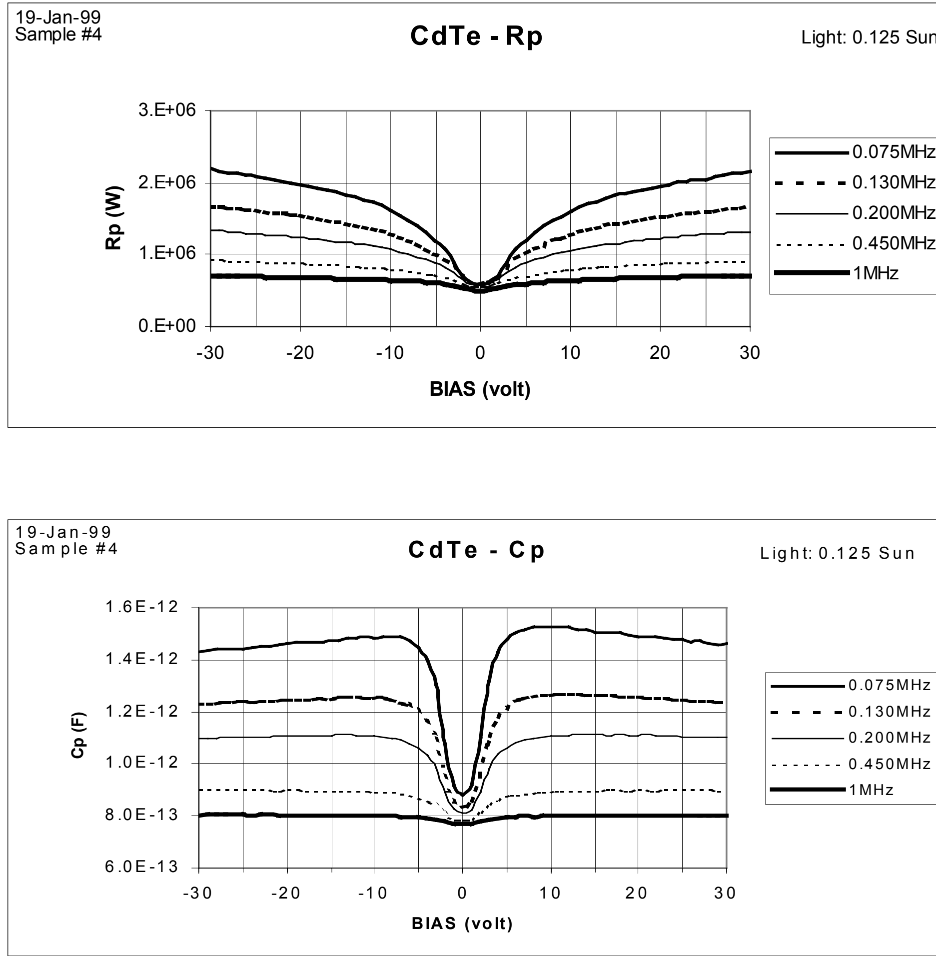

Fig. 1.5 Effect of bias voltage on measured film resistance and capacitance.

The increase of the DC resistance was explained and modeled in Ref. 10 based on the idea that under high bias the electrical charge trapped by the GB states and the GB potential barrier height increase. This in turn should lead to an increase in the GB depletion width and reduce the measured depletion capacitance. This effect was observed and discussed in [7, 8]. However a significant increase was observed in the low-frequency range on Si bicrystals with applied bias [11]. This effect was attributed to the carrier transfer between the grain and the GB traps which is out of phase with the oscillating testing voltage. Thus the total AC current is a sum of grain-to-grain and grain-to-GB currents. Accordingly, the electrical model of a grain boundary should be modified (see Fig. 1.6). The out-of-phase grain-to-GB carrier transport can be modeled with a capacitor C_T in series with a resistor R_T, which represents a finite probability for carriers incident on the GB to be trapped. The product $R_TC_T \equiv \tau_T = 1/\omega_T$ is the characteristic time of a trap (reciprocal of the characteristic frequency ω_T) and is related to the emission rate. The in-phase and out-of-phase grain-to-grain transport mechanisms are modeled respectively with a resistor $R_{G\text{-}G}$ and a capacitor $C_{G\text{-}G}$. Capacitors C_T and $C_{G\text{-}G}$ represent the oscillating and depletion capacitances of the GB, respectively.

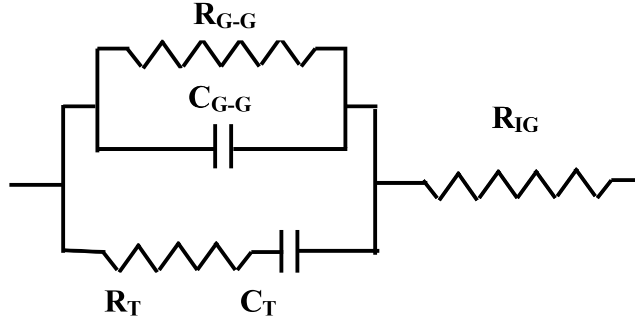

Fig. 1.6. Modified electrical model for the polycrystalline film. R_{G-G} and C_{G-G} relate to the grain to-grain electrical transport, R_T and C_T to the grain-to-GB transport; R_{IG} represents resistance of the intragrain material.

When fitting our AC measurements of CdTe films with this electrical model, it was found that R_{IG} is orders of magnitude smaller than R_{G-G} and R_T. In the frequency range of f<5MHz variation in reasonable limits does not influence the fitting value of capacitance. If we neglect R_{IG}, the capacitance value measured in "p"mode is described by equation:

$$C_p=C_{G-G}+C_T/[1+(R_TC_T\omega)^2]= C_{G-G}+C_T/[1+(\omega/\omega_T)^2] \quad (1.5)$$

For the given R_T and C_T values, the contribution of the oscillating component to the total measured capacitance decreases as the frequency increases, which allows us to separate C_{G-G} and C_T. This result is in agreement with our experimental data and also consistent with observations and discussion in [11,12]. The contribution of C_T also decreases with increase in R_T (decrease in ω_T). It was found that illumination of the sample diminishes R_T which makes the capacitance dependence on bias voltage more pronounced and easier to measure.

1.1.2 Experimental. Technical Problems of Measurement.

Samples

The measured samples are semiconductor films on insulating substrates such as glass. The sample impedance is measured in-plane with a two-electrode method. Parallel metal strips are evaporated on the surface of the semiconductor film through the mask. To provide semi-ohmic low-resistance contacts we evaporate gold on CdTe and aluminum on CdS. DC J-V characteristics measured are linear, indicating ohmic contacts. On the surface of each sample we normally evaporate six metal strips as discussed below.

LCR meters have limitations on the resistance of the tested sample. A Hewlett-Packard LCR meter Model 4285 is capable to measure and display the results if the sample resistance (real part of the impedance) does not exceed ~50 MΩ. The DC sheet resistance of the CdTe and CdS films we have measured varied in a wide range up to tens and hundreds GΩ. With increasing frequency the real part of impedance reduces (see Eqs. 1.1 and 1.2) and becomes measurable only at a higher frequency. This narrows the frequency range we can analyze and estimate the film parameters (R_{GB}, C_{GB}, etc.). To decrease the sample resistance we use a geometry factor.

The mask we use to evaporate metal electrodes provides the distance between them of 0.18mm, while the sample width (the size perpendicular to the current direction) is usually of 20 mm. This geometry reduced the sample resistance by more than two orders of magnitude as compared to the square-shaped sample configuration. By depositing several strips on the semiconductor surface, we produce several identical samples, e.g., five samples between six metal strips. When connecting the samples in parallel, we decrease the resistance by a factor of five.

Parallel connection of the individual samples increases the capacitance to be measured. This is an additional advantage of multiple metal strips. The single sample (between two neighboring strips) capacitance is rather small, usually ~1 pF. For such a small capacitance to be measured, the problem of parasitic capacitance and inductance becomes important. Even the "leads zeroing" procedure provided by the LCR meter does not necessarily ensure exclusion of the parasitic effects. The multi-strip geometry helped us to estimate possible inaccuracy due to the parasitic elements in the measurement circuit. First, the capacitance was measured on all the individual samples on the same film.es of strips. Then the same measurements were performed on the samples connected in parallel. Based on individual capacitance values we calculated the expected capacitance of two, three, four or five samples in parallel and compared these values with the measured ones. Discrepancy was usually small, not higher than 5%. We consider this result as verification of the small influence of parasitic reactant elements. Another way to estimate parasitic effects was to measure the glass substrate with electrodes but without a semiconductor film. It was found that the measured capacitance (imaginary part of admittance) was two orders lower than that measured with the semiconductor film.

Measurements in dark and light

The sample to be characterized is positioned in a metal box whose internal and external surfaces are coated with a black paint. The sample can be illuminated through a glass window in the top cover of the box. We use a white light source for illumination and neutral density filters to vary the light intensity. To provide dark-measurement conditions the box is thoroughly protected from the room light with a multi-layer dense black cloth.

All the CdTe and CdS polycrystalline films manifest a significant photo-conductivity effect (see Fig. 1.7). Even illumination with a light of 0.1 Sun intensity as in Fig. 1. 7 provides a 10-1000 fold decrease in measured resistance, depending on the GB resistance. Usually a significant difference is also observed between resistances measured without using a light source but with and without the black cloth. The measured capacitance is also sensitive to the illumination, especially the bias dependent capacitance.

Another issue to be discussed is the kinetics of photo-response. After turning light on, a steady state resistance value is achieved in a short time not exceeding one or several seconds. After switching the light off, a rapid increase in resistance takes place initially, followed by very slow restoration of the "dark" resistance. This process is not a simple exponential decay. The instantaneous relaxation time increases with real time of observation, so that we may wait for hours or sometimes days for the total restoration of the dark resistance. Thus the real "dark" conditions are not achievable in a reasonable time. It is beyond any doubt that thorough studies of transient effects are of great interest themselves. These studies can shed light on some

important properties of deep GB electron states. They also might clarify some light-induced changes in defects accumulated at the GB region and their spatial distribution.

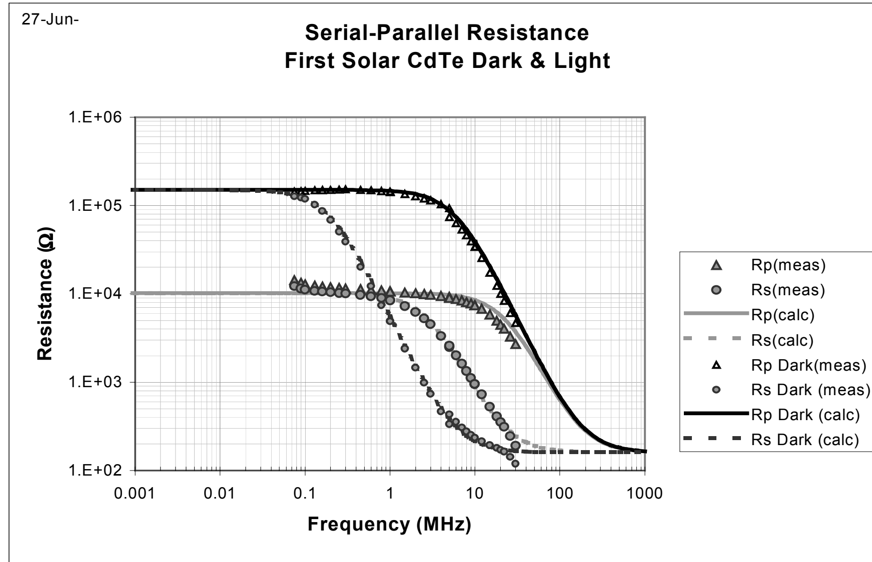

Fig. 1.7 Comparison of the frequency dependencies of R_p and R_s measured on CdTe film in dark (without black cloth) and in light (0.1 Sun intensity). More than ten-fold decrease in light is seen.

These transient effects are distinct for differently processed and stressed films, and make interpretaion of dark measurements less reliable. In this report we confine ourselves to measurements under controllable light conditions. It was found that the 0.1 Sun light intensity is usually sufficient for these measurements. First, at this light intensity no long-term transient effects in films were observed at room temperature. Then, the film resistance under these conditions decreases, making AC measurements possible in the whole frequency range. Finally, the sample heating by illumination is small, which is important when studying the GB resistance, which depends exponentially on temperature due to the GB potential barriers.

1.1.3 Major results of the GB studies

Influence of processing procedure on the GB resistance

CdTe films on the glass substrates were prepared by B. McCandless at the Institute of Energy Conversion (University of Delaware) with physical vapor deposition at a substrate temperature of 325° C. Some films were treated with $CdCl_2$ and doped with S or Cu at the CSM facilities. AC measurements of R_p, R_s, C_p, and C_s were performed with and without illumination. Measurements at zero bias and fitting data with Eqs. 1.1- 1.4 were used to obtain R_{GB}, C_{GB}, and R_{IG} values for each sample.

The R_{GB} value was orders of magnitude greater than the R_{IG} for all films. The estimated potential barrier height Φ_b without illumination varied from 0.7 to 0.3 eV depending on post-deposition treatment. The decrease in barrier height caused by illumination reached values of 0.15-0.2eV for

some films. The $CdCl_2$ treatment lowered R_{GB} measured in light only. Sulfur diffusion lowered the "in-light" R_{GB} value, but increased the "in-dark". Finally, copper diffusion into CdTe films was found to lower both "in-dark" and "in-light" R_{GB} values by more than two orders of magnitude.

Space charge density in the GB region and density of GB states derived from the bias-dependent capacitance

According to theory [11,12], the contribution of the oscillating capacitance is zero without an application of bias. Thus capacitance measured at zero bias is equal to the depletion capacitance. Based on the average grain size and film geometry and assuming the square-shaped grains of the same size, we estimated the specific GB depletion capacitance $C_{G\text{-}G}$*, that is capacitance per unit area of a single GB. Its value did not vary much with the varying post deposition treatment and was in a range of around 5×10^{-7} F/cm^2. The space charge density in the GB depletion region, ρ_{GB} was estimated from the $C_{G\text{-}G}$* value using the equation:

$$\rho_{GB}=(8\Phi_{b0}/\varepsilon\varepsilon_o)(C_{G\text{-}G}^*)^2 \qquad (1.6)$$

where Φ_{b0} is the zero-bias potential barrier height. The obtained value of ρ/e was in the range of 10^{17}-10^{18}cm^{-3}. The $C_{G\text{-}G}$*, hence the ρ_{GB} value might be overestimated by assuming such a simple morphology of the films but the error could not be orders of magnitude. Thus one can conclude that the space charge density in the GB region is much higher than the hole concentration derived from the C-V measurements on the CdTe cells. This result is consistent with the estimates obtained in Ref. 2. In the case of dominating compensation of acceptors by the GB states, the negative space charge density in the GB proximity, should be close to the acceptor concentration and can be much higher than the free hole concentration derived from the C-V profile. However, one cannot exclude an enhanced doping density in the GB region due to accumulation of dopant. Indeed, the estimated value of ρ_{GB} for the Cu-doped films was several times higher than that for the undoped films.

As shown in [11], measurements of bias-dependent oscillating capacitance C_T can provide an estimate of the GB density of states. In [3, 4] we have presented a simplified analysis of the problem limited to the case of a low bias applied to a single GB, namely, $V^*<\Phi_{b0}/2$. For the specific capacitance (per unit area of a single GB) we have obtained the equation:

$$C_T^*=\{2C_{G\text{-}G}^*(0)/[1+4C_{G\text{-}G}^*(0)/e^2D_T]\}\times \tanh(V^*/2kT) \qquad (1.7)$$

where $V^*=V_{bias}d/l$, V_{bias} is the bias voltage applied between probes, l is the inter-probe distance, and d is an average grain size. The density of the GB traps, D_T, is assumed constant, because a small V* effects both the trap occupation and Fermi level position with respect to the trap band only slightly. Thus the measured capacitance increases with bias, until it reaches saturation at $V^*>2k_BT$, thereafter it may slowly decrease due to the decreasing depletion capacitance. Using this model, and allowing d and D_T to be fitting parameters, one can obtain information about average grain size and GB density of states:

$$D_T = (4/e^2)\times \beta/(2-\beta)\times C_{G\text{-}G}^*(0);\ \ \beta= C_T^{sat}/C_{G\text{-}G}(0) \qquad (1.8)$$

It was found that the measured $C_T(V_{bias})$ dependence fits the equation above for all the films studied . Fig. 1.8 shows the experimental data for one of the CdTe thin films prepared with PVD. The film thickness is 2.3 μm and the distance between gold electrodes is 0.18 mm. To decrease the sample resistance it was illuminated with white light of 0.125 Sun intensity.

The fit of experimental data was quite satisfactory. An average grain size, *d*, of 1.3 μm, is in agreement with the estimate based on AFM images. An estimated maximum bias voltage per single GB is $V^*_{max}<0.11V$. That satisfied the condition of small bias voltage, $V^*<\Phi_{b0}/2$, which we used when deriving the equations. The estimated density of GB states, D_T, is about 3.5×10^{12} $cm^{-2}eV^{-1}$. Since the bias applied is small, this value is approximately equal to the GB density of states at the GB Fermi level for the unbiased GB. Similar measurements were made on other PVD CdTe films and on the CdTe films lifted off from the TCO/CdS/CdTe structures prepared by CSS at NREL. These samples were provided by Dr. L. Woods. The estimated D_T values varied in the range of 10^{12} to 10^{13} $cm^{-2}eV^{-1}$. For Cu-doped films it was higher than for the undoped ones.

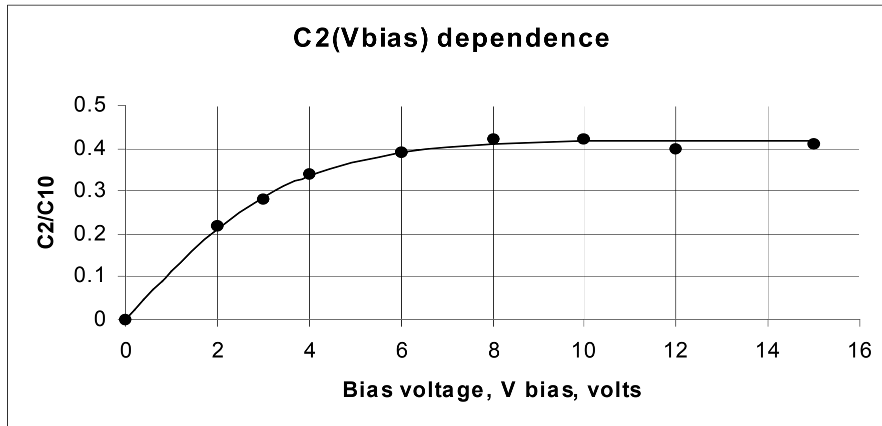

Fig. 1.8 Dependence of the GB "oscillating" capacitance on bias voltage between probes. Here C_2 is equivalent to C_T, and C_{10} to $C_{G\text{-}G}(0)$ in Eq. (1.7). The sample is a PVD CdTe thin film. Points represent the experimental data; solid line represents calculations according Eqs. 1.7 and 1.8 with fitting parameters $C_T^{sat}/C_{G\text{-}G}(0)$ =0.41 and average grain size *d*=1.3 μm.

1.1.4 Conclusions

- Impedance spectroscopy can provide a vast and important information on electronic properties of grain boundaries in thin polycrystalline CdTe films if appropriate physical and electrical models are used.
- The GB contribution to the in-plane film resistance can be separated from the contribution of the grain bulk material. Analysis of the former, especially if combined with temperature

dependence of their resistance allows estimates of the potential barrier height and dominating grain-to-grain carrier transport mechanism.

- Along with the GB resistance, IS provides estimates of the specific GB capacitance. In this way the space charge density (SCD) in the vicinity of GB can be estimated. Our results show that it exceeds the SCD value estimated with the C-V profiling of cells by orders of magnitude.
- Studies of the bias-dependent “oscillation” capacitance provide information on density of the GB electronic states in the vicinity of Fermi level.
- IS measurements under illumination of varying intensity and its kinetics can help to understand mechanism of the GB states recharging by light and their influence on photo-electric properties of a cell, particularly on the effective lifetime of photo-generated carriers.

1.2 Hall Effect in Thin CdTe Polycrystalline Films

As shown in Sec. 1.1, polycrystalline CdTe films in the cells demonstrate a fine-granular structure (grain size of ~1 μm) and high density of deep GB electronic states (up to 10^{13} cm^{-2} [3]). An important effect of GB states is trapping of the majority carriers (holes). The resulting GB potential barrier for holes provides high resistance for grain-to-grain transport. Recent studies showed that the barrier height in CdTe films extracted from a cell could be as high as 0.8 eV [2]. Besides the straightforward impact of GB on the CdTe electronic properties, hence the cell performance, their influence should also be taken into account when characterizing properties of grain bulk, in particular carrier concentration and mobility derived from Hall measurements [13].

In this section we present combined studies of Hall effect and of impedance spectroscopy (IS) under varying illumination in thin CdTe polycrystalline films. The IS allows one to separate and estimate individual contributions of GB and bulk (B) material to the film in-plane resistance. Illumination of films can significantly reduce the GB resistance (see Sec. 1.1). We have used this effect to exclude the influence of high resistive grain boundaries, and to estimate the real hole concentration and mobility in the doped p-type films where IS revealed a significant contribution of GB to the film resistance. In the undoped films with small hole concentration and negligible GB resistance, the light-dependent Hall measurements were used to estimate the concentration of the photogenerated electrons, along with their mobility and lifetime.

1.2.1 Experimental details

CdTe films with thickness of ~3μm were deposited on soda lime glass using the First Solar proprietary vapor transport deposition method. After deposition, some films were doped with Cu using the standard First Solar procedure. After this anneal, typical grain sizes are 1-2 μm. Due to high diffusivity of Cu in CdTe [14], the resulting Cu distribution is estimated to be almost uniform throughout the film thickness. Doping with Cu has significantly changed the electrical properties of the CdTe films. For example, Hall concentration of holes, p_H, in these films exceeds 10^{13} cm^{-3} and Hall mobility, μ_H, is of the order of several units of cm^2/Vs. In the undoped films, however, p_H~10^9-$10^{10}cm^{-3}$ and μ_H~20-50 cm^2/Vs.

Gold electrical contacts, ~ 80nm thick, were evaporated on the surface of CdTe. Two different contact arrangements were used: one a standard van der Pauw geometry of contacts on the corners of a square-shaped sample for Hall measurements and the second a series of parallel strips with 0.2 mm spacing between them for IS measurements (see Sec. 1.1). Measurements between different pairs of strips were used to check electrical uniformity of a film in plane and also to exclude contribution of possible parasitic effects.

Hall measurements were performed using a Bio Rad HL5500 Hall effect measurement system. IS measurements were done with the equipment and procedures described in Section 1.1.

Illumination of samples during IS and Hall measurements was performed using a light source simulating the solar spectrum, fed through a fiber optic bundle. The intensity of illumination was controlled using various gray filters and their combinations, and measured using a Newport power meter (model 1815-C) with a silicon detector. The intensity of light did not exceed $2mW/cm^2$. All measurements were done at room temperature. To avoid overheating of the fiber optic bundle we have used the SnO_2:F/Glass filters that cut off the IR irradiation with wavelengths higher than ~1400 nm.

1.2.2 Measurements and discussion

Doped Films

Before measuring the Hall concentration and mobility under varying illumination, the doped films were characterized with IS under the same light intensities. The light intensities were chosen to provide significant reducing R_{GB}, while being low enough to exclude the influence of photogenerated carriers in the grain bulk. Table 1.1 presents data for one of these films.

Table 1.1 Parameters measured and calculated for the CdTe:Cu film at different light intensities

R_{GB}/R_B	p_H, cm^{-3}	μ_H, cm^2/Vs	p_{calc}, cm^{-3}	$\mu_{calc.}$, cm^2/Vs
$2.3x10^3$	$2.3x10^{13}$	5.5	$3.0x10^{15}$	110
$3.1x10^2$	$1.2x10^{14}$	7.1	$2.3x10^{15}$	142
$2.0x10^2$	$2.9x10^{14}$	5.3	$3.1x10^{15}$	115
$1.7x10^2$	$3.1x10^{14}$	7.3	$2.9x10^{15}$	145
		Average	$\approx 2.8x10^{15}$	128

The first column shows the ratio of the GB and bulk resistances measured at different light intensities. The next two columns present data on measured Hall concentrations and mobilities. The concentration and mobility in the grain bulk presented in the last two columns were calculated based on the experimental data, using the procedure described below.

The analysis here is based on the model (Fig.1.9) and equations presented in Ref. 13, and is aimed at interpretation of the photo-Hall effect in polycrystalline films.

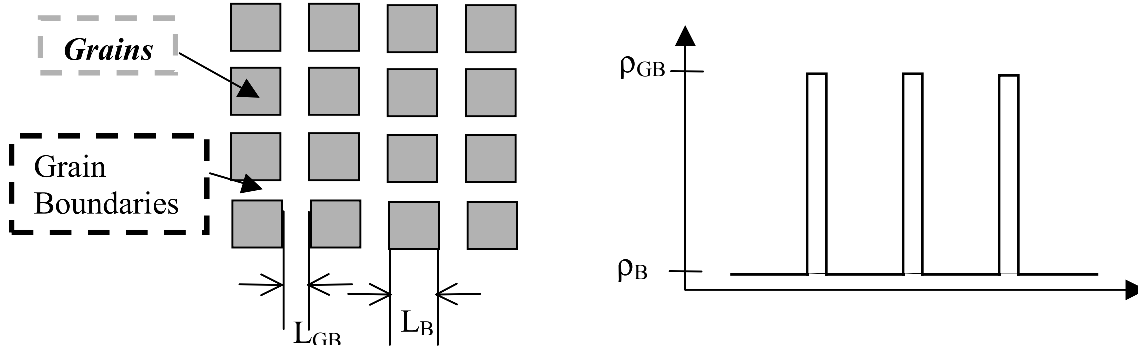

Fig. 1.9 Block diagram of a polycrystalline film with regularly arranged square shaped grains separated by GB regions of high resistivity. (a) Spatial arrangement of identical grains and grain boundaries. b) Spatial distribution of resistivity of grains (ρ_B) and GB regions (ρ_{GB}).

If the same mobility is assumed in the grain bulk and in the GB region, the theory developed in [13] contains two parameters of theory: L_{GB}/L_B and ρ_{GB}/ρ_B (see Fig.1.9). We have replaced the second parameter by the ratio R_{GB}/R_B, which is measured using IS. Thus, there is only one adjustable parameter remaining, L_{GB}/L_B. With this modification, the equations for the Hall concentration and mobility from [13] transform to:

$$\frac{p_H}{p_B} = \frac{(1+\beta^2/\gamma)(1+\beta+\beta^2+\beta^2/\gamma)}{(1+\beta)+\beta[(1+\gamma)(1+\beta^2/\gamma)+\beta(1+\beta)]} \tag{1.9}$$

$$\frac{\mu_H}{\mu_B} = [(1+\gamma)(1+\beta^2/\gamma)]^{-1} + \frac{\beta}{(1+\beta)}\left(1+\frac{\beta/\gamma(1+\beta)}{(1/\gamma+1)(1+\beta^2/\gamma)}\right) \tag{1.10}$$

where p_B and μ_B are the hole concentration and mobility in bulk material, p_H and μ_H are the same quantities obtained by Hall measurements; $\gamma = R_{GB}/R_B$, and $\beta = L_{GB}/L_B$. Figure 1.10 shows that for high grain-boundary resistance, the Hall concentration can be much smaller than the real concentration in the bulk. The Hall mobility also reduces as γ increases, and its dependence saturates at the level determined by the L_{GB}/L_B ratio.

The best fitting of the experimental dependence of p_H/p_B on R_{GB}/R_B was obtained for $L_{GB}/L_B \approx 0.05$. While the measured Hall concentration varies by more than the order of magnitude, the estimated p_B value is almost the same at all light intensities and is higher than any measured Hall concentration value (see Table 1.1, columns 2 and 4). The estimated bulk mobility is presented in the last column of the table. The reported hole mobility in single crystal CdTe [15] is lower by 40-50%, but is still 10-12 times higher than the measured Hall mobility.

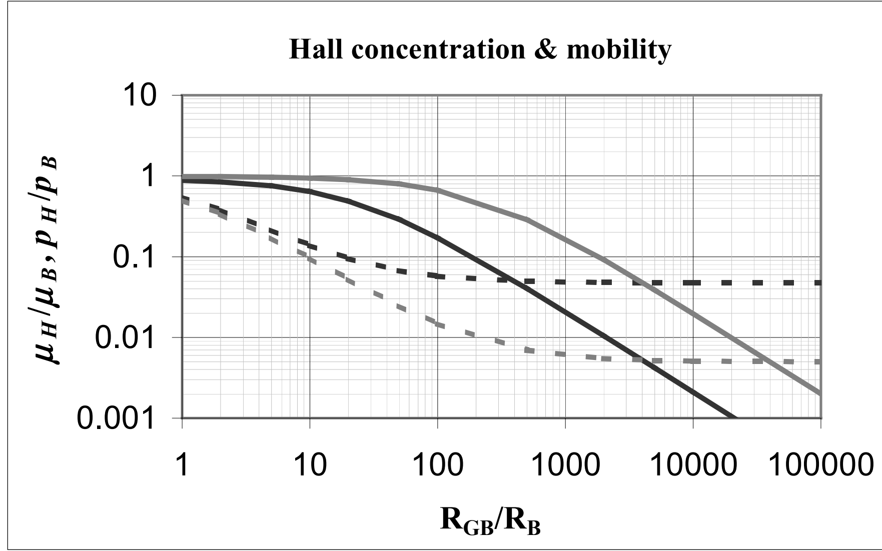

Fig. 1.10 Dependence of Hall concentration and mobility on the GB region resistance and size. Solid curves are p_H/p_B, dashed are μ_H/μ_B, black indicates L_{GB}/L_B = 0.05, and gray L_{GB}/L_B = 0.005.

Undoped Films

The Hall coefficient measured in dark on undoped films is positive, and the hole concentration is below 10^{10}cm^{-3}, but greater than 10^9cm^{-3}, while the measured hole mobility is ~50cm^2/Vs. This high mobility is consistent with the results of IS which did not reveal considerable resistance of the GB. The high density of GB states [3] causes depletion of the GB bulk (low carrier concentration), accompanied with reduced GB barriers. The influence of light on the Hall effect in undoped films is dramatically different from that in the doped ones. Even for a very low illumination intensity ~5µW/cm^2, the Hall coefficient, R_H, becomes negative, indicating a significant contribution of photogenerated electrons. With increasing illumination intensity (up to 1 mW), the magnitude of the Hall coefficient increases, then passes a maximum and decreases again. The Hall mobility increases monotonically up to μ_H ~ 300 cm^2/Vs with illumination. For data analysis, the equations for the mixed electron-hole conductance were used:

$$R_H = \frac{A_H}{e}\frac{p\mu_p^2 - n\mu_n^2}{(p\mu_p + n\mu_n)^2}; \qquad p = p_o + n \tag{1.11}$$

$$\mu_H = A_H\left|\frac{p\mu_p^2 - n\mu_n^2}{p\mu_p + n\mu_n}\right|; \tag{1.12}$$

where p, n, μ_p and μ_n are the hole and electron concentrations and mobilities respectively, and p_o is the hole concentration in dark. Since the measured values of p_o >10^9 cm^{-3}, the equilibrium electron concentration is negligibly small in CdTe at room temperature. The Hall factor A_H,

being close to 1, was neglected in the calculations. Figure 1.11 presents experimental values of p_H and μ_H for the film with dark hole concentration $p_o = 4.5x10^9$ cm^{-3} and dark Hall mobility μ_H = 47 cm^2/Vs as a function of n/ p_o, (of light intensity). Calculations (solid curves) were made with μ_n =280 cm^2/Vs which provided the best fitting. This mobility value is somewhat lower than the highest values reported for the CdTe single crystals of ~1000 cm^2 /Vs. It does not seem surprising because the density of defects that scatter electrons in the polycrystalline films are expected to be higher than in single crystals. It is more surprising that the difference is rather small for holes.

We have used the relationship between the non-equilibrium carrier concentration values obtained as described above and the light intensity to estimate the effective lifetime of electrons. Based on the power distribution over the photon energies in solar spectrum, we estimated the flux of incident photons of energy exceeding the CdTe band gap. Then, assuming the quantum efficiency of 100%, we calculated the photogeneration rate, G, $(cm^2s)^{-1}$. With the simplifying assumption of uniform distribution of the photogenerated electrons over the film thickness t, we calculated lifetime as $\tau = (n/G)t$. With a small spread it turned out: $\tau \approx 8\times10^{-9} s$. Probably the lifetime is somewhat underestimated if to take into account the simplifying assumptions made, like 100% quantum efficiency and uniform distribution of the photogenerated carriers.

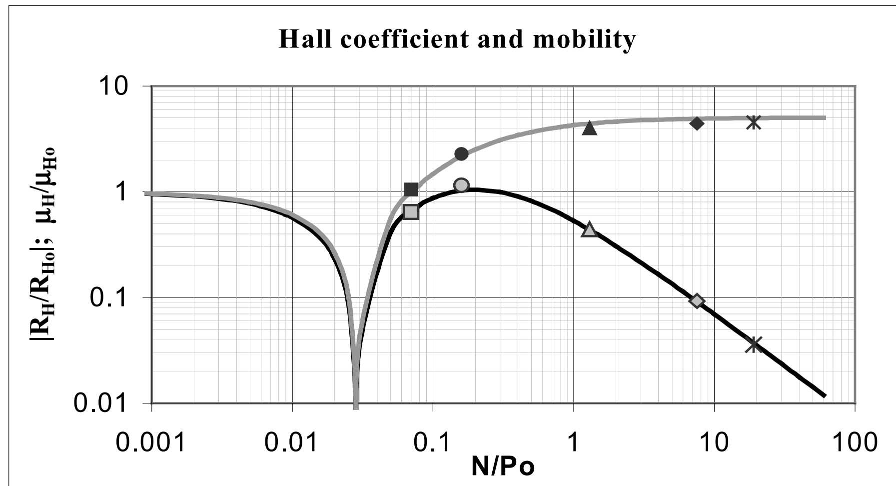

Fig.1.11. Dependence of Hall concentration and mobility on concentration of photogenerated electrons. The black line is the calculated ratio R_H/R_{Ho}, and gray line is μ_H/μ_{Ho}. Black filled points are measured μ_H/μ_{Ho}, and gray filled R_H/R_{Ho}. Light power (per cm^2) is as follows: asterisks = 1.6mW, diamond = 0.6mW, triangle = 58μW, circle = 6.7μW, square = ~3μW.

1.2.3 Conclusions

- Combined Hall and impedance spectroscopy (IS) measurements under varying illumination (photo-Hall and photo-IS) provide an opportunity to evaluate the real carrier concentration and mobility in the p-type CdTe films with the high resistance grain boundaries.
- In films with moderate hole concentration, e.g., ~ 10^{14} cm^{-3}, the electron lifetime can be estimated from measurements of this kind at light intensities of ~ 20 mW/cm^2.

2. BASIC ELECTRONIC PROPERTIES OF THIN FILM TRANSPARENT CONDUCTIVE OXIDES

2.1 Introduction

Transparent conductive oxides (TCO) have numerous technical applications, in particular as the front contact layers in thin film solar cells. For the latter, the most widely used TCO's include tin oxide doped with fluorine and antimony, the tin doped indium oxide (ITO) and zinc oxide usually doped with aluminum. In addition to binary compounds, ternary compounds with very promising properties have been developed, such as cadmium stannate and zinc stannate, but their thin films have not yet been used widely. To improve the properties of existing and new TCOs, it is important to put the topic on a solid scientific basis by obtaining detailed information about the electronic properties of thin films, as well as about the effect of substrates (glass, polymer, other semiconductors etc.), film structure, morphology etc. This information, and its theoretical analysis, will enable an estimate to be made of the limiting mobility and of the achievable figure-of-merit for practical TCOs. The approach requires a variety of methods and tools for characterization of the fabricated samples as well as solid scientific grounds for interpretation and theoretical analysis of the data. This section presents our studies in this area.

In the figure of merit of TCOs that is commonly used, transparency is weighted much higher than low sheet resistance [16], hence the range of the free carrier concentration, n, is defined by transparency. Free carrier absorption becomes a serious problem at $n \sim 10^{21} cm^{-3}$. Through extrinsic doping, the carrier concentration in commercially available and newly developed TCOs approaches this level. It is not practical to increase the carrier concentration further. Thus, the only possible way to decrease sheet resistance is to improve carrier mobility.

Mobility in single crystals is defined by fundamental electronic parameters, such as the effective mass of free carriers, the dominating scattering mechanism, types and density of scatterers, etc. The major goals of our research are to modify and develop novel methods and apply them to study basic electronic properties of TCO thin films relevant to mobility, clarify the factors that determine sheet resistance in polycrystalline films and try to estimate the theoretical limit for mobility. The methods we use are based on measurements and analysis of electron transport phenomena both in stationary external fields and in high-frequency electromagnetic field (optical characterization). The results of studies presented in this section relate to SnO_2:F and ZnO:Al thin films.

2.2 Electron Parameters to be Determined: their Influence on the TCO Figure-of-Merit.

2.2.1 Band model, the effective mass tensor, and density of states.

Along with the bandgap that defines the short-wavelength transmission limit of the material, other details of the band structure are necessary to determine the achievable figure-of-merit. In general, we need to know the dependence of the carrier energy on its wave vector, ***k*****,** in the conduction band. In particular, we are interested in the shape of the constant-energy surfaces in ***k***-space and the effective mass value, which are equivalent to the dependence $E(\boldsymbol{k})$. We will limit the discussion to i) isotropic, spherically-shaped surfaces, ii) single-ellipsoid surfaces, and iii) multi-ellipsoid surfaces. By way of example, we shall consider the conduction band of silicon.

In general, the reciprocal effective mass is a second rank tensor that reduces to a scalar quantity for a spherical band. For a single-ellipsoid model, it is characterized by three values of effective mass, m_i^* (i=1, 2, 3), each corresponding to one of the principal axes of the ellipsoid. In the case of the ellipsoid of revolution, we have only two independent values of the effective mass: m_{φ}* related to the direction of the revolution axis, and $m_{\perp}$* related to the perpendicular axis. In the n-Si-like band model we have 6 equivalent ellipsoids located in ***k***-space on the <100>-type axes which are the axes of revolution.

Together with the relaxation time, τ, which is to the first approximation the inverse of the collision (scattering) frequency, effective mass determines mobility. The smaller the effective mass, the higher the mobility. For the isotropic band, the carrier mobility is determined by the equation

$$\mu = \frac{e\langle\tau(E)\rangle}{m^*} \tag{2.1}$$

in which $\langle\tau(E)\rangle$ symbolizes averaging τ over the conduction band weighted for a parabolic band by $E^{3/2}\left(\frac{\partial f_0}{\partial E}\right)$ where $f_0(E)$ is the Fermi-Dirac distribution function. A highly degenerate electron gas, such as a typical TCO, has $(E_F - E_c)/k_BT >> 1$. E_F is Fermi energy, E_c is the energy of the minimum in the conduction band, and k_B is the Boltzmann constant. In such materials $\left(\frac{\partial f_0}{\partial E}\right)$ differs from zero only in the vicinity of Fermi level, hence only the carriers with energies close to Fermi level contribute to electron transport. The properties of these carriers determine the magnitude of the mobility and the other transport coefficients. Thus for an isotropic band, mobility is given by

$$\mu = e\,\tau(E_F)/m^*(E_F). \tag{2.2}$$

Subsequently, we shall presume high degeneracy, and omit the reference to the Fermi level. For an isotropic relaxation time the only reason for the mobility to be anisotropic is anisotropy of the effective mass. For a single ellipsoidal band, the mobility may be expressed as

$$\mu_i = \frac{e\tau}{m_i^*} \tag{2.3}$$

in which the subscript refers to the three principal ellipsoid axes. In polycrystalline material, with randomly oriented crystallites, averaging spatially leads to an isotropic mobility, given by

$$\mu = \frac{1}{3}e\tau\sum_{i=1}^{3}\frac{1}{m_i^*} \tag{2.4}$$

For crystals of cubic symmetry with multi-valley band, such as n-Si or n-Ge, the mobility is isotropic and may be described by

$$\mu = e\tau / m_c^* . \tag{2.5}$$

m_c^* is the *conductivity effective mass* and is determined by

$$\frac{1}{m_c^*} = \frac{1}{3}\left(\frac{1}{m_\parallel^*} + \frac{2}{m_\perp^*}\right) . \tag{2.6}$$

The factor of 2 inside the parentheses arises because there is rotational symmetry of the ellipsoid in k-space. The conductivity effective mass influences the plasma frequency and, hence, the long-wave limit of transparency of the TCO. The plasma frequency is given by

$$\omega_p = \left(\frac{e^2 N}{m_c^* \varepsilon_\infty \varepsilon_0}\right)^{1/2} , \tag{2.7}$$

where N is the carrier concentration, ε_0 is the free space dielectric constant, and ε_∞ is the high frequency dielectric permittivity of the material.

The density-of-states (DOS) function, $D(E)$ is an important characteristic of a material that also depends on effective mass. For a parabolic band spectrum ($E \alpha k^2$)

$$D(E) = \frac{4\pi (2m_d^*)^{3/2}}{h^3} E^{1/2} \tag{2.8}$$

Here m_d^* is the *density-of-states* (DOS) effective mass, which is a combination of the effective mass components. For the cases of an isotropic spectrum, a single ellipsoid band and a multi-ellipsoidal band, the DOS effective mass is given by equations (2.9) a), b) and c), respectively.

$$m_d^* = m^* \qquad \text{a)}$$

$$m_d^* = (m_1^* m_2^* m_3^*)^{1/3} \qquad \text{b)} \tag{2.9}$$

$$m_d^* = \mathrm{N}^{2/3} (m_1^* m_2^* m_3^*)^{1/3} \qquad \text{c)}$$

where N is the number of the equivalent ellipsoids, e.g., N=6 for n-Si. It is seen that m_d^* can differ significantly from m_c^*, especially for the multi-ellipsoid model. Comparison of these two values, which may be obtained experimentally, can provide information about the band structure and, in particular, whether it is single- or multi-valley. It can also reveal information about the anisotropy of the constant-energy ellipsoids i.e. about the ratio $\beta = m_\parallel / m_\perp$.

In turn, the DOS function, hence the effective mass, determines the Fermi level for a specific carrier concentration:

$$E_F = \left(\frac{3N}{8\pi}\right)^{2/3}\left(\frac{h^2}{2m_d^*}\right) \tag{2.10}$$

The change in the position of the Fermi level as a function of carrier concentration, relative to the conduction band minimum, leads to the Burstein-Moss shift [17], which defines the short-wave limit for transparency.

Neglecting the difference between the m_d* and m_c* values can impact estimates of the achievable figure of merit. One must remember that expressions for mobility and plasma frequency include m_c*, while expressions for E_F and hence for the Burstein-Moss shift include m_d*.

2.2.2 Carrier scattering, relaxation time, scattering parameter

Carrier scattering leads to a finite mobility value. The higher the scattering (collision) frequency, hence the lower the relaxation time, the lower the mobility. A high scattering rate causes a less sharp the plasma reflection edge, thus worsening the transparency spectrum. It also affects absorption by free carriers. Carriers are scattered by phonons, point defects, like vacancies, interstitials, impurity atoms and ions, etc., by dislocations, and by two-dimensional defects like small angle boundaries (dislocation walls) or grain boundaries in a very fine granular structures. While the effective mass is considered an intrinsic parameter of a material that depends on its composition, the relaxation time is much influenced by the crystal quality that depends on structural imperfections, hence on the film preparation technique.

Relaxation time depends on the carrier energy (this dependence is different for different scattering mechanisms). In the case of semi-elastic scattering, dependence of scattering frequency on energy can be presented in the form:

$$\tau^{-1}(E) \propto W(E)D(E) \tag{2.11}$$

where $D(E)$ is the DOS function and $W(E)$ is the square matrix element of the electron scattering giving the probability of transition from one quantum state to another of the same energy. For the most commonly discussed scattering mechanisms, theory shows that, in a parabolic band, $W(E)$ is a power function of energy and is commonly represented as

$$W(E) \propto E^{-r} \tag{2.12}$$

In a parabolic band, the density of states is given by

$$D(E) \propto E^{1/2} \tag{2.13}$$

which means that

$$\tau \alpha E^{r-1/2} \quad \tau \propto E^{r-1/2} \tag{2.14}$$

The quantity r is known as the scattering parameter and it is different for each scattering mechanism, varying from r=0 for acoustic phonon scattering, to r=2 for ionized impurity scattering. This kind of dependence, with a fixed value of the scattering parameter, takes place only if the same scattering mechanism dominates over the entire energy range. In reality, several scattering mechanisms may occur simultaneously. The total scattering frequency is the sum of the individual frequencies due to each of the scattering mechanisms, which may be expressed as

$$\omega_c = \tau_c^{-1} = \sum_i \tau_i^{-1} \tag{2.15}$$

The dependence of relaxation time on energy can be more complicated when a wide range of energies is being considered. Fortunately, in the case of high degeneracy (the only practical case for TCOs), only a narrow range of energy around E_F is of interest. In this case *W(E)* can be approximated by a power function

$$W(E) = W(E_F) \times (E/E_F)^{-r} \tag{2.16}$$

The scattering parameter in this case is defined as

$$r(E_F) = \left(\frac{d \ln \tau}{d \ln E} \right)_{E=E_F} + \frac{1}{2} \tag{2.17}$$

Along with the concentration and temperature dependencies of mobility, knowledge of the scattering parameter value is important for identifying the dominant scattering mechanism(s). It is also to be noted that the relaxation time depends on the effective mass because of its inverse dependence on the density of states. In heavily doped (degenerate) TCOs, scattering by impurity ions is sometimes the dominant scattering mechanism. In this case, for materials that have the same carrier concentration, the density of impurity ions, and the dielectric permittivity, there can be a difference in mobility due to different effective masses, $\tau \propto 1/m^*$, thus $\mu \propto 1/m^{*2}$.

2.2.3 Influence of non-parabolicity

The dependence $E(k)$ is parabolic only in the immediate vicinity of the conduction band minimum. As energy increases, the dependence deviates from parabolic and the only question is at what energy the deviation becomes sufficiently important to influence the properties of electrons of interest. The most obvious indication of non-parabolicity is the increase of measured effective mass with energy (with Fermi level or carrier concentration in degenerate semiconductors). In narrow-gap and direct-gap semiconductors, such as InSb, (Hg,Cd)Te, PbSe, (Pb,Sn)Te, non-parabolicity significantly affects electronic transport properties at Fermi levels of E_F ~ 0.1eV, or even lower. For wide-gap semiconductors, such as TCOs, non-parabolicity has not been much investigated but for heavily doped ZnO, CdO, and zinc stannate it has been established that there is a progressive increase of the density-of-states effective mass with carrier concentration [18-20].

To analyze the influence of non-parabolicity, we consider the theory of electron transport developed in [21, 22] for the rather general, multi-ellipsoid, non-parabolic band model. The equations for the transport coefficients are based on solutions of the Boltzmann equation and the relaxation time approximation. In [21, 22] the energy dependence on wave vector in the principal ellipsoid axes (1, 2, 3) is described by the equation:

$$\frac{\hbar^2}{2}\left[\frac{k_1^2}{m_{10}^*}+\frac{k_2^2}{m_{20}^*}+\frac{k_3^2}{m_{30}^*}\right]=\gamma(E)=E\left(1+\frac{E}{E_1}+\frac{E^2}{E_2^2}+\frac{E^3}{E_3^3}+\cdots\cdots\right) \quad (2.18)$$

where m_{i0}^* (i=1, 2, 3) are the effective mass components at the bottom of the band (E=0), $\gamma(E)$ is an arbitrary function of energy ($d\gamma/dE>0$), which may be represented as a power series in energy with coefficients given by E_1, E_2^2, E_3^3, etc. The latter have dimensions of energy raised to the same power as their energy term in each numerator. The values of E_1, E_2, E_3, etc., determine the deviation of the spectrum from parabolic for each energy E. If $E<<E_1$, E_2, E_3, etc., the equation reduces to that of a parabolic band. We will refer to first order non-parabolicity as the case when

$$\gamma(E)\approx E\left(1+\frac{E}{E_1}\right) \quad (2.19)$$

in the energy range of interest, while the terms of higher power in energy can be neglected.

For the non-parabolic spectrum, the equations for the effective masses, density of states function and carrier concentration are

$$\begin{aligned} m_i^*(E) &= m_{i0}^*\frac{d\gamma}{dE} && \text{a)}\\ m_c^*(E) &= m_{c0}^*\frac{d\gamma}{dE} && \text{b)}\\ m_d^*(E) &= m_{d0}^*\frac{d\gamma}{dE} && c) \end{aligned} \quad (2.20)$$

$$D(E)=\frac{4\pi\left(2m_{do}^*\right)^{3/2}}{h^3}\left[\gamma(E)\right]^{1/2}\frac{d\gamma}{dE} \quad (2.21)$$

$$N=\frac{8\pi}{3}\frac{\left(2m_{d0}^*\right)^{3/2}}{h^3}\left[\gamma(E_F)\right]^{3/2} \quad \text{(high degeneracy)} \quad (2.22)$$

It is seen that the effective mass increases with energy since $d\gamma/dE>0$. The density of states grows more rapidly with energy and Fermi level increases slower with the carrier concentration than in a parabolic band.

Non-parabolicity changes the relaxation time dependence on energy. One of the reasons is the change in the $D(E)$ dependence. The scattering matrix element is preserved in [22] with the same dependence as in the parabolic case, $W(E) \propto \left(k^2\right)^{-r}$, with the same values of the scattering parameter r for each particular scattering mechanism. Thus, based on equation (2.21), one obtains for the non-parabolic spectrum

$$\tau \propto \left[W(E)D(E)\right]^{-1} \propto \gamma^{r-1/2}\left(\frac{d\gamma}{dE}\right)^{-1} \tag{2.23}$$

instead of $\tau \propto E^{r-1/2}$ for the parabolic band.

The above analysis shows that we need to know the real dependence, $E(\mathbf{k})$, when trying to estimate the limiting value of mobility, μ_{lim}, for heavily doped TCOs. Using, for example, the effective mass obtained from a sample of a not-too-high carrier concentration, one can overestimate μ_{lim} for a material with a more practical carrier concentration. The same is true for the plasma frequency and the Burstein-Moss shift. Analysis of the transport phenomena, aimed at establishing the dominant scattering mechanism, can lead to the wrong conclusions if parabolic theory is applied to a material while the spectrum is actually non-parabolic.

2.3 Formulation of Experimental Methods

2.3.1 Method of four coefficients (electron transport in stationary external fields).

The method discussed in this section is aimed at the determination of mobility, the DOS effective mass, m_d^*, and the scattering parameter, r. It is based on the simultaneous measurements of four transport coefficients: electrical resistivity, ρ, the Hall, Seebeck, and Nernst-Ettingshausen coefficients, R_H, α, and Q, respectively (ρ and α at $\mathbf{B}$=0, and R_H and Q in a weak magnetic field). The method does not require fulfilling the condition of strong magnetic field (μB>>1) as some powerful methods for the band structure studies do (e.g. cyclotron resonance, Shubnikov-de Haas and de Haas- van Alphen effects). This is a significant advantage for TCOs that typically have small mobilities and do not meet this condition (μ < 100 cm^2 V^{-1} s^{-1}, and μB <0.01 for B = 1 Tesla). Measurements in a wide range of carrier concentration/Fermi level position provide detection of non-parabolicity and establishment of real dependence of the electron energy on the wave vector, $E(\mathbf{k})$.

The method was first proposed and applied to studies of n-PbTe in [23] and then used widely for studying a variety of semiconductors and semimetals, in both bulk and thin film form, see, e.g., [24, 25]. In 1995 joint studies by Dr. T. Coutts (NREL) and Dr. V. Kaydanov (CSM) were started, aimed at applying the method to investigation of TCO materials. It is hard to overestimate the contribution of W. Mulligan and D. Young to these studies. Both were CSM Ph.D. students advised by T. Coutts and V. Kaydanov. Dr. Mulligan created the first system that provided measurements of the four coefficients in typical TCO thin films and performed preliminary experiments on cadmium stannate [27]. Dr. Young has developed new, more perfect and sophisticated measurement equipment and performed systematic comparative studies of a variety of TCO thin polycrystalline film materials [18, 19, 20, 28].

Hall effect measurements provide the carrier concentration. In a weak magnetic field ($\mu B << 1$),

$$R_H = A_R / qN \,, \tag{2.24}$$

where $q = -e$ for electrons and $q = e$ for holes. The Hall factor, A_R, which is isotropic for spherical and single-ellipsoid constant-energy surfaces, is very close to 1 in the case of high degeneracy. For a multi-ellipsoid band in cubic crystals (like n-Si and n-Ge) it is also isotropic but its value depends on the anisotropy of the ellipsoids. It is given by

$$A_R = \frac{3\beta(\beta+2)}{(2\beta+1)^2} \,, \tag{2.25}$$

where

$$\beta = \frac{m_{\parallel}}{m_{\perp}} \tag{2.26}$$

This brings some uncertainty in the determination of N, but fortunately not too high. For example, A_R=0.96 for β=2, and A_R=0.82 for β=10.

Combined measurements of ρ and R_H provide an estimate of the mobility. The so-called Hall mobility differs from the real drift mobility by the Hall factor, A_R:

$$\mu_H = |R| / \rho = A_R \mu \tag{2.27}$$

Combined measurement of Hall coefficient (carrier concentration) and Seebeck coefficient (thermopower) is one of the oldest methods used to estimate the effective mass in semiconductors. For a parabolic band and high degeneracy, the Seebeck coefficient is given by

$$\alpha = 8\pi \left(\frac{\pi}{3}\right)^{5/3} \frac{k_B^2 T}{qh^2} (r+1) \frac{m_d^*}{N^{2/3}} \tag{2.28}$$

Equation (2. 28) contains one more quantity to be determined, namely the scattering parameter, r. Using this equation without knowledge of the value of the scattering parameter, can lead to a rather inaccurate estimate of m_d^*. For example, if one assumes that the dominant scattering mechanism is due to acoustic phonons, for which r=0, one will obtain a value of m_d^* three times greater than that obtained if one assumes ionized impurity scattering, for which r=2.

The problem can be solved by measuring the resistivity and the transverse Nernst-Ettingshausen (N-E) coefficient along with the Hall and Seebeck coefficients. The thermo-magnetic N-E effect is defined by the equation [26]:

$$E_y = -Q \frac{dT}{dx} B_z \,. \tag{2.29}$$

For a parabolic band and with high degeneracy of the carrier gas, the N-E coefficient can be described by

$$Q = |\alpha| \mu_H \frac{r - 1/2}{r + 1} \quad (2.30)$$

Combining Eqs. (2.28) and (2.30), one obtains

$$m_d^*(E_F) = \left(\frac{3N}{8\pi^4}\right)^{2/3} \frac{eh^2}{k_B^2 T} \left(|\alpha| - \frac{Q}{\mu_H}\right) \quad (2.31)$$

and

$$r = \frac{3}{2} \frac{Q}{|\alpha| \mu_H - Q} + \frac{1}{2} \quad (2.32)$$

Thus, by measuring the four transport coefficients, one can determine both the DOS effective mass and scattering parameter. In the non-parabolic case equations (2.28) and (2.30) transform to

$$\alpha = 8\pi \left(\frac{\pi}{3}\right)^{5/3} \frac{k_B^2 T}{qh^2} \frac{1}{N^{2/3}} \left[m_d^*(r + 1 - \lambda)\right]_{E_F} \quad (2.33)$$

and

$$Q = |\alpha| \mu_H \left(\frac{r - 1/2 - \lambda}{r + 1 - \lambda}\right)_{E_F} \quad (2.34)$$

where

$$\lambda(E) \equiv 2\gamma(E) \frac{d^2\gamma}{dE^2} \left(\frac{d\gamma}{dE}\right)^{-2} = \frac{N}{m_d^*} \frac{dm_d^*}{dN} \quad (2.35)$$

It is easy to show that m_d^* can be calculated from the measured data using the same equation (2.31) as in the parabolic case. The scattering parameter is now defined as

$$r = \frac{3}{2} \left(\frac{Q}{|\alpha| \mu_H - Q}\right) + \frac{1}{2} + \lambda \quad (2.36)$$

To realize all the advantages offered by this method, we must have heavily doped samples of a material in a wide range of carrier concentrations/Fermi level positions. Based on measurements of the four transport coefficients, we are able to obtain the dependence $m_d^* = f(N)$. If $m_d^*(N) = const$, the deviations from parabolicity are negligible in this range of N and E_F, and, in subsequent analysis, we may reasonably use parabolic band theory. A substantial increase in m_d^* with carrier concentration indicates the need to use the more general non-parabolic band theory. Using the experimental dependence $m_d^* = f(N)$, with equations (2.20) – (2.22), we can

reconstruct the function $\gamma(E)$ and, hence, $E(k)$. The scattering parameter data enable us to identify the dominant scattering mechanism and to monitor its changes as a function of carrier concentration.

It should be mentioned here that the empirically established correlation between Seebeck coefficient, α, and carrier concentration can be used to map the carrier concentration distribution over the sample area of a thin film. Measurement of the local Seebeck coefficient, at various positions on the surface, by relocating the thermoprobe, is a non-destructive and simple method that may be applied to films of an arbitrary size and shape.

2.3.2 Optical characterization (ultra-high frequency electron transport).

The high electrical conductivity in metals and heavily doped semiconductors, and its dependence on frequency, significantly influences the optical properties of these materials and, in particular, the transmittance and reflectance spectra. The electrical conductivity is a complex value and depends on frequency of the electric field. It is given by

$$\sigma(\omega) = \frac{\sigma_0}{1 - i\omega\tau} \tag{2.37}$$

where σ_0 is the stationary (DC) conductivity, which is defined as

$$\sigma_0 = e^2 N\tau / m_c^* \tag{2.38}$$

The real and imaginary parts of the dielectric permittivity are described by equations:

$$\mathrm{Re}\,\varepsilon = \varepsilon' = n^2 - k^2 = \varepsilon_\infty\left(1 - \frac{\omega_p^2}{\omega^2 - \omega_c^2}\right), \tag{2.39}$$

and

$$\mathrm{Im}\,\varepsilon = \varepsilon'' = 2nk = \varepsilon_\infty\left(\frac{\omega_p^2\omega_c}{\omega\left(\omega^2 + \omega_c^2\right)}\right). \tag{2.40}$$

n and k are the refractive index and extinction coefficient, respectively, ε_∞ is the "high-frequency" dielectric permittivity due to the bound electrons. Two characteristic frequencies: ω_p and ω_c, are totally defined by the free carriers. The plasma frequency, ω_p, is related to the carrier concentration and conductivity effective mass by equation (2.7). The collision frequency, ω_c, is the reciprocal of the relaxation time, $\omega_c=1/\tau$.

When the frequency of an electromagnetic wave, ω, decreases approaching ω_p, reflectance and transmittance of the material change dramatically. If $\omega_c \ll \omega_p$, then, to a first approximation,

$$\varepsilon \approx \varepsilon' = \varepsilon_\infty\left(1 - \omega_p^2/\omega^2\right) \tag{2.41}$$

When ε is real and negative ($\omega < \omega_p$), the solutions to the wave equation decay exponentially in the material; i.e. no radiation can propagate. Thus at $\omega = \omega_p$, a sharp increase in reflectivity, known as the "plasma reflectivity edge", should be observed. For real conductors, ω_c/ω_p is usually not so small, therefore reflectance does not change so rapidly when the frequency approaches ω_p. The analysis of the measured optical spectra (by, for example, spectrophotometry or ellipsometry) allows the plasma and collision frequencies to be determined.

Based on the plasma frequency and Hall carrier concentration data, it is possible to calculate the conductivity effective mass, m_c^*, using Eq. 2.7. Comparison of m_c^* with m_d^* (see Eqs. 2.6 and 2.9) provides guidance about the shape of the constant-energy surfaces, and, in particular, enables a distinguishing between the single-valley and multi-valley models. For a single-ellipsoid model this comparison enables an approximate estimation of the deviation from the spherical shape. In principle, measuring dependence $m_c^*(N)$ provides establishing of non-parabolicity and reconstruction of $\gamma(E)$ and $E(k)$ dependencies in the same way as $m_d^*(N)$. The coincidence of the results obtained from Hall and optical measurements could be considered as evidence of their reliability. This is important because each of the methods used has its own sources of errors, both technical (like non-accurate measurements, not-too-high uniformity of the samples) and theoretical (validity of the theories behind the methods).

The empirically established dependence $\omega_p(N)$ for a particular material provides an alternative to the Hall effect method for measuring carrier concentration and its uniformity over the thin film area. Multi-angle spectroscopic ellipsometry, with appropriate modeling of the raw data, provides a unique option to test the uniformity of N and μ (via ω_p and ω_c) over the film thickness [29, 30].

Based on the m_c^* and ω_c data, derived from the optical characterization, one can calculate the *optical mobility,* defined as

$$\mu_{opt} = \frac{e\tau}{m_c^*} = \frac{e}{m_c^* \omega_c} \qquad (2.42)$$

which is not necessarily the same as the Hall mobility. Comparison of the two provides guidance about contribution of the grain boundaries to the measured DC sheet resistance and bulk resistivity.

2.3.3 Evaluation of the grain boundary contribution to the film sheet resistance.

A significant difference is usually observed between resistivity measured on a single crystal and thin film polycrystalline samples of the same semiconductor with the same carrier concentration. This difference is commonly attributed to the influence of grain boundaries and treated in terms of “GB scattering”. This terminology is not always correct and sometimes can be misleading. Indeed, GBs disturb the translation symmetry of the crystal and inevitably cause the free carrier scattering. But the GB scattering coexists with scattering by phonons, point defects, dislocations, etc. The total scattering rate is the sum of the particular ones. The contribution of GB scattering

is significant only if the grain size, d, is comparable to the mean free path, l, due to all the scattering mechanisms. In typical polycrystalline thin TCO films the l value estimated based on the mobility and carrier concentration is rather small: $l \leq 100$Å, while $d \geq 1000$Å.

Thus, we have to use a different approach to the problem. We must regard a TCO polycrystalline film as having two phases. One of these is the material inside the grains (bulk material), and the other is that at grain boundaries. The equivalent electrical circuit of the sample can be constructed as a series connection of resistors, R_B and R_{GB}, representing bulk material and grain boundaries, respectively. When measuring the DC resistance of the film, we obtain the sum of these two types of resistors. Thus the measured bulk resistivity, ρ, relates to the real resistivity in the grain bulk, ρ_B, as

$$\rho = \rho_B \left(1 + R_{GB} / R_B\right). \tag{2.43}$$

The R_{GB}/R_{GB} ratio can be estimated based on comparison of the optical and Hall mobilities. Scattering in the grain bulk dominates the collision frequency, ω_c, if the grain size, d, is much greater than the mean free path, l, which is the case for TCOs. Thus the optical mobility defined by Eq. (2.42) is close to the real drift mobility in the grain bulk. The Hall mobility is determined by the Hall coefficient and DC resistivity measurements: $\mu_H = R_H / \rho$. Hence the measured Hall mobility due to the influence of GB can differ significantly from the real mobility in the grain bulk. Supposing the Hall factor $A_H \approx 1$ and using Eqs. (2.42) and (2.43), we obtain the equation that enables estimation of the GB contribution to the resistivity:

$$\frac{R_{GB}}{R_B} = \frac{\mu_{opt}}{\mu_H} - 1 \tag{2.44}$$

One may expect that in the heavily doped semiconductors, such as TCOs, the effect of grain boundaries on sheet resistance should not be too pronounced. The electrical charge located at grain boundaries, due to trapping of majority carriers by the GB electron states, creates a potential barrier for majority carriers. With increasing doping level, the amount of the trapped charge also increases, as does the height of the potential barrier. With the further increase in doping level, eventually all the grain boundary states are filled with trapped carriers and the charge cannot increase any more. However the space charge density in the depletion region continues to increase causing a reduction in the height and width of the potential barrier, allowing tunneling. Moreover, for a very high doping level, the potential barrier is well below the Fermi level and the electrons pass over the barrier without being remarkably perturbed by it [31, 32].

It should also be mentioned here that the other method for studying electrical properties of the GB described in Sec.1, namely Impedance Spectroscopy, is not applicable to the high conductivity TCO films. The limitation is put by the value of the product of the film resistance, R_{sh}, and capacitance, C_{sh}, which defines characteristic frequency of the sample, $\omega_o = (R_{sh}C_{sh})^{-1}$. For the 1 μm thick film with a grain size of 1 μm, $R_{sh} \sim 10$ Ω/□ and $C_{sh} \leq 0.1$ pF/□. Thus, $\omega_o \geq 10^{12}$ rad/s = 160 GHz which is far beyond the frequency limit of our LCR meters.

2.4 Experimental Studies of Thin TCO Films

2.4.1 Tin oxide films doped with fluorine

The studies presented in this section illustrate the method based on combination of transport phenomena measurement and optical characterization of a material.

Experimental details

SnO_2:F thin films were prepared at CSM in collaboration with Dr. J. Xi from Green Development, LLC., by atmospheric pressure chemical vapor deposition. Films for studies were selected with the thickness of 350-600 nm, which is typical for practical applications. The top surface roughness did not exceed 10% of the film thickness. The average grain size determined with AFM and SEM for many films was in a range from 130 to 200 nm.

Electrical characterization included measurements of DC resistivity ρ, Hall coefficient R_H, and Hall mobility μ_H measured with a Bio Rad HL 5500 PC Hall Effect Measurement System (van der Pauw geometry). The Seebeck coefficient S (thermopower) was measured at room temperature with a simple home made equipment. Optical properties were studied by using multiangle spectroscopic ellipsometry (a © J. A. Woollam Co. Inc. VASE® system). Modeling based on the Drude model provided data on plasma frequency ω_p and collision frequency ω_c, the parameters that are totally defined by free carriers.

Band spectrum, Fermi level position

The analysis of the experimental data was based on the theory of electron transport phenomena presented in Sections 2.2 and 2.3 specified for the case of isotropic band spectrum and high degeneracy of the free electron gas. Indeed, according to [33], the conductance band structure in SnO_2 is described by a single ellipsoid model. The longitudinal and transverse effective masses (parallel and perpendicular to the revolution axis of the constant energy ellipsoid) are: $m_{\parallel}$*=0.234m$_0$ and $m_{\perp}$*=0.299m$_0$. Thus the anisotropy of ellipsoid in ***k***-space is rather low: $k_{\|}/k_{\perp}\approx 0.9$. The values of the conductance and density of states effective masses calcuated using Eqs. 2.6 and 2.9b are practically the same: $m_c^*=0.274m_0$, $m_d^*=0.276m_0$. This allows assumption of an isotropic spectrum. Then, the free electron concentration determined by Hall measurements varied in the range of 1.8×10^{20} to 5.9×10^{20} cm^{-3}. This high electron concentration together with the low magnitude of the measured Seebeck coefficient (-20 to -40 μV/K) indicates high degeneracy of the electron gas in all samples at room temperature.

The next problem is whether there are considerable deviations from parabolic spectrum. To clarify the problem we have analyzed the plasma frequency, ω_p, dependence on the electron concentration, *N*. The latter was determined from Hall measurements as $N=(-eR_H)^{-1}$ because the Hall factor in Eq. (2.24) is $A\approx 1$ for the single ellipsoid spectrum and high degeneracy of the free carrier gas. According to Eq. (2.7), $\omega_p^2 \propto N$ if the effective mass does not depend on carrier concentration (Fermi level). The experimental data (see Fig. 2.1a) demonstrate just this kind of dependence within the accuracy of measurements. Thus no considerable deviation from parabolic spectrum takes place in the studied concentration range. This is confirmed by the

Seebeck coefficient dependence on carrier concentration (Fig. 2.1b) which is very close to $S \propto N^{-2/3}$, in accordance to Eq. (2.28).

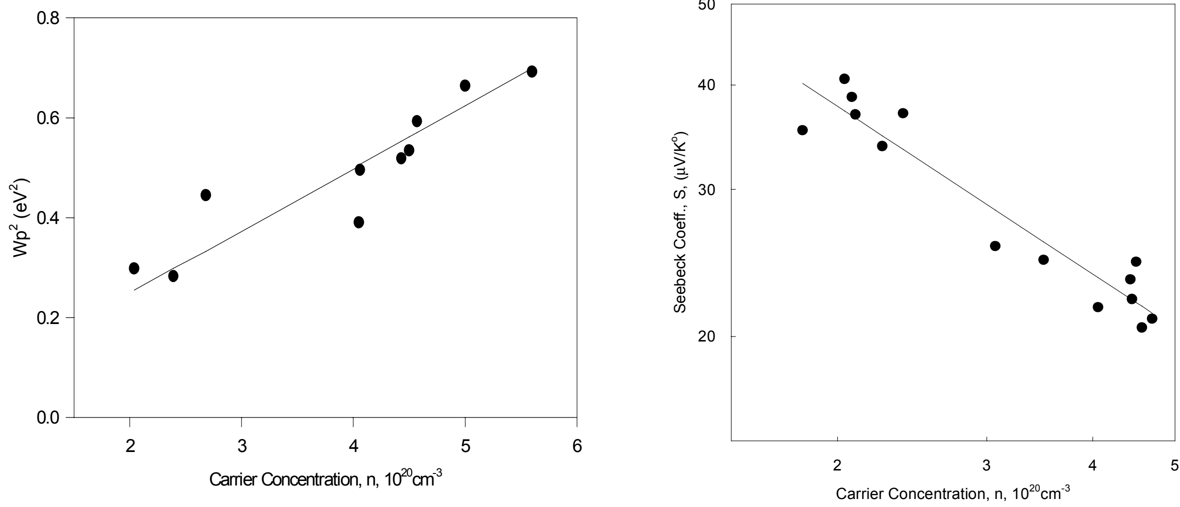

Fig. 2.1 Dependence of plasma frequency (a) and Seebeck coefficient (b) on electron concentration.

The conductance effective mass value determined from the slope of the graph in Fig. 2.1a is: $m_c^* = (0.28 \pm 0.01)m_o$, which is very close to the values $0.274m_o$ and $0.276m_o$ for the conductance and DOS effective masses presented in Ref. 33. In our further analysis we will use the isotropic and parabolic band approximation with $m_d^* = m_c^* = 0.28m_o$. The Fermi energy E_F calculated using this effective mass value and Eq. (2.10) varied in range of 0.4 to 0.9 eV for carrier concentrations in the range of 1.8×10^{20} to 5.9×10^{20}cm^{-3}.

Mobility

The Hall and optical mobility values defined by Eqs. (2.27) and (2.42) and measured on several typical SnO_2 films are presented in Table 2.1. All films were prepared with the same deposition technique and fluorine concentration, while the duration of deposition and the oxygen pressure during post-deposition treatment were varied. It is seen that for samples #3-8 the μ_H and μ_{opt} values are close to each other. For the first two samples the Hall mobility is much lower than the optical one. This difference is likely provided by the influence of grain boundaries on the measured resistivity, hence on the Hall mobility.

Table 2.1. Comparison of the Hall and optical mobility values

Sample #	Thickness (nm)	Concentration ($10^{20}cm^{-3}$)	Mobility (cm^2/Vs)	
			μ_H	μ_{opt}
1	110	5.9	4.5	21
2	60	4.0	4.5	32
3	370	5.6	25	26
4	330	5.2	30	32
5	500	4.6	29	30
6	470	3.1	11.5	12
7	500	3.2	12	12
8	520	3.0	11	11

Scattering by grain boundaries can be neglected to the first approximation because the grain size is much greater than the mean free path length l. In the case of high degeneracy, the only carriers that contribute to electron transport are those having energy close to the Fermi level. Thus the mean free path can be estimated by using the equations:

$$l = v_F \tau_F ; \quad \tau_F = \mu m^* / e ; \quad v_F m^* = P_F = h(3N/8\pi)^{1/3} \rightarrow$$

$$l = \left(\frac{3N}{8\pi}\right)^{1/3} \left(\frac{h}{e}\right) \mu \qquad (2.45)$$

where v_F, τ_F, P_F are respectively the velocity, relaxation time and electron momentum of an electron at the Fermi level, N and μ are the measured concentration and mobility. Even for the samples of highest mobility, the estimated value of l does not exceed 10 nm while the grain size is above 100nm.

Thus we must use another approach to the discussion of the GB influence that is based on treating the polycrystalline material as a two-phase system (see Sec. 2.3.3). One phase is the bulk material inside grains, and the other phase is the GB region. Eq. 2.44 was used to evaluate the ratio of contributions of GBs and bulk material to the in plane resistance, R_{GB}/R_B. In this model the optical mobility is not impacted by grain boundaries as long as the grain size is much greater than the mean free path. The collision frequency is determined by scattering processes occurring in the bulk of a grain, and is a reciprocal of the bulk relaxation/collision time, τ. Thus μ_{opt} is a better measure of a real mobility in the grain bulk. If the μ_H and μ_{opt} values are close to each other, that means that contribution of GB to the film resistance is negligible ($R_{GB} << R_B$). Table 2.1 shows that grain boundaries significantly increase resistivity only in thin films, while their influence is rather low in films thicker than ~300 nm.

The last three samples in Table 2.1 were annealed in an atmosphere enriched with oxygen, and exhibit almost equal values of μ_H *and* μ_{opt}, hence the impact of GB is insignificant. At the same time they demonstrate mobilities much lower than other thick films. This difference can be

attributed to the partial compensation of the fluorine donors by uncontrolled acceptor centers. We have compared these samples (set 1) with the samples cut from the same SnO_2/glass plate and annealed in standard atmosphere (set 2). The latter had an average electron concentration of 5.3×10^{20} cm^{-3} and an average mobility of ~30cm^2/Vs. If it is supposed that the donor concentration is the same in both sets, $N_d \approx 5.3 \times 10^{20}$ cm^{-3}, then the concentration of single charged acceptors is $N_a \approx 2.2 \times 10^{20}$ cm^{-3}. The density of the scatterers (ions) in the set 1 samples is $N_{sc}=N_d+N_a \approx 7.5 \times 10^{20}$ cm^{-3}, that is ~1.4 times greater than in the set 2. For the ion impurity scattering in highly degenerate material, $\mu \propto \eta^{3/2}/N_{sc} \propto n/N_{sc}$, where $\eta \equiv E_F - E_c$ is the distance between Fermi level and the conductance band edge. Thus the ratio of mobilities in the two sets should be $\mu_1/\mu_2 \approx 0.3$, which is close to the measured ratio.

Scattering mechanism, theoretical estimates of mobility

For these studies we selected presumably uncompensated samples with $\mu_H \approx \mu_{opt}$. The uniformity of electronic properties in plane was checked with thermoprobe (thermopower) and the four-point-probe method (resistivity). Ellipsometry measurements were used to check uniformity of the plasma and collision frequencies (electron concentration and mobility) across the film thickness.

Mobility measurements in the temperature range of 300 to 500K did not reveal any $\mu(T)$ dependence; hence one can exclude phonon scattering. As to the scattering by neutral defects and impurity ions, we can distinguish them based on the scattering parameter value, r. The latter is defined by the relaxation time dependence on energy (see Eq. 2.17). For neutral hydrogen-like impurity centers r = 1/2, for centers with the δ-type scattering potential r = 0, and for the impurity ions r =2 [34]. We have derived the scattering parameter from the Seebeck coefficient data by using the equation:

$$S = \frac{k_B}{e}\frac{\pi^2}{3}(r+2)\frac{k_B T}{\eta} \qquad (2.46)$$

For the electron concentration in the range of 2×10^{20} to 5.5×10^{20} cm^{-3}, the obtained value of r varied from 1.2 to 1.5, which is considerably higher than that for the first two mechanisms mentioned above. The discussion below will show that screening of the ion Coulomb potential by free carriers (FSC) can yield this range of r. In this case, the scattering potential is $U = \frac{Q}{\varepsilon R}\exp\left(-\frac{R}{R_o}\right)$, where ε is a dielectric constant, R is a distance from the ion center and R_o is a screening radius which is defined for highly degenerate semiconductors by [34]

$$R_o = \left[\frac{(\pi/3N)^{1/3}(\varepsilon h^2)}{16\pi^2 m^* e^2}\right]^{1/2} \qquad (2.47)$$

This and the following equations are written in the CGS system.

To calculate the scattering parameter we used the theory presented in [35, 36 and 34]. The dependence of relaxation time on energy for scattering by screened impurity ions can be written in the form:

$$\tau(E) = \left\{ \frac{(2m^*)^{1/2} \varepsilon^2}{\pi e^4 N_i \Phi(\xi)} \right\} E^{3/2} \tag{2.48}$$

$$\Phi(\xi) = \ln(1+\xi) - \frac{\xi}{1+\xi}; \ \xi = (2k_F R_o)^2; \ k_F = (3\pi^2 N)^{1/3} \tag{2.49}$$

where N_i is the impurity ion concentration , $\Phi(\xi)$ reflects the influence of SFC, and k_F is the Fermi wave vector magnitude. The derived expression for the scattering parameter is:

$$r = 2 - \left(\frac{d \ln \Phi}{d \ln \xi} \right)_{E=\eta} = 2 - \frac{\xi^2}{\Phi(1+\xi)^2} \tag{2.50}$$

The screening radius value calculated with Eq. 2.47 is of the order of the unit cell size or lower. This raises the problem of spatial dispersion of the dielectric constant. The dielectric constant ε in Eqs. 2.47 and 2.49 is a sum of (a) the high frequency dielectric constant, ε_∞, provided by polarization of the atomic electron shells and (b) the lattice dielectric constant, ε_L, provided by displacement of the lattice ions ($\varepsilon=\varepsilon_\infty + \varepsilon_L$). Confining the perturbation potential to a volume of the order of the unit cell decreases the contribution of the second mechanism so that the effective dielectric constant is somewhere between ε_∞ and ε_0 (static dielectric constant). Fortunately, the scattering parameter calculations provided values only slightly different for ε_0=10 and $\varepsilon_\infty = 4$ (see data for ε in SnO_2 in [33]). For the carrier concentrations of 2x10^{20} to 5.5x10^{20} cm^{-3}, the results of calculations ($1.3 \leq r_{calc} \leq 1.5$) are in a good agreement with the data derived from the Seebeck coefficient measurement ($1.2 \lesssim r_{exp} \lesssim 1.5$). This result verifies impurity ion scattering with SFC as a dominating mechanism in our films.

Studies presented above enabled us to calculate mobility as $\mu=e\tau/m^*$ and compare the calculated and measured data. The effective mass was assumed to be isotropic, independent of the carrier concentration, and equal to 0.28 m_0. The mobility was calculated for $N = 5\times10^{20}$ cm^{-3} and varying dielectric constant, assuming singly charged donors and no compensation, and varied from ~80 cm^2/Vs ($\varepsilon=\varepsilon_0$) to ~20 cm^2/Vs ($\varepsilon=\varepsilon_\infty$). The best fitting for the highest measured mobility of 35 cm^2/Vs was obtained with ε=5.3.

2.4.2 Application of the four-coefficient method: ZnO films

Measurement techniques and experimental procedure

The four-coefficient instrument created at NREL with our participation has already been described and discussed in detail in [19, 28]. Here we present only a brief review of its principal features and operation.

Thin film TCO samples are deposited on electrically insulating substrates and are etched photolithographically to the pattern schematically shown in Fig. 2.2b. Two copper blocks with embedded electrical heaters control the sample temperature and the temperature gradient in vertical direction when measuring Seebeck and Nernst-Ettingshausen (N-E) effects. The copper blocks have a differential thermocouple mounted between them to measure the temperature gradient across the sample. One of the blocks has an additional embedded thermocouple for absolute temperature measurement. The entire sample holder is cooled by a closed-cycle helium cryostat for temperature-dependent measurements from 30 to 350 K.

Hall effect and resistivity are measured with the van der Pauw method by using electrical contacts 1, 2, 3, and 4. The Seebeck voltage is measured between contacts 1 and 3, and N-E voltage is measured between contacts 2 and 4. Note that the temperature gradient is applied parallel to the short dimension of a sample while the N-E voltage is measured in the long dimension. This geometry of the sample orientation is different from the traditional geometry (see, e.g., [23]) presented schematically at Fig. 2.2a. The latter is similar to the Hall bar geometry where current flows along the long side of a sample and Hall voltage is measured along the short side. The reason for changing geometry is that the N-E coefficient is very small in TCOs. Indeed, this coefficient is proportional to mobility and the ratio $k_BT/(E_F-E_C)$, see Sec.2.3.1. Both parameters are small for typical TCOs, so that for the reasonable values of magnetic field and temperature difference across the sample, the N-E signal is in the nano-volt scale.

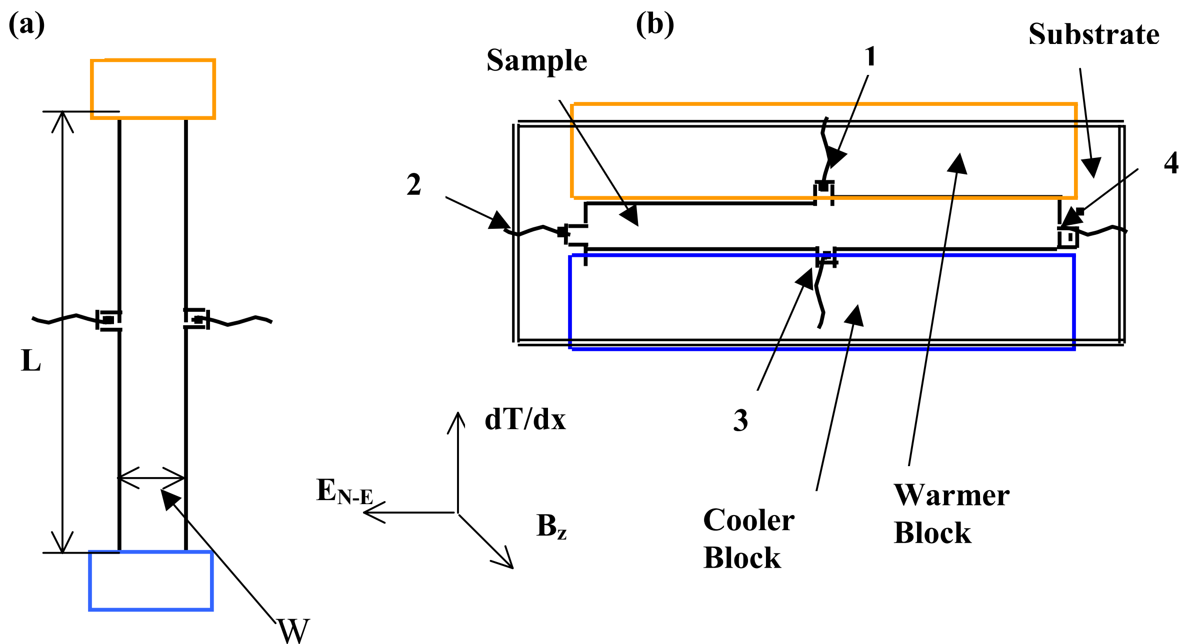

Fig. 2.2 Comparison of two types of geometry used for the N-E effect measurements. (a) traditional geometry; (b) geometry used in our instrument.

Let us rewrite the Eq. 2.29 for the N-E effect in terms of temperature difference across a sample, $\Delta T=(dT/dx)L$, and the N-E voltage, $V_{N-E}=E_{N-E}W$, where L and W are the sample dimensions shown in Fig. 2.2a. The new equation is

$$V_{N-E} = Q \times \Delta T \times B_z \times \frac{W}{L} \tag{2.51a}$$

For the geometry shown in Fig. 2.2b this equation transforms to

$$V_{N-E} = Q \times \Delta T \times B_z \times \frac{L}{W} \tag{2.51b}$$

where L and W are the lengths of the long and short sides of a sample respectively. It is seen that rotation of the sample by the angle of 90° with respect to the temperature gradient direction leads to the $(L/W)^2$ fold increase in the N-E signal. For the real samples we use, L=16 mm and W=3mm, that is $(L/W)^2$=28.4. Thus using the geometry of Fig. 2.2b we provided a significant increase in the N-E voltage while preserving a reasonably small temperature difference across the sample, of 10 K or less. This geometry was proposed and realized first in [37].

Some results and discussion

To demonstrate the applicability of the method to studies of TCOs and illustrate typical information provided by these measurements, we review here briefly the data obtained for ZnO thin films and presented in [19]. The films were RF magnetron-sputtered on 7059 glass substrates. The DOS effective mass m_d* was studied with the FC method in the carrier concentration range of $2x10^{19}$ to $5x10^{20}$ cm^{-3}. The obtained value of m_d* varies in this range from 0.3 to 0.45 m_o indicating non-parabolicity of the conductance band. The plot of m_d* vs. $N^{2/3}$ is linear indicating the first-order non-parabolicity in this concentration range. Extrapolation of the plot to N =0, provided m_{do}*=0.27 m_o (m_{do}* is the DOS effective mass at the conduction band bottom). The plasma-frequency conductivity effective mass values for the electron concentrations of $4x10^{19}$ and $5x10^{20}$ cm^{-3} taken from literature [38, 39] are in a good agreement with m_d*, considering the deviation from the parabolic spectrum. Besides, the difference between m_d* and m_c* is rather small which corresponds to the single-valley band in agreement with the theory prediction [40]. The constant-energy surfaces shape is close to sphere. Within the accuracy of measurements the ratio of the ellipsoid principal axes lengths does not exceed 1.5.

The scattering parameter r values were determined as described in Sec. 2.31, using Eq. 2.36 with the non-parabolicity parameter λ (Eq. 2.35) values derived from the experimental dependence $m_d^*(N)$. For heavily doped ZnO:Al samples ($N \geq 4x10^{20}$ cm^{-3}) the r value matches well with that for the impurity ion scattering. For the undoped material ($N \sim 2x10^{19}$ cm^{-3}), the scattering parameter was found to lie closely with the value for neutral impurity scattering.

It is interesting to compare data for ZnO with those for Cd_2SnO_4 (CTO). CTO films were also prepared with the RF magnetron sputtering. Free electron concentration varied between $2x10^{20}$ and $6.8x10^{20}$ cm^{-3}. The DOS effective mass increases with the carrier concentration, but much slower than in ZnO, only by a factor of 1.2 in the concentration range indicated above. The m_d* value in CTO is smaller than in ZnO, by a factor of 1.8 for N =$4x10^{20}$ cm^{-3}. Probably this difference accounts for mobilities in CTO being nearly 3 times larger than in ZnO. First,

mobility is reversely proportional to effective mass, and second, the lower effective mass, and hence lower density of states leads to the reduced scattering rate. Indeed, the estimated relaxation time value for $N= 4x10^{20}$ cm^{-3} in CTO is ~1.6 times that value for ZnO. It is important to point that comparison of the Hall and optical mobilities in both materials differ only slightly indicating no considerable impact of grain boundaries on the film sheet resistance. The same conclusion was made previously in [29, 30] about SnO_2:F films, see also Sec. 2.4.1.

2.5 Conclusions

- Combined experimental studies of electron transport phenomena in stationary external fields and in ultra high-frequency electromagnetic fields (optical characterization) provide a unique opportunity for investigation of band spectrum and scattering processes in heavily doped semiconductors with low mobilities.
- Based on these studies one can determine effective mass and its dependence on the carrier energy (Fermi level position), the shape of the constant energy surfaces, relaxation time and dominating scattering mechanism.
- Comparison of the Hall and optical mobility values enables estimating contribution of grain boundaries to the film sheet resistance.
- The techniques and equipment developed at NREL in cooperation with School of Mines provides measurements on the TCO thin films of resistivity, Hall, Seebeck and Nernst-Ettingshausen effects in a wide temperature range. Using the multi-angle spectroscopic ellipsometry proved to be a convenient and reliable method for determination of the plasma and collision frequencies and variations of these parameters across the film thickness. The latter, being combined with the in plane mapping sheet resistance (four-point-probe method) and Seebeck coefficient (thermoprobe), provide a convenient non-destructive method for evaluation of spatial uniformity of electronic properties of a film.

3. NEAR FIELD SCANNING OPTICAL MICROSCOPY (NSOM) OF CdTe/CdS SOLAR CELLS

To clarify the role of polycrystallinity in forming opto-electronic properties of thin film CdTe/CdS solar cells, it is important to use characterization techniques with high spatial resolution. Morphological studies (SEM, AFM) of the CdTe absorber layer show that the grain size is usually one to several microns. Hence we need the tools that provide testing of composition, optical and electronic properties of a material with a spatial resolution on the order of 0.1μm or lower. Along with the scanning tunneling microscopy and spectroscopy, the NSOM is one of the most promising techniques. In our facilities this method and instrumentation were developed by Professor R.T. Collins and Graduate Research Assistant M.K. Herndon. In this section we present results that demonstrate the effectiveness of NSOM for studies and two-dimension mapping of current collection over the cell cross section. One of the major goals of the experiments was to study the interdiffusion of S into CdTe by using the compositional dependence of the ternary $CdTe_{1-x}S_x$ phase band gap and NSOM.

Post growth annealing of the CdTe/CdS films has been shown to enhance the performance of solar cells. Substantial evidence exists that interdiffusion between CdTe and CdS layers occurs during growth and post growth annealing processes [41]. In particular, S diffusion into the CdTe layer leads to the formation of a ternary $CdTe_{1-x}S_x$ phase within the CdTe layer. For S concentrations less than ~25%, bowing in the bandgap of the ternary as a function of x reduces the band gap as S content increases. This leads to a decrease in the low energy cutoff of the device relative to pure CdTe [42]. Various models for the mechanism of S diffusion have been developed, and it is generally believed that grain boundaries must play a role in the diffusion process. However this has been difficult to verify experimentally. This study provides evidence that S diffuses preferentially along the grain boundaries in CdTe.

3.1 Experimental Techniques and Procedures

The samples used in these measurements were grown on soda-lime glass coated with a tin oxide TCO. Chemical bath deposition was used to grow a ~200 nm thick CdS layer on the SnO_2. CdTe was electrochemically deposited on the CdS layer to a thickness of 3-4 μm. The sample was treated with $CdCl_2$ and annealed at 365°C. Previous work has shown interdiffusion can be observed after the 365°C anneal, and increases significantly with temperature. By increasing the anneal temperature to 450°C, a nearly uniform S concentration is observed throughout the film [43]. Gold was evaporated through a shadow mask to form a back contact and define individual devices. Capacitance-voltage measurements gave a zero bias depletion width of ~1.5 μm for the diodes and doping level of ~5 $x10^{14}/cm^3$ in the CdTe.

The glass side of the sample was scribed in the region under a device and broken to expose a cross section of the device. It was mounted so that spatially resolved photocurrent and topographic images of the cross section could be measured with the NSOM. The NSOM is a home built instrument that operates in air. The experiments were done at room temperature. The NSOM probe was made from a single mode optical fiber which was tapered using a micropipette puller and metal-coated, leaving a ~100nm diameter aperture at the tip [44]. The probe was raster scanned across the sample cross section using optically detected shear force feedback to maintain

a constant separation of approximately 10nm between the probe tip and sample [45]. Monitoring the feedback signal while raster scanning the sample allowed the topography of the cleaved surface to be measured.

A tunable Ti:Sapphire laser and a 632.8nm HeNe laser were simultaneously coupled into the fiber probe allowing it to be used as an excitation source. Each laser was chopped at a different frequency before being coupled into the fiber. The photocurrent generated in the CdS/CdTe diode was detected for each wavelength using two lock-in amplifiers. The outputs of the lock-in amplifiers were recorded at each point as the sample was scanned. This allowed two spatially-resolved measurements of the generated photocurrent, one for each wavelength of light, to be recorded simultaneously with the surface topography.

Scans of the cell cross section began on the glass side of the junction, and progressed toward the back of the CdTe layer. The same area was scanned several times, each with a different wavelength from the Ti:Sapphire laser, in order to see variations in collection as a function of excitation energy. The HeNe images, taken simultaneously with each Ti:Sapphire measurement, were compared from scan to scan. This reference enabled us to ensure that variations in the Ti:Sapphire measurements were due to changes in excitation wavelength and not due to changes in the probe or scanning conditions.

The band gap of the $CdTe_{1-x}S_x$ ternary phase decreases as a function of x (for $x \leq 0.25$) from ~1.51eV at x=0 to 1.41eV at x=0.25 [46-48]. This dependence of band gap on x allows changes in excitation energy during NSOM measurements to be used to observe spatial variations in the S composition of the $CdTe_{1-x}S_x$ ternary across the heterojunction, and therefore to identify regions of high S content. In the discussion below we have used the bandgap dependence of Ref. [49] to associate optical excitation energies with specific S concentrations. In general, however, the band edge of polycrystalline films shows inhomogeneous broadening due to effects such as strain, defects, and alloying, which can lead to an apparent bandgap which is lower than that for crystalline material. Because of this broadening and the uncertainties in the reported composition dependence of the $CdTe_{1-x}S_x$ band gap, relative changes and spatial variations in S composition found from optical measurements are likely to be much more reliable than the numerical S compositions inferred from the measurements. The later should probably be viewed as correct to within a few percent.

3.2 Experimental Results and Discussion

Figure 3.1 shows a topographic image and three photocurrent images, each produced using a different excitation energy. The images are 4.8 x 4.8 μm. The topography measurements showed an average grain size of 1-2 μm. A small amount of drift occurred between scans. Comparison of the locations of individual grains seen in the topographic images allows us to track this drift. The layers present in the film have been identified adjacent to Figs. 3.1a and 3.1b. The interface between the glass and film is evident as the horizontal feature across the bottom of the topography image. One obvious grain, which will be discussed in more detail below, has been outlined on the topography plot (Fig. 3.1a). The topography measurements obtained in registry with each photocurrent measurement were used to locate this feature in subsequent scans, allowing this region to be identified in the photocurrent images in Figs. 3.1b-3.1d.

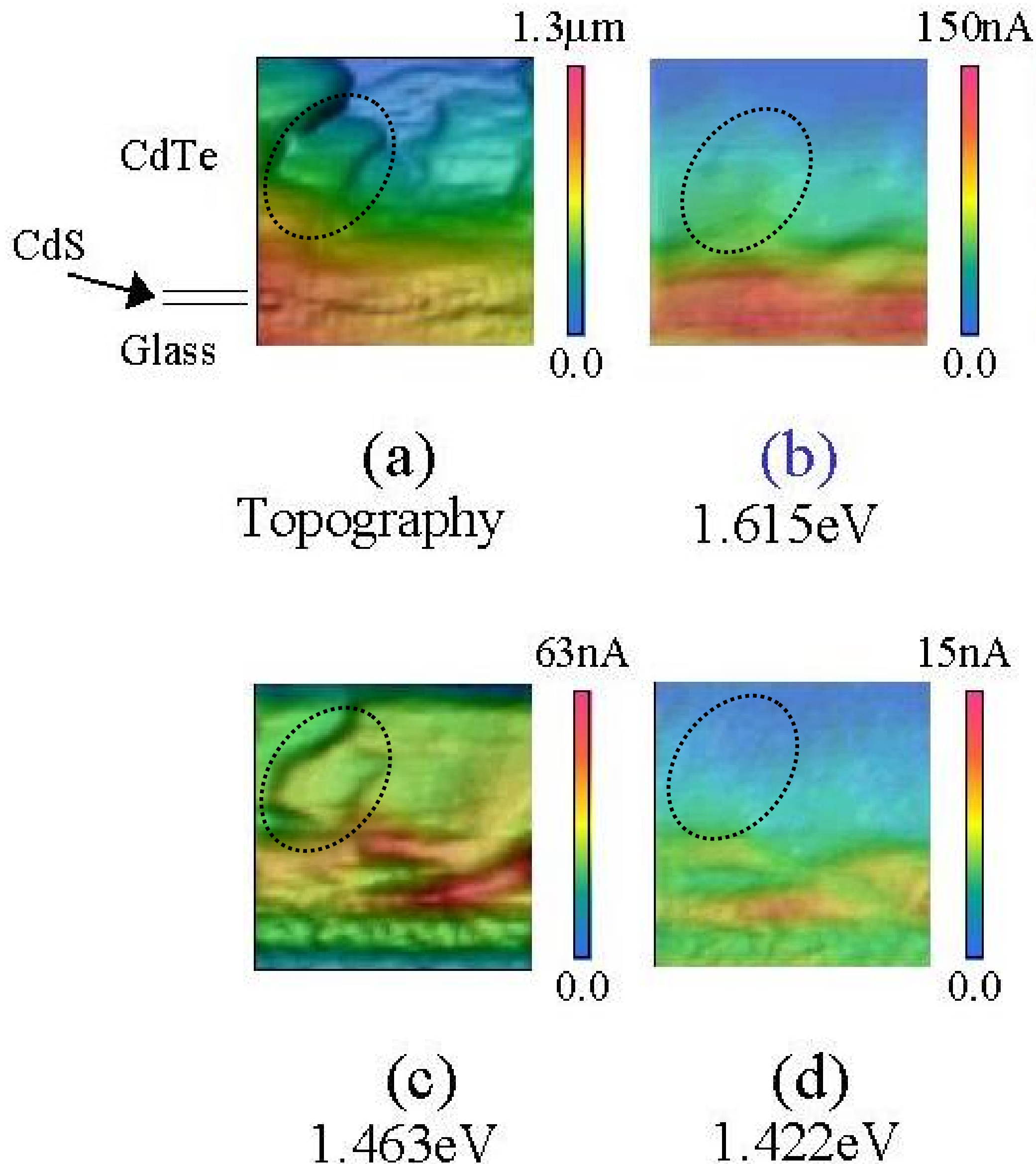

Fig. 3.1. Topography (a) and photocurrent (b-d) NSOM images taken on the cross section of a CdS/CdTe solar cell. The same grain has been outlined in the topography and in each of the photocurrent images. The shift in its position is due to drift, which was tracked using the topographic images. (b) The excitation energy of 1.615eV is above the CdTe bandgap. (c) The excitation energy of 1.463eV is ~50 meV below the CdTe bandgap. Increased width of the collection region in the CdTe layer is observed compared to (b). For the marked grain, the collection is much greater at the boundary than in the interior. (d) The excitation energy is 1.422eV.

For 1.615 eV excitation (Fig.3.1b), which is a little more than 100 meV above the CdTe bandgap, we see the photocurrent is strongly peaked near the junction, and decreases toward the back of the device. This is typical of measurements at energies above bandgap. In general, the photocurrent becomes even more strongly peaked near the CdTe/CdS junction as energy increases. As energy decreases below the CdTe bandgap to 1.463eV (Fig. 3.1c), corresponding to a S composition of 6%, the collection efficiency at the back of the device improves relative to that at the interface. We have observed this effect (a widening of the collection region at longer wavelength) in most edge cleaved semiconductor diodes we have studied. We attribute it to a competition between surface recombination and collection by the junction. At longer wavelengths, the light is absorbed further from the surface, allowing more of the carriers to be collected by the junction before recombining at the surface. Similar observations and conclusions were presented in Ref. 30. We note that the carrier collection region at this energy extends from the junction to the back of the device and that the average collection efficiency at the junction and near the back is roughly the same. Simplistically, the width of the collection region is determined by the depletion width and the minority carrier diffusion length. Since our depletion width is ~1.5μm, this indicates a minority carrier diffusion length of more than 2μm.

At 1.422eV (Fig.3.1d), the excitation energy is 80 meV below the CdTe band gap and corresponds to a S content of 16%. Here the width of the collection region has once again decreased. This is the result of carriers being generated mainly in the higher S content, lower bandgap, $CdTe_{1-x}S_x$ ternary phase, which is most likely to exist close to the CdS/CdTe junction. The S concentration we would infer near the junction in Fig.3.1d is larger than the reported immiscibility gap composition of ~6% at 415°C [41]. This may in part be due to the uncertainties in quantifying S concentration mentioned above.

For excitation energies below the CdTe band gap, a large amount of contrast was visible across the photocurrent images. For example, localized regions of higher photocurrent are visible near the interface in both Figs. 3.1c and 3.1d. Presumably this contrast arises from variation in S content and hence bandgap across these regions. A particularly interesting example of this contrast is seen in Fig. 3.1c where a loop of higher photocurrent is clearly visible within the outlined region. This correlates exactly with the boundary of the grain identified in Fig. 3.1a. To clarify the energy dependence of this feature, a series of measurements across this grain was recorded while varying the excitation energy from 30 meV above to 60 meV below the CdTe band gap. The results are shown in Fig. 3.2 where each line on the graph represents a single horizontal scan across the grain. Each scan was made at the same location using a different excitation energy.

In agreement with the data in Fig. 3.1, as energy decreases, the traces in Fig. 3.2 initially show an overall increase in the average value of the photocurrent, that is maximum for energies just below the CdTe bandgap. As excitation energy decreases further, the average value of the photocurrent drops. Nearly all the signal has disappeared in the 1.44eV scan.

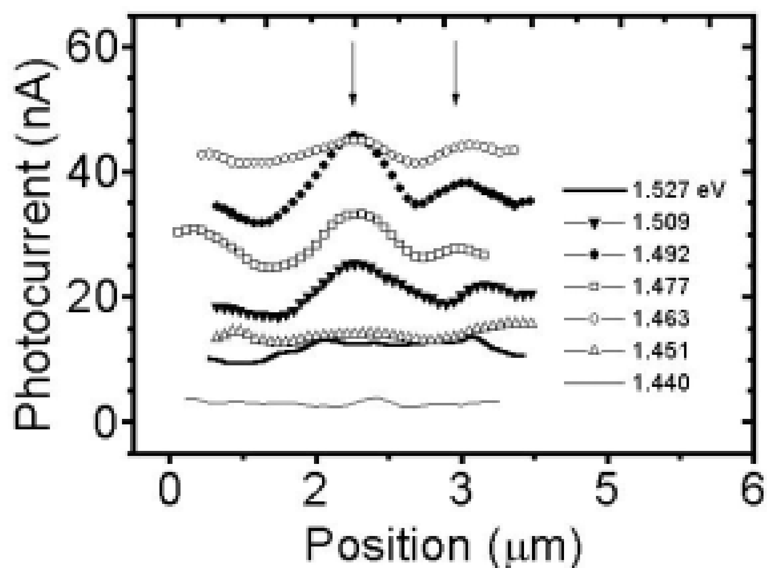

Fig. 3.2. The plot showing line traces taken from single scans across the grain outlined in Figure 3.1. The arrows indicate the location of the grain boundaries. Increased collection at the boundaries relative to the interior of the grain is observed in the scans taken at or just below the CdTe band gap. This indicates that the boundary has a lower energy gap, and therefore higher S composition, than the grain center.

Comparison with topographic data shows that the two peaks in the line traces, which are indicated by arrows in Fig. 3.2, occur at the grain boundary. The relative peak height, or contrast, is largest at 1.492 eV. The region around the boundaries collects less relative to the boundaries as the excitation energy falls below the CdTe band gap. This is presumably due to the boundary material having a lower band gap, and therefore higher S concentration, than the grain center. The contrast first becomes visible at 1.509 eV and finally disappears at 1.451 eV, allowing us to estimate that the region away from the grain boundary is nearly pure CdTe while at the boundary the S concentration is ~ 8%.

In the discussion above, we have attributed features in the photocurrent images to spatial variations in absorption which arise from changes in bandgap across polycrystalline grains due to the presence of $CdTe_xS_{1-x}$. Contrast can also originate from other sources including coupling between topography and photocurrent, and spatial variations in the collection efficiency of carriers created by the NSOM. We were able to discount the possibility that the enhanced collection was somehow due to topography affecting the coupling of light into the sample, since many such grain boundaries did not show a significant variation in photocurrent. This can be seen in Fig. 3.1 where several grain boundaries visible in the topography do not show large photocurrent contrast. Our tests also showed that the enhanced contrast at the boundaries was independent of such measurement parameters as probe-sample separation, illumination intensity, and scan speed.

The presence of spatial variations in the efficiency with which carriers are collected is a more interesting possibility to consider. For the photocurrent measurements shown in Figs. 3.1 and

3.2, small changes in excitation energy dramatically affect the spatial nonuniformities observed. This leads us to conclude that they are not due to variations in collection efficiency, as we would expect such variations to be observable over a broader range of wavelengths. In some cross sectional photocurrent images of these devices we have, however, observed enhancements in photocurrent near grain boundaries which are present not only at energies below the CdTe bandgap but also well above the bandgap, and which we believe are due to enhanced collection efficiency near the grain boundary. Probably, this effect is not due to (or not only to) the presence of the ternary phase at the GB region. In any case the effect deserves to be studied more thoroughly.

3.3 Conclusions

- Experimental results presented in this report demonstrate the effectiveness of NSOM as a high resolution method for studies and two dimensional mapping of current collection over the cell cross section.
- Variation of excitation wavelength from above to below CdTe bandgap provide new options for correlating specific topographic features of carrier photogeneration and current collection in polycrystalline thin film solar cells.
- The S concentration across annealed CdTe/CdS heterojunctions is quite nonuniform. We were able to directly observe regions at grain boundaries which have a lower band gap than that at grain centers, indicating a higher S content at the boundary. This provides very strong evidence that S diffuses preferentially along the grain boundaries of polycrystalline CdTe and suggests that the overall lack of uniformity in S composition is a result of this grain boundary assisted diffusion mechanism.
- In some cross sectional photocurrent images, enhancements were observed in photocurrent near grain boundaries which are present from energies well above the CdTe bandgap to below the gap and which we believe are due to enhanced collection efficiency near the grain boundary. This result is of a significant importance if verified by future studies. Exploration of transport effects near grain boundaries in more detail hopefully can clarify mechanisms of grain boundary effect on cell performance.

4. DEEP TRAPS IN CdTe SOLAR CELLS

The problem of detection, identification and studying the properties of deep traps in the cell is an important issue relevant both to the cell performance and to its degradation. In these section we present studies of deep traps in CdTe/CdS solar cells conducted with the deep level transient spectroscopy (DLTS) and admittance spectroscopy (AS). The DLTS studies were conducted in collaboration with Dr. R. Ahrenkiel, Dr. D. Levi (NREL) and Ahmet Balcioglu (the CSM Ph.D. student advised by Dr. Ahrienkel). His Ph.D research included comparative studies of properties of differently processed CdTe/CdS cells, namely the Cu-related deep traps in the cells fabricated at NREL (CBD CdS, CSS CdTe, and Hg:Cu/graphite back contact) and the cells prepared at CSM (CBD CdS, electrodeposited (ED) CdTe, and Cu/Au back contact). Prior to DLTS, the ED cells were characterized using C-V and C-T techniques. In Phase III of the project we started the AS studies here, at CSM, aimed at clarification of applicability of this method with respect to CdTe/CdS solar cells. Previously this method in various modifications has been successfully applied to CIS and CIGS solar cells.

4.1 DLTS Studies of Electrodeposited CdTe/CdS cells

Cell fabrication and characterization

The cells were processed with only small deviations from our standard procedure. The 250 nm thick CdS layer was deposited on commercial tin oxide/glass substrate and annealed with $CdCl_2$ in N_2 for 50 min at 450°C. After electrodepositing ~3 μm thick CdTe, the obtained structure was subjected to $CdCl_2$ treatment in air for 45 min at 410°C. After etching with 0.1% Br_2/methanol, the Cu layers of 30 or 100 Å thickness were thermally evaporated on the CdTe surface followed by annealing at temperatures ranging from 100° to 250° C for 15 min in vacuum. Afterwards, a Br_2/methanol etch was applied to remove the remaining Cu from the CdTe surface. Metallization of the back contact was provided by thermal evaporation of gold.

The results of J-V characterization for the cells prepared with different temperature of the post-Cu annealing are presented in Table 4.1

Table 4.1 Device performance vs. Cu annealing temperature

Temperature ^{o}C	**Efficiency** %	J_{sc} mA/cm^2	V_{oc} mV	Rs Ω-cm^2	R_{sh} Ω-cm^2	FF %
100	7.00	21.5	670	40.0	230	49
140*	9.00	20.9	732	2.60	475	59
150	10.6	22.8	725	7.00	560	64
170*	8.10	20.4	728	7.70	409	54
200	8.50	22.1	658	9.10	316	59
250	5.30	19.3	564	12.8	190	48

The highest efficiency was demonstrated by the cell with 150°C post-Cu annealing temperature. Efficiency decreases as the annealing temperature goes up or down from 150°C. As to the

particular cell parameters (V_{oc}, J_{sc}, etc.), the "150" cell has the highest J_{sc}, R_{sh} and FF values. V_{oc} is only a little lower than that for the neighboring cells, "140*" and "170*" that were processed with 100 Å thick Cu films. These two cells demonstrate considerably lower J_{sc}.

Standard C-V measurements to determine the apparent doping profile were performed at a frequency f=100 kHz using the standard treatment of the data based on the equation [50]:

$$N = \left[\frac{A^2 q \varepsilon \varepsilon_0}{2} \frac{d\left(1/C^2\right)}{dV} \right]^{-1} \tag{4.1}$$

where C is the measured capacitance, V is the applied bias voltage, A is the area of a cell. The carrier concentration profiles determined for the cells listed in Table 4.1 are shown at Fig. 4.1. It is to be noted that the "doping level" increases with the annealing temperature and that this level rises at smaller depths, that is closer to the CdS/CdTe interface.

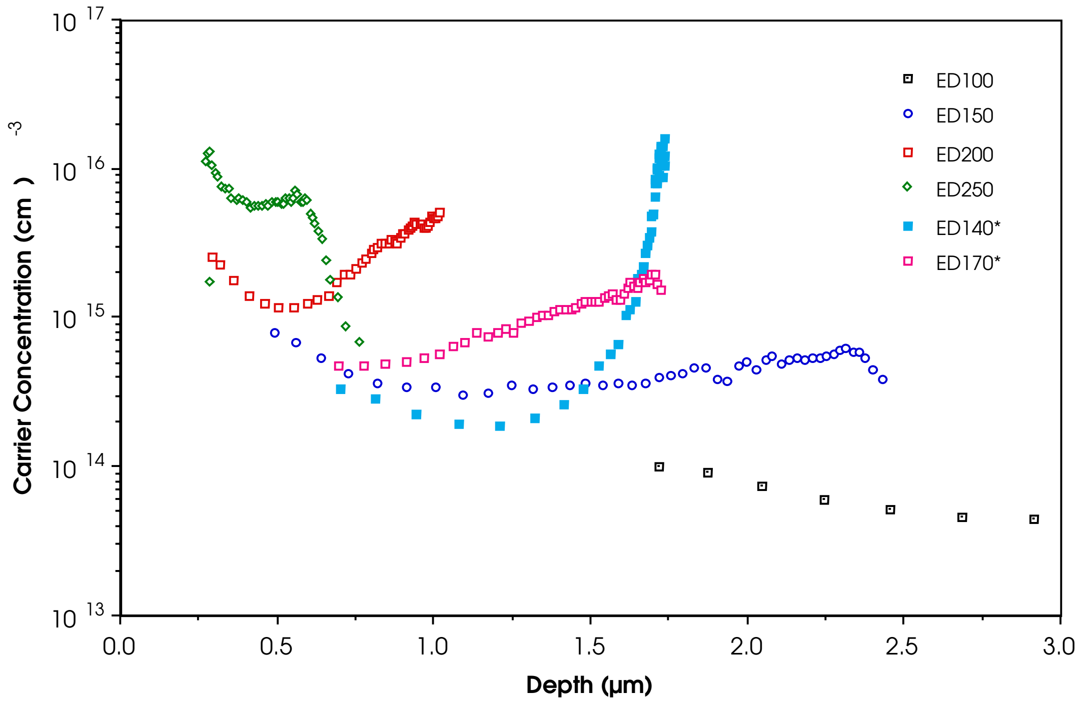

Fig. 4.1 The carrier concentration profile measured at room temperature for various post- Cu annealing temperatures

For the "150" cell the "doping density" at zero and reverse biases is close to that for the NREL CSS cells, but at the forward biases exceeds those by more than an order of magnitude. The discrepancy for the "200" and "250" cells is remarkably higher.

Fig. 4.2 shows the temperature dependence of carrier concentration derived from the C-V measurements for the cell "150". A remarkable decrease is seen as temperature changes from

400 K to 150 K. It should be also mentioned that the capacitance dependence on bias weakens with decreasing temperature. For measurements at 150 K the C value changes only by about 5% in the bias range from –1.8V to +0.2V. At T =100 K no change in capacitance could be seen in the same bias range and the depletion width estimated from the capacitance is very close to the CdTe layer thickness. One of the probable explanations for this C(T) behavior is carrier freeze-out. If true, the impurity level that provides the dominating contribution to the hole concentration likely is not shallow, or that it is strongly compensated.

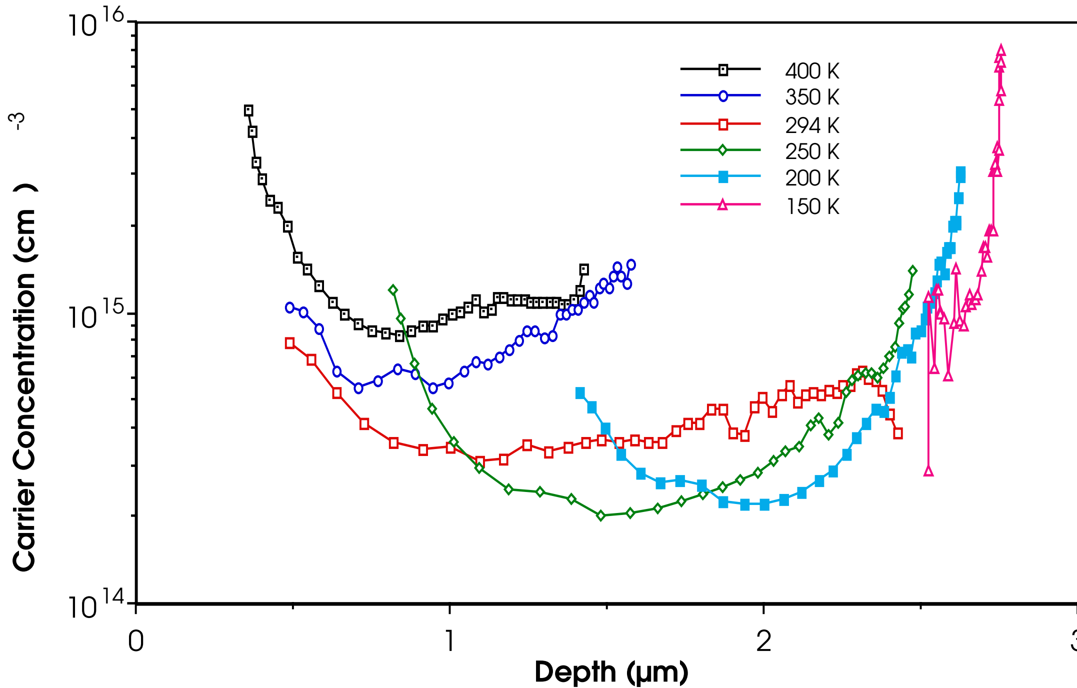

Fig. 4.2 The carrier concentration-depth profile in the cell "150" as a function of temperature

Another possible mechanism of the temperature-dependent capacitance is the influence of deep traps. It is known that in the presence of deep traps two distinct components of the measured capacitance should be considered [50]. The first one is described as the geometry or depletion capacitance, C_d, which is determined by the depletion width and does not depend on the testing voltage frequency, ω (the angular frequency ω [rad/s]=$2\pi f$ [Hz]). The second component is due to oscillations of the electrical charge trapped by deep levels, named the oscillation capacitance, C_T. The amplitude of these oscillations and hence the magnitude of C_T depends strongly on the relationship between ω and the characteristic frequency of traps, ω_o, which is reciprocal of the characteristic time, τ. For high testing frequencies, $\omega >> \omega_o$, the trapped charge cannot follow changes of the testing voltage and the C_T value tends to zero. As frequency ω decreases, becoming of the order of ω_o or lower, the C_T value increases and tends to saturation at the level that depends on the trap concentration. Thus the reduction of the measured capacitance with the testing frequency could be considered as an indication of the deep traps presence. (More detailed analysis of the oscillation capacitance is presented in Sec. 4.2).

C-V measurements were performed on the cell "150" at room temperature at testing frequencies of 0.1, 1, 10, and 100 kHz. The frequency-dependent capacitance was observed over all the bias range from –2 V to +0.5 V. Reduction of capacitance with frequency was much more pronounced at zero and forward biases than at the reverse bias. Indeed, for $V_{bias} = 0$ and $V_{bias} = +0.5$ V the measured capacitance decreases 2.5 times as frequency rises from 0.1 kHz to 100 kHz, while at $V_{bias} = -2$ V the decrease is only of about 25 %. These data show that there exist deep traps in amount comparable to the carrier concentration or even higher, and that the traps are probably distributed non-uniformly over the CdTe thickness.

One more conclusion can be made from these measurements, namely from a rather smooth C(f) dependence. Indeed, the C(f)/C(0.1 kHz) ratio measured at $V_{bias} = 0$, is equal to 0.7, 0.5 and 0.4 for f=1 kHz, 10 kHz and 100 kHz, respectively. For a single trap level with a certain characteristic frequency ω_o, the $C_T(\omega)$ dependence is described by the equation:

$$C_T(\omega) = C_T(0)\frac{1}{1+(\omega/\omega_o)^2} \tag{4.2}$$

A significant change in C_T with ω takes place close to ω_o. In the range of ω=(1/5-5)ω_o, $C_T(\omega)$ changes from 0.96$C_T(0)$ to 0.04$C_T(0)$. At lower and higher frequencies the measured capacitance approaches rapidly the saturation levels, $C_0=C_T(0)+C_d$ and $C_\infty=C_d$, respectively. In our measurements the C value changed gradually as the testing frequency ω increased by three orders of magnitude. That means that there are several trap levels in the band gap or, possibly, bands of trap levels.

Based on the deep trap concept, we can discuss an alternative explanation for the temperature dependence of capacitance. The characteristic time/frequency of a trap depends on emission rate and varies exponentially with temperature: $\omega_o \propto \exp(-\Delta E/k_BT)$, where ΔE is the distance between the trap level E_T and the edge of the corresponding band, that is $\Delta E=E_T-E_V$ if we consider traps for holes. Thus the traps that are "too slow" at room temperature to follow the oscillating voltage, become "players" when their ω_o approaches ω due to enhanced temperature. It is seen from Eq. 4.2 that contribution of traps to the capacitance measured at some frequency ω, $C_T(\omega)$, increases with rising ω_o, approaching the limiting value $C_T(0)$. The $C_T(0)$ value is determined by the trap concentration, its distribution over the diode thickness, and band bending [50].

While the second mechanism (deep trap contribution) is supported by the data presented above, the first one (increase in carrier concentration with temperature) is also rather probable. It is to be noted that the data presented at Fig. 4.2 were obtained at a high frequency of 1 MHz, hence the contribution of deep traps to the total measured capacitance, that is the ratio $C_T/(C_T+C_d)$, was minimized as much as possible. To clarify the role and estimate the individual contributions of these two mechanisms we need to perform more thorough experimental studies and modeling.

DLTS studies

All the DLTS studies as well as the minority-carrier lifetime and SIMS measurements were performed at NREL. The DLTS measurements were used to determine the energy of deep levels in the bandgap and estimate the trap concentration. These measurements were done at a reverse bias of –1.0 V with pulse amplitude of 1V and pulse width of 1.0 ms. The concentration of trap levels was estimated using equation [50]:

$$N_T = 2\frac{\Delta C}{C}N\left(\frac{w^2}{(w-\lambda)^2-(w_o-\lambda)^2}\right) \quad (4.3)$$

where ΔC, C, $N=(N_A-N_D)$, w, w_o and λ are the DLTS peak maximum, steady state capacitance of a peak maximum, the carrier concentration, the depletion width at reverse bias, depletion width at forward bias, and the edge region. The latter is defined as a distance from the depletion region edge and to the plane where the trap level crosses the Fermi level ("crossing point").

Five deep levels were observed in devices studied in the temperature range of 80 to 450 K. They were designated as E1 (the electron trap), H1, H2, H3, and H4 (all four are hole traps). Their energies are presented in Table 4.2. It was found that the deep levels were partially annealed as a result of the DLTS scan from 80 to 450 K. The repeated scan revealed reduction of the trap concentration and a significant change in the peak shape. The trap concentrations calculated using the initial DLTS spectra (the first scan 80-450K) are also shown in Table 4.2. The trap levels H1, H2, and H3 were derived from the DLTS spectra obtained on the partially annealed samples because at the initial scan the DLTS peaks did not shift with the emission rate window. It might be due to the presence of the interfacial layers, non-exponential transients, and large series resistance of a cell.

The estimated concentration of traps is pretty high being comparable to the "doping level" derived from C-V measurements (the free carrier concentration), especially for the deepest H2, H3, and H4 levels. The observed increase in the trap concentration with increasing post-Cu annealing temperature correlates with the increase of Cu concentration in the CdTe indicated by SIMS measurements performed at NREL by Drs. S. Asher and R. Reedy, see Fig. 4.3.

Table 4.2. Trap levels and concentrations

	Trap level energy				
	E1 E_c-0.37 eV	H1 E_v+0.34 eV	H2 E_v+0.70 eV	H3 E_v+0.80 eV	H4 E_v+0.97 eV
Sample ID (Cu anneal Temperature)	Trap concentration (cm^{-3})				
"100"	$9.7x10^{11}$	-	$5.6x10^{13}$	$7.7x10^{13}$	-
"150"	$3.2x10^{13}$	-	$1.5x10^{14}$	$1.8x10^{14}$	-
"200"	-	$3.5x10^{12}$	$3.0x10^{14}$	$3.9x10^{14}$	$6.5x10^{14}$
"250"	-	$2.5x10^{13}$	-	$5.2x10^{14}$	$1.2x10^{15}$

Five deep levels: $E1^*=E_c-0.28eV$, $H1^*=E_V+0.35eV$, $H2^*=E_V+0.45eV$, $H3^*=E_V+0.79eV$, and $H4^*=E_V+0.93eV$, were also revealed in the NREL CSS devices [51, 52]. These energies are close to those found in the CSM cells except the H2* and H2 levels. Probably the other four levels are associated with the same types of defects in both materials. Small difference in energy for similar states observed in the two materials should not be considered as evidence of a different nature of the defects. Indeed, it could be seen from literature that the estimates in various reports of the levels attributed to the same centers vary depending on the method of the CdTe cell preparation and the CdTe postdeposition treatment. Abou-Elfotouh *et. al*. [53] observed in the ED-grown CdTe devices a minority carrier trap level with an activation energy of $E_c-0.35eV$. In as-grown CSS CdTe/CdS cells the E1 level has an activation energy of $E_c-0.28$ eV [51, 52]. After stressing of a cell this level shifts into the band gap by 0.22eV [51]. The H1 level of energy about Ev+0.35 eV was previously reported for the ED-grown, CSS- grown CdTe devices [53-56] and p-CdTe single crystals [15, 54, 57]. Usually it is attributed to Cu_{Cd} substitution defects. The H3 level with the energy around $E_v+0.8eV$ was reported in numerous publications and is believed to be associated with an acceptor complex involving the native V_{Cd} defect and impurity.

The concentration of levels E1 and H1 are comparable for both the NREL and CSM devices. The concentration of H2 traps was two orders of magnitude higher in the CSM devices. Concentrations of H3 and H4 traps were also significantly higher for the CSM cells.

It is to be noted that for the trap H3 with an activation energy close to the CdTe midgap, the thermal emission rates were found comparable for electrons and holes [58]. This indicates that these traps can act as effective recombination centers. To confirm this, the minority-carrier lifetime was measured in the CSM cells using time-resolved photoluminescence (TRPL). The lifetime was found to depend on the post-Cu annealing temperature and hence the trap concentration. The data presented in Table 4.3 show the tendency of the lifetime to reduce with increasing trap density. The latter increases with the annealing temperature and, as seen from Fig. 4.3, with the Cu content in CdTe. The minority-carrier lifetime was also measured in the standard NREL CSS devices and was found to be of the order of 0.6-1.0 ns.

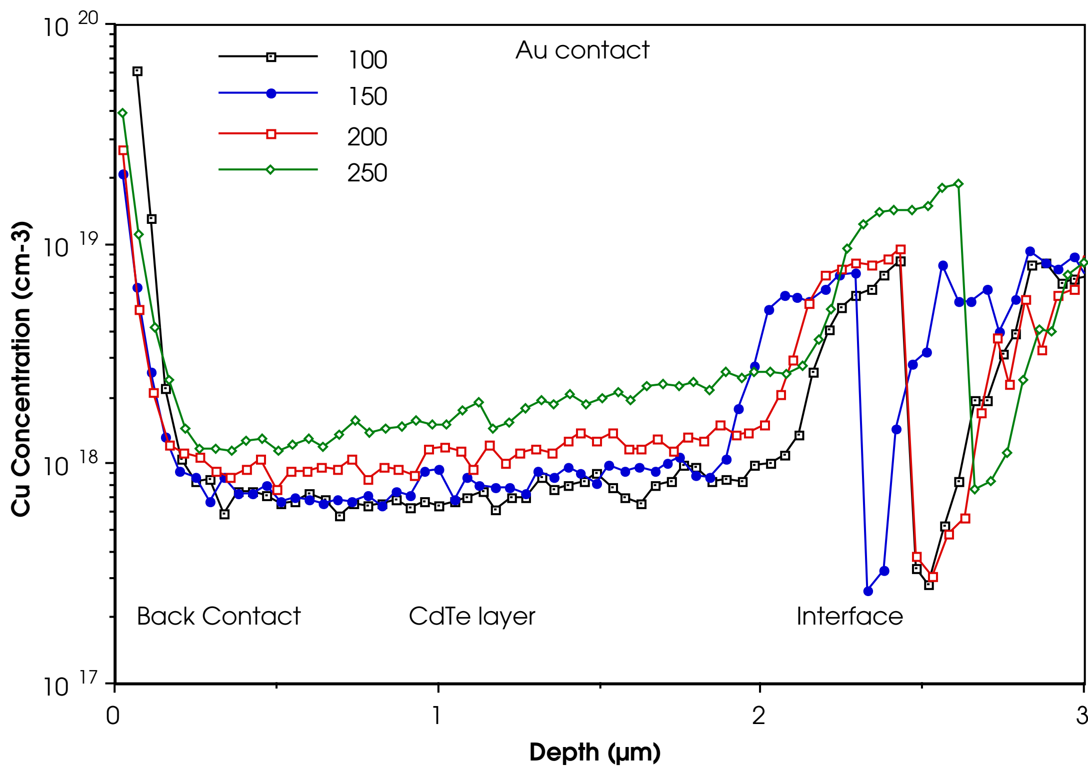

Fig. 4.3 SIMS data on the Cu concentration profile in the CdTe/CdS solar cells with the Cu/Au back contact annealed at different temperatures: 100, 150, 200 and 250° C.

Table 4.3 Lifetime determined using the TRPL in dependence on the post-Cu annealing temperature

Ann. Temp. (^{o}C)	140	150	170	200	250
Trap conc. ($10^{14}cm^{-3}$)	-	1.8	-	3.9	5.2
Lifetime (ns)	~1.4	~1.3	~1.1	~0.4	~0.2

Discussion

The data presented in Sec.4.1 provide evidence of a few deep levels in the CdTe solar cells doped with Cu. Based on the DLTS studies and especially on the C(f, T) measurements, one can conclude that the concentration of deep electron/hole states is comparable to or even higher than the majority carrier concentration derived from the C-V profiles. Concentration of deep traps depends on the processing technology. In particular, it is different for the NREL CSS cells and

the CSM ED cells. For the latter with the Cu/Au back contact the deep trap density increases with the post-Cu annealing temperature, which in turn influences the Cu content in the CdTe detected by SIMS.

There is a significant uncertainty in identity of the defects responsible for the observed deep levels. We could speculate about the nature of a particular center/level based on the literature review, but even these guesses could not be verified unambiguously. The problem of identification is especially complicated for the fine-grain polycrystalline materials. Not all the deep levels reported for the thin film CdTe solar cells have analogs in single crystals. On the other hand, there is evidence of the deep grain boundary states that provide potential barriers for the majority carriers. These states were found in both bicrystals and polycrystalline films, see, e.g., [2, 3, 8]. Probably these GB states are related to the specific GB defects such as dangling bonds. However, enhanced concentration of impurities, native defects and complexes in the GB region may provide energy levels different from those in the bulk material because of a different environment in the highly disordered GB region.

It is doubtful that the problem of the deep level identity can be solved soon. However, revealing deep traps and their thorough studies on the empirical level are important and urgent issues in the activities aimed at improvement of cell performance and stability. One must establish and explain (using modeling) correlations between the determined trap characteristics, on one hand, and the cell photo-electrical parameters, such as V_{oc}, J_{sc}, R_{se} etc., on the other. It is also necessary to analyze the deep trap influence on the C-V profile and correct the "doping level" derived. Finally, the trap characteristics and the cell performance should be related to the cell processing techniques and regimes to provide the basis for optimizing the latter.

4.2 Admittance Spectroscopy of Deep Traps in CdTe/CdS Solar Cells

<u>Basics of the method</u> (see, e.g., [50])

If the band bending V is sufficiently large so that the Fermi level E_F crosses the trap level E_t at some distance from the interface, x_t (crossing point), then the electric charge accumulated by traps oscillates under the oscillating voltage applied. If the amplitude of the oscillating voltage is much lower than the total band bending, then the charge oscillations occur in a narrow space region around the crossing point. Oscillating current due to the trap recharging has both in-phase and out-of-phase components so that the total measured impedance can be presented in the form:

$$Y = Y_d + Y_t = [G_d(\omega) + G_t(\omega)] + i\omega[C_d(\omega) + C_t(\omega)] \quad (4.4)$$

where ω is the angular frequency of the oscillating (testing) voltage, G_d and C_d represent the diode conductance and capacitance in the absence of traps while G_t and C_t are the additional conductance and capacitance provided by the trap charge oscillations. In the case of a single trap level with a characteristic frequency ω_t the frequency dependencies of C and G are described by equations:

$$C(\omega) = C_d + \frac{C_t^o}{1 + (\omega / \omega_t)^2} \tag{4.5}$$

$$G(\omega) = G_d + \frac{G_t^o (\omega / \omega_t)^2}{1 + (\omega / \omega_t)^2} \tag{4.6}$$

$$\frac{C_t^o}{C_d} = \frac{N_t}{N} \left\{ \frac{1 - (x_t / x_d)}{1 + (x_t / x_d)(N_t / N)} \right\} \tag{4.7}$$

$$G_t^o = C_t^o \omega_t \tag{4.8}$$

In these equations x_d is the total depletion width, which determines the "geometry" diode capacitance $C = A\varepsilon\varepsilon_o / x_d$ (A is the diode area); $N = N_a - N_d = n_h$ is the difference between the concentrations of shallow acceptors and compensating donors, which defines the hole concentration n_h beyond the band bending region; N_t is the trap density. We do not discuss here the influence of the N and N_t spatial non-uniformities.

Comparison of the conductance and capacitance values measured at high and low frequencies ($\omega_{HF} >> \omega_t$ and $\omega_{LF} << \omega_t$) provide estimates of C_d, G_d, C_t^o and G_t^o:

$$C_d = C(\omega_{HF}); \; G_d = G(\omega_{LF});$$
$$C_t^o = C(\omega_{LF}) - C(\omega_{HF}); \; G_t^o = G(\omega_{HF}) - G(\omega_{LF}) \tag{4.9}$$

Analysis of the frequency dependencies of the derivatives, $dG/d\omega$ and $-dC/d\omega$, provides additional and useful options to determine the trap characteristics. Both derivatives should demonstrate peaks at the same frequency $\omega_p = \omega_t / \sqrt{3}$ and the magnitudes of these peaks are:

$$\left.\frac{dC}{d\omega}\right|_{\omega_p} = -\frac{3\sqrt{3}}{8} \frac{C_t^o}{\omega_t}; \; \left.\frac{dG}{d\omega}\right|_{\omega_p} = \frac{3\sqrt{3}}{8} \frac{G_t^o}{\omega_t} \tag{4.10}$$

Experimental results and discussion

Admittance of the cells was measured using two LCR meters in the angular frequency range of $\omega \cong 126$ to 1.8×10^8 s^{-1}. The oscillating voltage amplitude was 0.01 V. Measurements were performed at different biases and temperatures of 0, 23 and 100°C. In addition to admittance spectroscopy the transient effects in conductance and capacitance were measured caused by switching the bias voltage applied. The as-prepared cells were studied as well as the same cells after stressing at 100°C in dark under bias applied for 280 hours.

Fig. 4.4 shows typical frequency dependencies of capacitance and conductance measured at room temperature. These dependencies are in general consistent with the predictions of theory. The capacitance reduces more than three times with frequency increase while conductance increases by more than five orders of magnitude. We should be cautious when analyzing data at very high frequencies, since the presence of a finite series resistance can lead to a decrease in capacitance and increase in conductance in this range. However, even in the frequency range of 20Hz to 100kHz capacitance reduces by two times, which means that $C_t^0 / C_d \geq 2$.

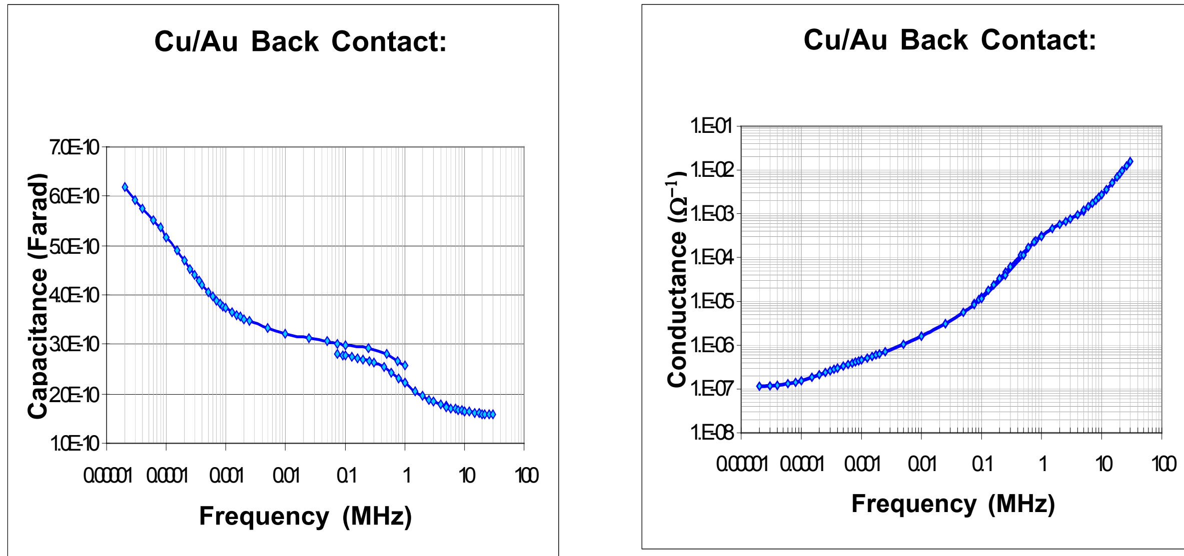

Fig. 4.4 Capacitance and conductance of a cell with the Cu/Au back contact measured at room temperature

The expression in the curly braces in Eq. 4.7 is always smaller than 1, hence $N_t / N > C_t^o / C_d$. The two-fold decrease of capacitance in this frequency range means that concentration of traps with characteristic frequencies $\omega_t \leq 6 \times 10^5 s^{-1}$ exceeds the "doping level". The absence of saturation of the $C(\omega)$ dependence in the low frequency range must be attributed to the presence of slow traps with $\tau > 10ms$, which could not be detected by our LCR meter.

It is seen from Eq. 4.5 that the trap level effect becomes considerable only when the test frequency ω increases to near the characteristic frequency ω_t, and then reduces rapidly with further increase of ω. However the measured C value gradually decreases while the frequency changes several orders of magnitude. One can explain this by suggesting several types of traps with different characteristic frequencies or broadening of the trap level. Characteristic frequency depends exponentially on the distance between the trap level and the valence band edge, thus ω_t can vary significantly within the trap band. In particular, one may attribute the trap band to the grain boundaries that are known to provide deep states in a wide energy range.

The (dG/df)-f plot in Fig. 4.5 demonstrates two, and perhaps three, peaks that could be attributed to single levels or relatively narrow trap bands. These peaks are much more pronounced than in the (dC/df)-f plot. The characteristic times derived from the peak frequencies are 4 ms, 1.6 ms and 0.35 μs. The particular trap concentrations estimated from the peak magnitudes are comparable to the "doping level" for all three peaks.

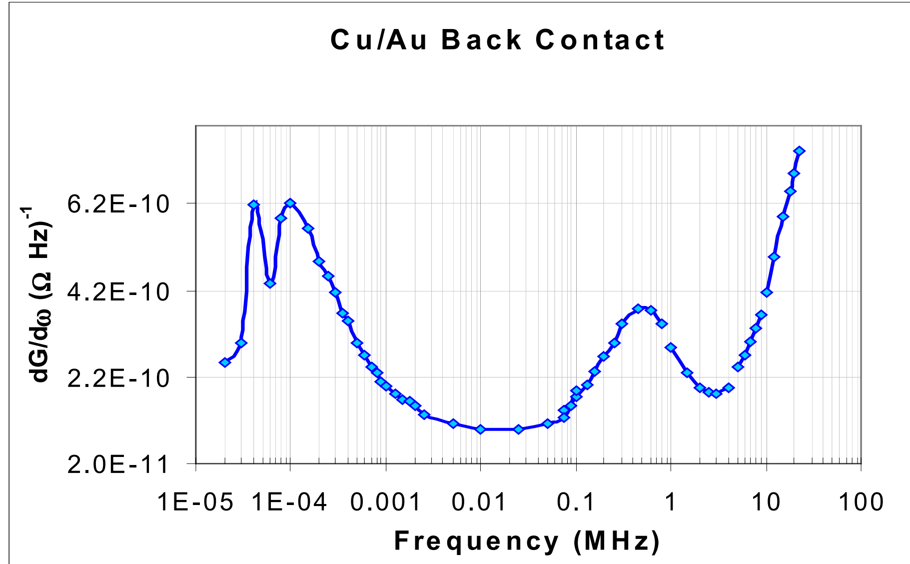

Fig. 4.5 The $(dG/df)-f$ plot demonstrates two or maybe three peaks related to different trap states with characteristic times of 4 ms, 1.6 ms and 0.35 μs

An increase in temperature provides the shift of the peak position toward high frequency. From analyzing this shift for the high frequency peak in Fig. 4.5 in the temperature range from 0 to 100 ^{0}C we estimated the activation energy as $\Delta E = (0.37 \pm 0.03)\,eV$. This value should be close to the difference $E_t - E_v$ although not exactly equal to it if the capture cross section depends on temperature. The trap level position estimated in this way does not differ much from one of the levels detected by DLTS and from the level $E_v + 0.35eV$ reported in literature and usually ascribed to the Cu ions in the Cd sites. An estimated value of the capture cross section is between 10^{-14} and 10^{-15} cm^2.

The influence of the bias voltage applied to the cell on the same peak was as follows: the peak position does not change significantly, which indicates no considerable change in ω_t, hence in emission rate; the peak amplitude increases about 10 times when the bias changes from –0.5 V to +0.5 V. This increase should be attributed to the decreasing ratio x_t / x_d with the reduction in band bending. Eq. 4.7 shows that effect of the trap charge oscillations increases as x_t / x_d goes

down and the C_t^o / C_d ratio comes closer to N_t / N. The latter parameter estimated from the peak amplitude for $V_{bias} = +0.5V$ exceeds 2.

Transients in capacitance and conductance were measured with switching applied bias 0 V → –1 V→ 0 V while holding at –1V for about two minutes. The testing voltage frequency was 1MHz. The C value measured about 3 seconds after switching back to $V_{bias} = 0$ was about 20 % higher than it was before applying reverse bias. Even after 5 or more minutes it did not return to the initial value. It is unclear whether the observed long-term relaxation is totally due to the recharging of slow electronic states or there is some contribution of migration and spatial redistribution of highly mobile ions such as Cu_i^+. If the difference in the C values before and immediately after exposure to the reverse bias is due only to the slow traps ($\tau \geq 3\,\mathrm{sec.}$), then the estimated concentration of these traps should not be less than 2N.

Comparison of the results of admittance spectroscopy for Cu/Au and Au-contacted cells demonstrates significant effects induced by the Cu dopant. The differences are especially visible in the $(dG/d\omega) - f$ plots. In particular, the high frequency peak ($\Delta E = (0.37 \pm 0.03)\ eV$) that is well pronounced in Cu-doped cells disappears in the undoped cells. Instead a small peak at 100 kHz is seen. The decrease in magnitude and some shift in peak position was observed for the low-frequency peak (~ 100 Hz). Significant differences are noted in the transient effects. Changes for stressed cells are also more significant for cells doped with Cu.

4.3 Conclusions

- The results of AS studies are in many respects similar to those obtained with DLTS. In particular, it was found that in the Cu-doped cells the trap concentration is rather high, exceeding the "doping level".
- There exist slow trap bands of high density that might be attributed to the grain boundary states. Single level traps or narrow trap bands with concentrations comparable to the doping level were detected at higher frequencies.
- The trap concentration and properties manifest considerable differences for undoped cells and those doped with Cu as well as for the as-prepared and stressed cells. That provides some new opportunities for clarification of mechanisms of Cu influence on the cell performance as well as on the degradation processes.

We are in the very beginning of the admittance spectroscopy studies of traps in CdTe/CdS cells but even the first results have shown that AS is a suitable method for detecting and studying properties of traps. Measurements in the bias, temperature and light intensity ranges provide numeral options for studying the trap level energy, its broadening, capture cross section, concentration of traps and its spatial distribution. This method seems to have even some advantages as compared to DLTS. The technique of measurement is simpler providing an opportunity of routine characterization of numerous cells differently processed and stressed. It could be applied to the cells with high trap concentration, comparable or even exceeding the "doping level". However, it should not be considered as a replacement of DLTS. Combined DLTS and AS measurements can complement each other, providing checking and verification of information obtained by each of them.

5. STUDY OF CELL DEGRADATION UNDER STRESS CONDITIONS

This section presents our studies of the degradation of the CdTe/CdS solar cells under various stress conditions. The cells under investigation included those with vapor transport deposited (VTD) CdTe (First Solar, LLC) and with electrodeposited (ED) CdTe (CSM). Various back contacts to both types of material were applied at CSM. One of the major goals was to find and analyze manifestations of electromigration of the electrically charged defects and impurities that are responsible for the degradation of a cell. To make this possible we conducted the stress tests in dark and light under different external biases. One must keep in mind that even at the absence of an external bias, strong built-in electric field exist in a cell that may cause electromigration of defects and influence its rate. The built-in potentials and the electric fields are different in dark and light. It is clear also that external biases applied to the cell change the magnitude and distribution of the electric fields over the cell thickness, hence providing changes in electromigration processes.

If we do not consider the electric fields in the GB regions due to the GB electrical charge, there are two regions in the cell with high electric fields (one-dimension model). The first one is the depletion layer adjacent to the CdTe/CdS junction. Under the open circuit condition ($V_{bias}=0$) in dark, the width of this layer is about 1.5 μm and the average electric field is of the order of 10^4 V/cm. Illumination of a cell with 1 Sun intensity decreases the built-in potential by an amount of about 0.8 V. The depletion layer shrinks considerably and the electric field diminishes significantly. The second region is the CdTe layer adjacent to the back contact interface. There are many indications that a Schottky diode usually exists at this interface with a potential barrier for the majority carriers (holes in our case). In the as-prepared cell this barrier is low and thin enough to provide tunneling through the barrier and sufficiently low "series resistance". But aging of a cell, especially under stress conditions, leads to the development of a stronger barrier, which manifests itself in an increase of “series resistance”.

The major objectives of the studies were:

- Studying degradation of the differently processed cells with different back contact structures cells under widely varied stress conditions to clarify what conditions provide the most severe degradation of a particular cell parameter and how the degradation rate depends on processing procedure.
- Studying reversible effects under consecutively changed applied biases
- Searching for manifestations of electromigration

5.1 Stressing Cells with the Vapor Transport Deposited CdTe and Cu/ZnTe/Au Contact.

Samples. Stress conditions

Cells were fabricated using the Glass/TCO/CdS/CdTe structures supplied by First Solar, LLC. The back contact was applied in our facilities. A multilayer structure consisting of the Cu, ZnTe, and Au layers was deposited on the preliminary etched, rinsed and dried CdTe surface. The successive deposition of the Cu and ZnTe layers instead of coevaporation previously used provided more precise control of the Cu amount. No considerable difference in the initial

performance of a cell was found for these two methods of the back contact preparation. No difference was found in the degradation rate for the same stress conditions such as enhanced temperature, vacuum, dark, open circuit.

All the stress tests were conducted on un-encapsulated cells in air. To activate the degradation processes, stress conditions included an elevated temperature of 100^0C. When stressing in light, about 1 Sun intensity was used. In the course of degradation the J-V (light and dark) and C-V (dark) dependencies were periodically measured.

Results of stressing

Some results of stress testing are presented in Table 5.1. The table shows that stressing under different applied biases leads to significantly different changes in the cell parameters. It is also seen that the results of stressing under the given bias conditions can differ considerably for stressing in dark and light.

Table 5.1. Changes in the cell parameters as a function of stress test conditions and length (time). Data are averaged over a number of cells stressed under the same conditions. Designations for the stress conditions: D – dark; L – light; RB – reverse bias, V≈-1V; SC - short circuit (V=0); V_{mp} - bias corresponds to the maximum power; OC - open circuit (J=0), FB – forward bias, J= +5 mA/cm^2.

Stress time, h	D, RB	D, OC	L, RB	L, SC	L, V_{mp}	L, OC	L, FB
				Δ Eff., %			
24	-50	-24	-22	-6.5	-9	-21	-20
113	-60	-44	-24	-21	-13	-6.7	-19
				Δ Voc, %			
24	-12	-2.3	-6.4	-4.3	+0.9	-0.5	-4.8
113	-8.7	-4.6	-7.0	-5.5	-1.4	-0.8	-7.0
				Δ Jsc, %			
24	-15.5	0.0	+1.1	+2.2	-3.0	+1.6	+2.9
113	-13.5	-4.3	-0.9	-9.9	-4.7	+1.1	+7.7
				ΔRse, %			
24	+2500	+440	+145	+22	+40	+230	+140
113	+2500	+820	+250	+75	+35	+80	+120
				Δ Rsh, %			
24	-70	-48	-21	+43	+20	-26	-18
113	-70	-65	-10	+45	+23	+2.8	-30.3

The highest degree of degradation of all parameters was observed for the (D, RB) stressing. The "series resistance" defined as $R_{se}=(dV/dJ)_{V=Voc}$ for the J-V dependence measured in light, increased more than 25 times. Lower, but also significant, increase in R_{se} took place at (OC) stressing. In

light R_{se} degrades much less, especially at (L, SC) and maximum power (L, $V_{mp)}$ conditions. The "Shunt resistance" $R_{sh}=(dV/dJ)_{V=0}$ measured in light also degrades strongly in the dark and much less in light. Moreover, for {L, SC) and (L,V_{mp}} conditions R_{sh} increases after stressing. V_{oc} degrades considerably at reverse bias both in dark in light, but in dark the change is greater. The lowest degradation of V_{oc} takes place at (L, SC) and (L,V_{mp}) conditions. Contrary to V_{oc}, the short circuit current, J_{sc}, even increases at {L, OC) and (L, FB), while it degrades significantly at (L, SC) and (L, V_{mp}) (see data for the 113 hour stressing). Again, the most severe degradation is seen for (D, RB) condition.

For all stress conditions, especially for (D, RB), an increase in series resistance contributes much more to the total efficiency degradation than all other parameters. A strong correlation was found between the R_{se} increase and lowering of the doping level in CdTe layer detected by C-V measurements. It is assumed that high doping level in the CdTe region adjacent to the back contact provides lowering and thinning the Schottky barrier, hence tunneling of holes through the barrier and low resistance of the back contact. This is one of the reasons why the acceptor Cu dopant is usually introduced via the back contact application. Conversely, a decrease in doping level should lead to development of stronger Schottky barrier and increase in series resistance. To stress and clarify specific features of J-V characteristics caused by the back contact Schottky diode we have studied the dynamic resistance R=dV/dJ in the forward bias range where the series resistance influence is well pronounced. The minimum and maximum in R(V) and R(J) dependencies are the major features we were focused on.

Our analysis of R(V) and R(J) dependencies for the two diode model is described in [59, 60]. These two diodes are: CdTe/CdS p-n heterojunction (the main diode, MD) and the back contact Schottky diode, SD. They are connected in series, opposite to each other. The major features in J-V characteristics we are focused on are the minimum and maximum present in the R(V) and J(V) dependencies. The MD resistance reduces exponentially with the forward current density through the cell. The same current is reverse for the SD, hence the resistance of the latter increases as the J magnitude increases. If the SD saturation current is sufficiently low (as in the case of degraded cells), then at some forward (with respect to the MD) J value, $R_{SD}=R_{MD}$. As J increases further, R_{SD} exceeds R_{MD}, and the total resistance of a cell increases. Thus R should have a minimum at some forward bias voltage/current value. Modeling of J-V characteristics for the SD shows that at sufficiently high reverse bias its resistance may drop with the applied voltage due to the image-force lowering and narrowing of the Schottky barrier. That can explain a maximum in R(V) and R(J) curves. The maximum sharpness and position on the V and J scales depend on the dominating mechanism of carrier transport through the diode.

Both minimum and maximum are due to the presence of SD and become invisible for very good, low-resistance back contacts. For the cells with the most degraded "series resistance" (the cells stressed in dark at reverse bias), where the dynamic resistance is very high over the whole range of bias applied, minimum and maximum are also practically non-detectable. We limit our discussion here to the cells with the moderate degradation of R_{se} and to the J-V data measured in dark where both minimum and maximum in dynamic resistance are more pronounced than in the the "light" J-V characteristics.

The R maximum is less sharp and shifts to higher bias voltage as degradation of series resistance becomes more severe. This indicates transition from predominantly tunneling mechanism to the thermionic-emission/ drift-diffusion mechanism. As to the minimum resistance, R_{min}, its value increases with stressing, and its position on the J scale, J_{min}, shifts toward lower J. To extract some cell characteristics from the data on R_{min}, we used the equations [60]:

$$J_{\min} = J_{SD0}\left[1+\left(\frac{A_{SD0}}{A_{MD0}}\right)^{1/2}\right]^{-1} \tag{5.1}$$

$$V_{\min} \approx \frac{k_B T}{e} A_{MD0} \ln\frac{J_{SD0}}{J_{MD0}} \tag{5.2}$$

$$R_{\min}\times J_{\min} = \frac{k_B T}{e} A_{SD0}\left[1+\left(\frac{A_{SD0}}{A_{MD0}}\right)^{1/2}\right] \tag{5.3}$$

where $V_{\min}$ is the location of $R_{\min}$ on the bias scale; J_{MD0}, J_{SD0} are the saturation current densities for the main diode and Schottky diode, respectively; and A_{MD0}, A_{SD0} are the quality factors for these diode.

For the differently degraded cells under discussion the J_{min} and R_{min} values varied by more than order of magnitude while the product $R_{min}\times J_{min}$ varied not more than 5% and was almost the same as for the as-prepared cell. From these results one may conclude that (1) the simple two-diode model describes well the properties of the studied cells and (2) degradation did not lead to a significant change in the diode quality factors. More detailed analysis showed that A_{MD0} was confined to the range of 1.7 to 1.85. The A_{SD} value slightly increased with stressing from ~1.3 to 1.6. The major differences were found in the back contact Schottky diode saturation current. In the cell with the highest R_{se} it was almost 20 times lower than for the as-prepared cell.

In order to achieve better understanding of the role of electromigration, we conducted some stress tests consecutively applying different biases to the same cells. Stress testing was conducted in dark at the temperature of 100^0C. Cells were characterized before stressing, after stress test under bias for 20 h, and then after additional stressing for 20 h under another bias. Some results of these studies are presented in Table 5.2.

Table 5.2 Stress tests under varied bias

Stress conditions	Eff.,%	J_{sc}, mA/cm^2	V_{oc}, mV	R_{se}, Ω-cm^2	R_{sh}, Ω-cm^2
Before Stress	11.5	21	825	2.7	560
OC, 20 h	8.7	20	770	16.7	305
OC, +20 h	7.7	18.8	760	20.8	290
Before stress	11.4	20.5	805	2.7	725
FB, 20 h	11.4	20.0	825	2.0	730
FB, +20 h	10.2	19.5	810	2.7	600
Before stress	11.3	20.8	805	3.5	695
RB, 20 h	7.7	20.2	745	86	680
RB, +20 h	7.2	20.1	735	86	540
Before stress	10.6	20.5	780	1.8	470
FB, 20 h	10.8	19.8	800	2.1	570
OC, +20 h	9.1	19.8	755	4.8	370
Before stress	10.5	20.0	785	1.9	544
FB, 20 h	10.0	19.3	780	1.9	540
RB, +20 h	7.4	18.8	730	25.5	440
Before stress	10.9	21.0	780	2.8	620
RB, 20 h	7.6	20.5	740	45.5	660
OC, +20 h	6.2	17.2	740	22.5	315
Before stress	10.4	19.7	785	3.0	650
RB, 20 h	6.9	19.3	735	60	640
FB, +20 h	6.9	20.0	685	6.9	550

It is seen from the table:

- The highest degree of the R_{se} degradation for 20 h testing is observed for the RB stress, the lowest (zero or even R_{se} improvement) for FB stress, while OC provides some intermediate increase in R_{se}. OC stress after FB leads to some increase in R_{se}, OC after RB decreases R_{se}. FB after RB provides a considerable recovery of R_{se}. RB after FB causes a significant increase in R_{se}, but its final value is three times lower than for RB stress only.
- FB and RB stresses for 20 h do not provide any degradation of R_{sh}, while OC stress for 20 h decreases R_{sh} by ~45%. It is seen that additional OC stress after FB or RB leads to a considerable R_{sh} degradation., while FB after RB and vice versa change R_{sh} much less.
- FB stressing itself does not cause a considerable degradation of V_{oc}, but when applied after RB, it leads to a considerable additional decrease in V_{oc}, which already has degraded

significantly due to the RB stress. OC stress causes 6.5% decrease in V_{oc} if applied after FB, but does not change V_{oc} after RB. This seems to be an observation that is difficult to explain invoking only electromigration.

5.2 Comparison of Degradation in Vapor Transport- and Electro- Deposited CdTe Solar Cells with Cu/ZnTe/Au and Cu/Au Back Contacts

Almost all groups working on CdTe solar cells have used Cu-doping via back contact application. The positive effect of Cu mainly comes from enhancement of V_{oc} and FF, the latter due to a significant decrease in the back contact resistance. While copper improves the initial performance of CdS/CdTe solar cells, it was found in many studies to deteriorate the cell stability [61, 62]. It is believed that one of the reasons is fast diffusion and electromigration of Cu in CdTe, especially along grain boundaries in polycrystalline films. That leads to expectation that morphology of CdTe film should impact Cu migration and degradation process. Indeed, degradation rates under different stress conditions and their peculiarities reported by various groups are different depending on the processing techniques, type and application method of the back contact. Studies presented in this section were aimed at clarifying some of these issues.

<u>Samples for studies. Stressing conditions</u>

Two types of CdS/CdTe structures were used in this study. One was provided by First Solar, LLC, (FS). It contains about 300 nm thick CdS and wet $CdCl_2$ treated 3.5 to 4.0 μm thick CdTe prepared with the gas transport deposition method. The other type was fabricated at CSM, containing 250 nm thick CdS (prepared with chemical bath deposition) and electrodeposited 3.3 μm thick CdTe. A wet $CdCl_2$ treatment was given to both CdS and CdTe [63].

Two types of back contacts were applied to the FS materials: ZnTe:Cu/Au and Cu/Au. For the first one, thin layers of Cu (7Å) and ZnTe (500Å) were evaporated on Br_2/methanol etched CdTe, and annealed in N_2 prior to evaporation of gold through mask to complete the back contact. For the second a thin Cu layer (30Å) was evaporated on the Br_2/methanol etched surface of CdTe and annealed in N_2. The excess Cu was removed by etching in Br_2/methanol solution, and Au was evaporated to complete the back contact. Cells on the CSM material were completed only with the Cu/Au back contact.

All three types of cells were stressed in dark at 100^0C in air under three bias conditions: open circuit (OC), forward bias of 0.55V (FB), and reverse bias of –1.2V (RB). Cells were periodically taken out of the oven and cooled down to room temperature before characterizing with I-V and C-V (at 100 kHz) techniques.

<u>Results of stress testing</u>

Fig. 5.1 shows the efficiency degradation under FB and RB conditions for the three types of cells: First Solar material (FS) with the first (Cu/ZnTe/Au) and the second (Cu/Au) types of back contact, and the CSM electrodeposited (ED) CdTe with the Cu/Au back contact.

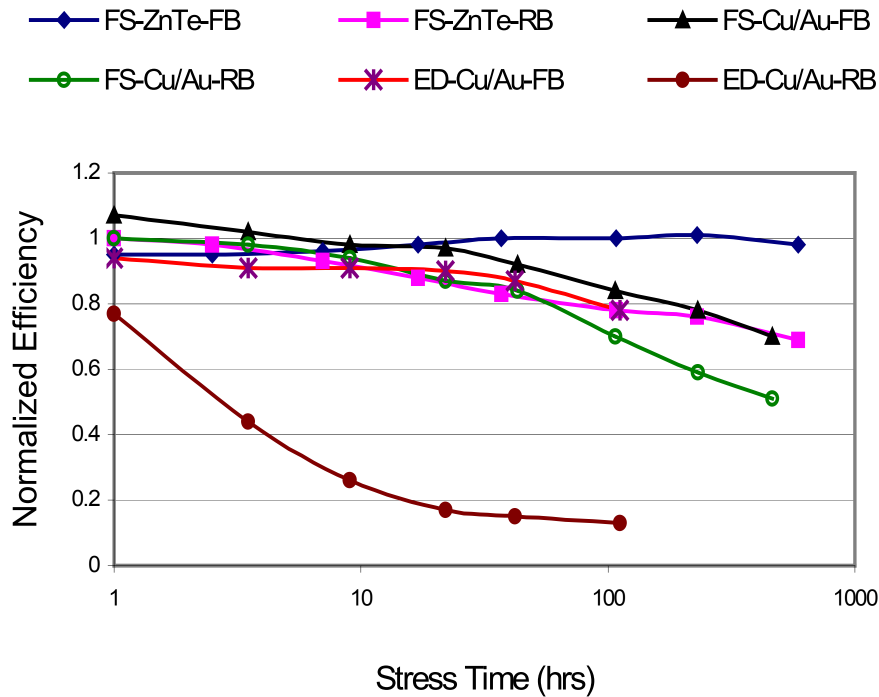

Fig. 5.1 Degradation of efficiency of various cells under FB and RB conditions

Cells stressed under FB (with any back contact) demonstrate the least degradation. FS-ZnTe cells show a decrease in efficiency by only 3% in 590 stressing hours while OC (not shown in the Figure) provided a 6% decrease for the same stressing time, and RB shows the most severe degradation of 33%. FS-Cu/Au samples show higher degree of degradation than that of the Cu/ZnTe/Au samples and different trend in efficiency change with time. Degradation is much more severe in the CSM (ED-Cu/Au) cells for all bias conditions, with the efficiency decreased by 80% under RB within 22 hours.

The trends in efficiency change in the initial hours of stressing are quite different for different back contacts. FS-ZnTe cells stressed under FB first manifest a decrease in efficiency by 6% (higher than decrease in 590 hours) followed by an increase. The behavior is opposite for the same samples stressed under OC with the initial increase in efficiency followed by decrease. Cu/Au back contact on the FS material manifests different trends. FB stressed cells show an initial increase in efficiency followed by a decrease, while OC-stressed cells show continuous decrease. Only reverse-biased cells showed almost the same trends of continuous decrease in both cases.

Pictograms in Fig.5.2 demonstrate visible differences in degradation of Voc and FF for various cells due to different bias conditions.

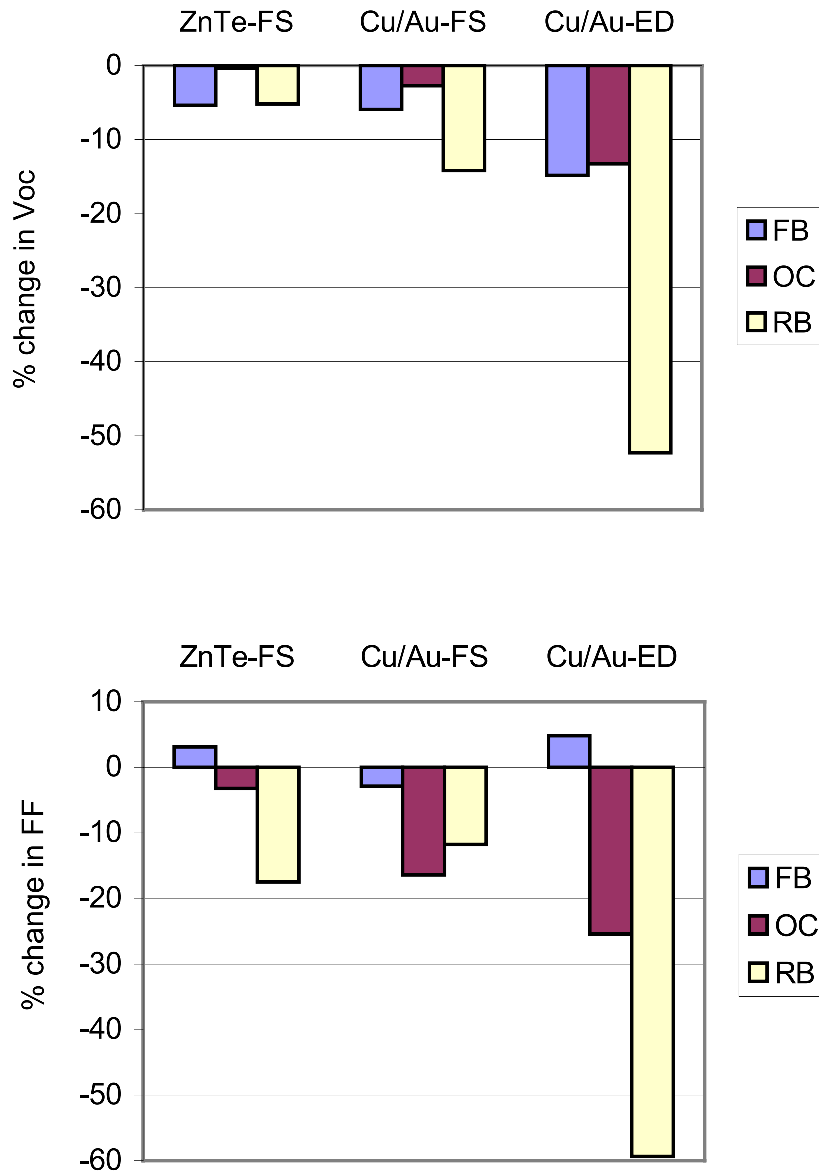

Fig. 5.2 Changes in fill factor (FF) and open circuit voltage (V_{oc}) after stressing for 110 hours

Differences in degradation of the cell parameters after various stress bias conditions correlate with differences in the doping-profile changes. Fig. 5.23 shows some data for the FS-ZnTe and ED-Cu/Au samples after 110 hour stressing as compared to the initial profiles. The following major features are to be mentioned:

- Doping density decreases after OC and FB stressing, while it increases after RB stressing. This correlates with changes in the depletion width derived from the zero bias capacitance
- RB stressing causes a peak in doping profile just at the depletion layer edge.

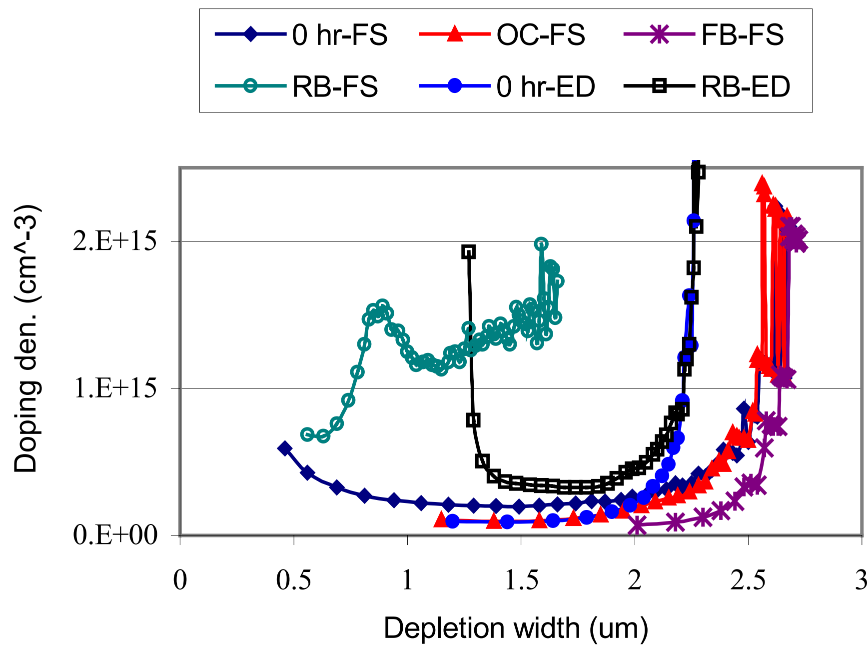

Fig. 5.3. Changes in doping profile for the FS-ZnTe and the CSM (ED) cells after 110 hours of stressing

5.3 Discussion

5.3.1 Major results of this study. Role of electromigration

The major results of the experimental studies presented above are as follows:

- Degradation of cells is accompanied and caused, at least partially, by significant changes in doping profile, which indicates spatial redistribution of electrically active defects.
- A strong influence of the applied bias during stressing should be attributed to a significant contribution of electromigration to this redistribution and maybe also to transformation of the defects in strong electric fields. The reversible effects found when stressing under varied bias provide an additional support to this conclusion. Distribution and redistribution of other charged defects should also be influenced by their drift in the built-in electric fields.
- The influence of the back contact type on the cell degradation and on changes in doping profile indicates that the Cu-related degradation process depends on the back contact structure. It should be concluded that the role of the ZnTe interlayer is not limited to providing low back contact resistance. Probably its presence also controls the Cu content and distribution throughout the cell.
- For the same back contact, degradation varies with the CdTe processing. Presumably it occurs due to the differences in the film morphology and the grain boundary properties as well as in imperfection of the intra-grain material.

We believe that the experimental studies presented above provide a strong evidence of a significant role of electromigration in the cell degradation. With respect to the Cu dopant in CdTe films and cells it was directly verified by PL studies [64]. To support this concept we present below some numerical estimates of a relative role of diffusion and drift in a spatial distribution/redistribution of ions during cell processing and stress testing.

To estimate approximately what dominates the charged defect migration (diffusion or drift), we used [60] the ratio of two characteristic lengths: Diffusion length, $L_{dif} \approx (Dt)^{1/2}$, and Drift length, $L_{dr} = \mu E t$, where D is an ion diffusion coefficient, μ is an ion mobility, and t is the time of the process duration. Based on the Einstein relation, $\mu = eD / kT$, it is easy to see that $L_{dr} / L_{dif} = (t / t^*)^{1/2}$, where $t^* = (kT / q)^2 / (E^2 D)$. The average built-in electric field in the CdTe depletion region in dark under OC condition is of the order of 10^4 V/cm. For T=100°C and $D \sim 10^{-12}$ cm^2/s and $D \sim 10^{-16}$ cm^2/s, the estimated t^* values are of ~10 s and ~28 hr, respectively. The first D is somewhat lower than the diffusion coefficient for fast Cu diffusion through the interstitials even at room temperature [14, 61]. A lower D is a realistic estimate for the substitution Cu_{Cd}^- diffusion through vacancies. It is seen that drift dominates diffusion in the first case even in the short time of cell fabrication. In the second case this effect should be expected for the long time stressing. Thus, at least for the high diffusivity Cu ions, the drift dominates diffusion.

Even though, we are not able to properly analyze and predict the time-dependent spatial redistribution of Cu in the CdTe/CdS cell. Indeed, the interstitial Cu_i^+ and substitutional Cu_{Cd}^- ions drift in the opposite directions in the same electric field. Both effects influence spatial distribution of Cu and the Cu-related donor and acceptor defects. Moreover, Cu_i^+ and Cu_{Cd}^- are not the only defects that determine electronic properties of CdTe film and a cell as a whole. When trying to clarify mechanisms of the cell degradation we face a much more general and complicated problem of identifying and studying of a variety defects that control electronic properties of the cell components and whose migration and transformation impact cell performance under stress and normal operation conditions. This problem is discussed below in more detail.

5.3.2 Some Basic Problems Behind Degradation Mechanisms and Possible Approaches to Their Solution

1. One of the high priority issues is the problem of the electrically active centers that determine the majority carrier concentration. Doping with Cu is commonly used to control the hole concentration in CdTe, but its concentration in CdTe detected by SIMS [65, 66] is orders of magnitude higher than the hole concentration provided by C-V profiling. This discrepancy is not specific for some processing method but is common for all. The major questions to be addressed are:
(a) What Cu-related defects dominate creation of free holes in CdTe: Cu_{Cd}, Cu-contained complexes, or acceptor-type native defects whose concentration depends on presence and concentration of Cu?

(b) What are the energy levels provided by the dominating acceptor centers: are those levels shallow or not, in other words, are they completely thermally ionized at room temperature or not? Most reports attribute the acceptor level of E_A-E_V ~ 0.3-0.35 eV found in CdTe:Cu to Cu_{Cd}. This level is deep enough to be much less than half thermally ionized at T=300 K, if the concentration of the centers exceeds 10^{14}cm^{-3}. For example, if E_A-E_V=0.35 eV and $N_{Cu_{Cd}} \approx 10^{16}$ cm^{-3}, the estimated free hole concentration at T=300K should be of $n_h \approx 5\times10^{14}$ cm^{-3}.

(c) Does a huge difference between N_{Cu} and n_h comes from involvement of the majority of Cu atoms in some neutral precipitates or neutral complexes? Or is there a high degree compensation of the acceptor centers by donor centers provided by Cu_i, or native defects or some complexes? For the shallow acceptors $n_h = N_A - N_D$, hence if $n_h << N_A$, the compensation degree is close to unity ($N_D / N_A \approx 1$). Even a small change in the ratio N_D / N_A can lead to a significant, by orders, change in the free hole concentration. It should be mentioned that in the case of dominating deep acceptors, the influence of compensation on the hole concentration could be even stronger than for shallow acceptors. For the deep acceptor like that in the example above (E_A-E_V=0.35 eV), $n_h \approx 2\times10^{13}$cm^{-3}, if $N_A \geq 10^{15}$cm^{-3} and $N_D / N_A \approx 0.5$, no matter what is the real N_A value.

(d) What is the influence of the deep electronic states associated with grain boundaries (GB) on the hole concentration in CdTe? Previous studies of the CdTe bicrystals [8] and polycrystalline thin films [2, 3] (see also Sec. 1.1) have shown that in the latter with a grain size of ~ 1 μ, the number of the GB states per unit volume can be as high as 10^{16} to 10^{17}cm^{-3}. That means that the GB states can effectively compensate acceptors in the grain volume (deplete the grain bulk). The difference between this compensation mechanism and that considered above is that in the previous case the film is overall as well as locally neutral, while in the latter case grain boundaries are charged positively and the grain bulk is charged negatively, so that film is neutral as a whole but not locally. It should be mentioned that in the case of dominating compensation by the GB states, the negative space charge density in the GB proximity, should be close to N_A and can be much higher than the free hole concentration derived from the C-V profile. Thus the enhanced space charge density ($\geq 10\times10^{17}$cm^{-3}) in the GB region observed in [2, 3] may be explained in particular by the GB compensation mechanism, although accumulation of the acceptor-type defects in the GB region also cannot be excluded.

2. A specific and important issue to be addressed is the presence of deep traps and their influence on carrier concentration, space charge density in the depletion layer in a cell and recombination processes.

(a) Although a few publications are devoted to detection and studies of deep traps in CdTe, e.g., [53-57, 67], the problem is far from clear. Numerous deep trap levels were reported so far, but the centers responsible for them have not been identified unambiguously. The sets of the deep levels reported in different publications are not the same and depend on the processing technology, postdeposition treatment, and morphology of polycrystalline films. That leads to an additional uncertainty in identification of the centers. One may expect that some of deep levels detected in the thin film CdTe-based solar cells originate from the CdTe/CdS interface and from the GB's inside the CdTe layer.

(b) If one believes that a high compensation degree takes place in CdTe, it is reasonable to expect deep traps of high concentration, higher than the free hole concentration. Our studies presented in Sec.4 verify this expectation. These traps of high concentration can influence

significantly the magnitude and spatial distribution of the space charge, hence the "doping level"- depth profile obtained with the standard analysis of C-V measurements.

3. It is believed that GB affect strongly the cell performance. The role and mechanisms of their influence on the electronic properties of thin film CdTe solar cells are not understood properly. Here we will discuss some of them:

(a) Presence of potential barriers for the majority carriers at the GB was demonstrated both for the CdTe bicrystals and polycrystalline films. That means two- or three-dimensional non-uniformity in the electrostatic potential distribution, hence rather non-uniform electron transport in thin-film CdTe cells. Potential relief separates spatially electrons and holes reducing the recombination rate. On the other hand, deep GB states that are responsible for the potential barriers can act themselves as the recombination centers.

(b) Diffusion of impurities and defects may be expected to be faster along the grain boundaries. This expectation was verified for interdiffusion at the CdTe/CdS interface [41, 43]. It was shown, although indirectly, that concentration of the ternary phase and the S content is higher in the GB regions. The evidence of rapid diffusion of Cu in polycrystalline CdTe due to GB was clearly demonstrated in [68, 69]. Probably the rates of electromigration, which is well manifested for Cu in CdTe are also different for the bulk material and the GB regions. GB are prone to attract and accumulate structural defects and impurities as well as to serve as nuclei for precipitates. It should be mentioned that usually we are not well aware whether these effects are beneficial (e.g. "passivation" of grain boundaries, whatever it means) or detrimental for the cell performance. Anyway, grain boundaries can strongly affect the spatial distribution of the species vital for the cell performance, especially in the fine grain structures like CdTe and CdS thin films. Migration along the GB, especially for fast diffusing species such as Cu, should also lead to their significant redistribution under varying stress conditions and hence may be an important factor in the degradation processes.

4. The problems presented above were discussed mostly with respect to the absorber, CdTe, layer of our cells. But the similar problems are also important for the window CdS and TCO layers.

(a) The initial doping level in n-CdS and its changes under cell stressing can strongly impact the spatial distribution of the built-in potential in a cell and the dominant transport mechanism of carriers through the CdS layer: diffusion, drift, or ballistic mechanism. Deep electronic states in the bulk of CdS and in the vicinity of CdS/CdTe interface can act as recombination centers. All this impacts photocurrent collection and cell performance. Defects that can influence the electronic properties of CdS are: native defects, impurities, such as Cl, Cu, Sn, Na, as well as the complexes that involve these impurities. For example, it was shown ([70, 71]) that the different postdeposition treatments of CdS films (with and without $CdCl_2$) significantly influence their optical, electrical and photoelectrical properties. In particular, it was found that $CdCl_2$ treatment results in the decrease in the shallow defect density, the increase of the bandgap and the photoconductivity response. Diffusion of Te into CdS leads to appearance of effective recombination centers. SIMS measurements on CdTe/CdS cells have shown [61, 72, 73] that Cu concentration in CdS could be very high, achieving the level of 10^{19} cm^{-3}. The SIMS profiling of the stressed cells indicates an additional accumulation of Cu dopant in CdS [74]. It is unclear as yet how Cu atoms that penetrated into CdS are spread between grain bulk and grain boundaries. Presumably, Cu migrates into CdS predominantly along the grain boundaries and most part of it

stays there just after cell processing or at the initial stages of stressing. But it is quite probable that under continued stressing and, maybe, after long period of operating under normal conditions, the amount of Cu in the grain bulk increases. Our recent PL studies of Cu doped CdS films and cells [75] have shown that the PL red band (1.55 to 2.3 eV) increases in intensity with the addition of Cu. Usually, Cu is thought to introduce the midgap states that contribute to this PL band [76]. At the same time the yellow band (2.35 to 2.55 eV) becomes increasingly quenched and totally disappears when CdS:Cu is annealed at enhanced temperatures. The origin of yellow band is commonly attributed to transitions from a donor level, introduced by interstitial Cd, to the valence band. Its disappearance can be explained by emptying of these states due to the Fermi level shift down in the depth of the bandgap. This suggestion is consistent with the results of Hall measurements that indicated conversion of the film to p-type when it is annealed with Cu at enhanced temperature. We suppose that this anneal promotes the Cu diffusion in the grain bulk.
(c) It has not yet been paid much attention to possible degradation of TCO layer. However, one cannot exclude interaction between fluorine and native defects, diffusion of sodium or other species from the glass substrate as well as of S, Te, Cl, Cu, etc., from other components of a cell. One of the possible effects of the composition changes is compensation of the donor dopant, hence shift in the plasma reflection edge, reducing mobility, increase in absorption due to the free electron scattering.

5. To clarify the fundamental problems listed above and some other relevant to the cell performance and stability, especially the nature of defects and corresponding electronic states that control electronic properties of a cell, we need to develop a variety of approaches to experimental studies, methods and techniques for the film and cell characterization, and approaches of the data analysis. Some of them are discussed below.

(a) As shown in Sec. 1, the in-plane electrical characterization of the CdTe films, using measurements of Hall effect, resitivity, and impedance spectroscopy can provide a vast information on electronic properties of the grain bulk material and of grain boundaries. In particular, these studies under varying illumination spectrum and intensity provide more reliable estimates of carrier concentration and mobility in the grain bulk. Analysis of temperature-dependent concentration with the appropriate multi-level model will clarify the problem of the defect electronic states that dominate the majority carrier concentration and help estimate the role and degree of compensation. The light-dependent Hall measurements could be used as an independent method for the effective lifetime of the minority carriers which determines effectiveness of the photocurrent collection and could be different from the estimates provided by the time-resolved photoluminescence. The former can be higher than the latter due to spatial separation of electrons and holes by the GB potential barriers and potential fluctuations in the grain bulk.
(b) The temperature-, light-, and bias-dependent impedance spectroscopy provides a detailed information on the GB electronic states, their density and distribution over the energy range, as well as their influence on photo-electrical properties of a material.

Of a special interest are studies conducted on CdTe films extracted from the cells with the “lift-off” techniques, e.g., those developed at NREL (L. Woods, D. Levi) and at the CSM. The lift-off samples are particularly valuable, as surrogate films deposited on glass may not have the same

properties as those in a cell, even if similar postdeposition treatments and stress tests were applied.

Our studies (not presented in this report) demonstrated feasibility of applying the above methods also to the analysis of CdS films deposited on the insulating substrates. (We were not able to apply the "lift-off" technique to thin CdS films).

The TCO films extracted from the degraded cell with the "lift-off" technique followed by etching of the CdS residuals can be tested using the methods described in Sec.2. Electrical and optical characterization should be accompanied with compositional and structural studies.

(b) The admittance spectroscopy of CdTe cells proved to be an effective method for detection and studies of deep traps (see Sec. 4). With this technique applied in the temperature, bias and light intensity ranges, one is able to detect deep states, evaluate their concentration, Density of states function, estimate capture cross sections and the trap energy levels/bands. Comparison of admittance spectroscopy with the DLTS studies should verify or correct and detail the information obtained. For very slow traps a suitable method is examination of long time, non-exponential transient effects in admittance. The obtained data on deep states, especially of high concentration, will provide more correct analysis of C-V profiles aimed at determination of the "doping level" (space charge density distribution) in a cell.

(c) Studies of photoluminescence can be useful for identifying defects responsible for particular electronic states. For this purpose one should correlate specific features of the PL spectra and their intensities with the processing procedure and information on concentration of specific defects/dopant and electronic states obtained by other methods. Another objective is to find some PL "signatures" for future monitoring of impurities/defects concentrations, spatial distribution/redistribution and transformations both in films and cells. PL studies of this kind on CdTe are presented, e.g., in Ref. 64. Recently we tried to apply this method with some success to study Cu impurity in CdS.

(d) Information similar to that provided by PL can also be obtained using electroluminescence (EL). Recently we obtained EL in the spectral range close to the CdTe bandgap (~1.4-1.62 eV) on cells fabricated using the material supplied by First Solar. The low temperature spectrum (T~20K) was measured at the forward current densities of 27 and 49 mA/cm^2 and demonstrated the fine structure identical to the PL spectrum. The high temperature EL (above room temperature) was observed and measured at current densities of 230 to 1180 mA/cm^2. This spectrum did not reveal fine structure but in general was similar to the PL one. Preliminary experiments on mapping EL over the cell area seem promising. We hope that this could be a good method for non-destructive characterization of cells and, in particular, for detecting non-uniformities of electronic properties of a cell and monitoring their evolution in the course of stressing.

(e) For polycrystalline materials it is very important to develop high spatial-resolution methods that make it possible to monitor and map the cell/film properties on a scale much less than the average CdTe grain Near Field Scanning Optical microscopy (NSOM) provides spatial resolution of 100 nm and less. This technique in the photocurrent operational mode was in

particular applied at the CSM to experimental verification and studying of the GB-assisted sulfur diffusion in CdTe (see Sec.3). We are starting to develop this technique to provide also mapping optical characteristics and PL on cells and films. It will enable studying content, spatial distribution and influence of S and other species, such as Cu, in the as prepared cells and films as well as in the degraded ones. Based on the specific PL signature of a defect, NSOM measurements will estimate local concentration of this defect on the scale much less than the grain size. In particular this method will be used for monitoring distribution of Cu between GB and the grain bulk.

Scanning tunneling spectroscopy (STS) performed in vacuum on clean surfaces with a scanning tunneling microscope (STM) can provide local density of state information. Changes in midgap states, particularly in materials with large defect concentration can be probed on a nm scale, allowing examination of individual grains or changes over the thickness of the film. STM and local tunneling spectroscopy can provide information on electronic states localized to grain boundaries and variations in electrostatic potential. STM and AFM measurements can be used to microscopically characterize potential variations across GB. Previous measurements on photovoltaic materials have shown measurable changes in potential and collected current

6. REFERENCES

1. J.J.. Kester, S. Albright, V. Kaydanov, R. Ribelin, L.M. Woods, J.A. Philips*, NREL/SNL PV Program Review, Proc 14th Conf*., Lakewood, CO, 1996, p. 162.

2 L.M. Woods, D.H. Levi, V. Kaydanov, G.Y. Robinson, R.K. Ahrenkiel*, Proc. 2nd World Conf. on PV Solar Energy Conversion*, July 1998, Vienna, Austria, p.1043.

3. A.S. Gilmore, V. Kaydanov, U. Laor, A. Gupta, T.R. Ohno, B. McCandless, *NCPV Progr. Rev. Meeting 2000*, April 2000, Denver, CO, p.259.

4. V.I Kaydanov and T.R Ohno, "Process Development and Basic Studies of Electrochemically Deposited CdTe-Based Solar Cells", Colorado School of Mines, Annual Technical Report to NREL, Subcontract No. XAK-8-17619-28, Phase I, 15 May 1998-14 May 1999.

5. Y. Matukura, *Jpn. J. Appl. Phys*. **2**, 91 (1963).

6. W.E. Taylor, N.H. Odell, and H.Y. Fan, *Phys. Rev*. **88**, 867 (1952);
R. Stratton, *Proc. Phys. Soc*., London, **B 69**, 513 (1956).

7. M.G. Spencer, W.J. Schaff and D.K. Wagner, *J. Appl. Phys*. **54**, 1429 (1983).

8. T.P. Thorpe, Jr., A.L. Fahrenbruch, and R.H. Bube, *J. Appl. Phys*. **60**, 3622 (1986)

9.` M. Matsuoka, *Jpn. J. Appl. Phys*. **10**, 736, (1971); L.M. Levinson and H.R. Philipp, *J. Appl. Phys*. **46**, 1332(1975).

10. G.E. Pike and C.H Seager, *J.Appl. Phys*. **50**, 3414 (1979).

11. C.H. Seager and G.E. Pike, *Appl. Phys. Lett*. **37**, 747 (1980).

12. G.E. Pike, "Grain Boundaries in Semiconductors", Elsevier Science Publ. Co., Inc., 1982, p. 369.

13. G.H. Blount, R.H. Bube, and A.L. Robinson, *J. Appl. Phys*. **41**, 2190 (1970).

14. Lyubomirsky, I., Rabinal, M.K., and Cahen, D., *J. Appl. Phys*. **81**, 6684 (1997).

15. K. Zanio "Cadmium Telluride" (Ser. Semiconductors and Semimetals, vol.13), Acad. Press, New York-San Francisco-London, 1978, (see p.110).

16. I. G. Haacke, *J. Appl. Phys.* **47,** (1976), 4086.

17. E. Burstein, *Phys. Rev.* **93**, 632 (1954).

18. T.J. Coutts, D.L. Young and X. Li, *MRS Bulletin*, **25**, No.8, 58 (Aug. 2000).

19. D.L. Young, T.J. Coutts, V.I. Kaydanov, W.P. Mulligan, to be published in *J. Vac. Sci. Technol.* **A 18,** No. 6, Nov-Dec. 2000.

20. D.L. Young, "A Fundamental Study of Electron Transport in Zinc Stannate Thin Films", Ph.D Thesis, Department of Physics, Colorado School of Mines, Golden, CO, 2000.

21. J. Kolodziejchak and S. Zhukotynski, *Phys. Status Solidi* **5**, 145 (1964).

22. W. Zawadski and J. Kolodziejchak , *Phys. Status Solidi* **6**, 419 (1964).

23. M.K. Zhitinskaya, V.I. Kaidanov, and I.A. Chernik, *Sov. Phys. Solid State* **8**, 295 (1966).

24. I.A. Chernik, V.I. Kaidanov, E.P. Ishutinov, *Sov. Phys. Semicond.* **2**, 825, (1969).

25. T.S. Gudkin, V.I. Kaidanov, et.al., *Sov. Phys. Semicond.* **5**, 1089 (1971).

26. E. Putley, "The Hall Effect and Related Phenomena", Butterworths, London, 1960.

27. W.P. Mulligan, "A Study of the Fundamental Limits to Electron Mobility in Cadmium Stannate Thin Films", Ph. D. Thesis, Department of Physics, Colorado School of Mines, Golden, CO, 1997.

28. D.L. Young, T.J. Coutts, V.I. Kaydanov, *Rev. of Sci. Instr*. **71**, 462 (2000).

29. A. M. Alkaoud, "APCVD Preparation and Studies of Physical Properties of Tin Oxide Thin Films", Ph. D. thesis, Department of Physics, Colorado School of Mines, Golden, CO, 1999.

30. A. Al-Kaoud, T. Wen, A. Gilmore, V. Kaydanov, T.R Ohno, C. Wolden, L. Feng, J. Xi, *NCPV Progr. Rev., Proc. 15th Conf.*, Denver, CO, 1998, p.212.

31. T.S Gudkin, I.A. Drabkin, V.I. Kaidanov, O.G. Sterlyadkina, *Sov. Phys. Semicond.* **8**, 1453 (1975).

32. L.I. Bytenskii, S.A. Kaz'min, V.I. Kaidanov, Yu.I. Ravich, and A.V. Savel'ev, *Sov. Phys. Semicond.* **16**, 712 (1982).

33. O. Madelung, Semiconductors other than Group IV Elements and III-V Compounds, Springer-Verlag, Berlin-Heidelberg, New York 1992.

34. B. M. Askerov, Electron Transport Phenomena in Semiconductors, World Scientific, Singapore, 1994.

35. H. Brooks, *Advances in Electronics and Electron. Phys.* **7**, (1955), 87.

36. R. Mansfield, *Proc. Phys. Soc. B*, **69,** (1956), 79.

37. V.I. Kaidanov and I.A. Chernik, *Sov. Phys. Semicond.* **1**, 1159 (1967).

38. S. Brehme, F. Fenske, W. Fuhs, E. Nebauer, M Poschenrieder, B. Selle, and I. Sieber, *Thin Solid Films* **342**, 167 (1999).

39. K.H. Hellwege, "Landolt-Bornstein numerical data and functional relationships in science and technology: Semiconductors", in *Numerical Data and Functional Relationships in Science and Technology*, edited by O. Madelung, M. Scultz, and H. Weiss (Springer, Berlin, 1982), vol. 17.

40. S. Bloom and I. Ortenburger, *Phys. Status Solidi* **B 58**, 561 (1973).

41. D. Mao, L. H. Feng, Y. Zhu, J. Tang, W. Song, R. Collins, D. L. Williamson, and J. U. Trefny, *13th NREL PV Program Review Proc.*, AIP Conference Proc. 353, p.352 (1996).

42. D.G. Jensen, B.E. McCandless and R.W. Birkmire, *Proc. 25th IEEE PVSC*, Washington, DC, May 1996, p. 773.

43. M. H. Aslan, W. Song, J. Tang, D. Mao, R. T. Collins, D. H. Levi, R. K. Ahrenkiel, S. C. Lindstrom, and M. B. Johnson, *Mat. Res. Soc. Symp. Proc.*, **485** p.203 (1998).

44. G.A. Valaskovic, M. Holton and G.H. Morrison, *Applied Optics* **34**, 1215 (1995).

45. E. Betzig, P.L. Finn and J.S. Weiner, *Appl. Phys. Lett.* **60**, 2484 (1992).

46.K. Ohata, J. Saraie and T. Tanaka, *Jap. J. Appl. Phys.* **12**, 1641 (1973).

47. D.S. Albin, private communication.

48. O. deMelo, M.Melendez-Lira, I. Hernandez-Calderon, L. Banos, and A. Morales-Acevedo, Proc. *1st IEEE World Conf. on Photovoltaic Solar Energy Conversion*, New York,1994, p.369.

49. M.S. Unlu, B.B. Goldberg, W.D. Herzog, D. Sun and E. Towe, *Appl. Phys. Lett.* **67**, 1862 (1995).

50. P. Blood and J.W Orton, "The Electrical Characterization of Semiconductors: Majority Carriers and Electron States", Academic Press, 1992.

51. Ahmet Balcioglu, "Characterization of Deep Impurity Levels in Semiconductor Devices", Ph.D. Thesis, Department of Physics, Colorado School of Mines, Golden, CO, 2000.

52. A. Balcioglu, R.K. Ahrenkiel and F. Hasoon (submitted for publication to *J.Appl. Phys.*, 2000).

53. F. Abou-Elfotouh, S. Ashour, S.A. Alkuhaimi, J. Zhang, D.J. Dunlavy, L.L. Kazmersky, *Mat. Res. Soc. Symp. Proc*. **238**, 335, (1992).

54. A. Castaldini, A. Cavalinu, B. Fraboni, P. Fernandez, J. Piqueras, *J. Appl. Phys*. **83**, 2121 (1998).

55. M.A. Lourenco, Y.K. Yew, K.P. Homewood, K. Durose, H. Richter, and D. Bonnet, *J. Appl. Phys*. **82**, 1423 (1997).

56. M.A. Lourenco, W.L. Ng, K.P. Homewood, and K. Durose, *Appl. Phys. Lett*. **75**, 277 (1999).

57. G. Zoth, F.G. Reidel, W. Schroter, *Phys. Stat. Sol*. **B 172**, 187 (1992).

58. A.J. De Nobel, *Phil. Re. Rep*. **14**, 430 (1959).

59. Jian Tang, "Study of Back Contact Formation on CDTe/CdS Thin Film Solar Cells", Ph.D Thesis, Department of Physics, Colorado School of Mines, Golden, CO, 2000.

60. D. Morgan, J. Tang, V. Kaydanov, T.R. Ohno, and J.U. Trefny, *NCPV PV Progr. Rev. 15th Conf.,* Denver, Colorado, Sept 1998, p. 200.

61. K. D. Dobson, I. V. Fisher, G. Hodes and D. Cahen, *Solar Energy Mater. & Sol. Cells* **62**, 295-325 (2000).

62. J. Tang, D. Mao, T. R. Ohno, V. Kaydanov and J. U. Trefny, *Proc. 26th IEEE PVSC*, Sept.–Oct. 1997, Anaheim, CA, pp 439-442.

63. W. Song, D. Mao, Y. Zhu, J. Tang and J. U. Trefny, *Proc. 25th IEEE PVSCP*, May 1996, Washington, DC, pp 873-876

64. D. Grecu, "Photoluminescence Study of Cu-doped CdTe and Related Stability Issues for CdS/CdTe Solar-Cell Devices" Ph.D Thesis, The University of Toledo, August 1999.

65. H.C. Chou, A. Rohatgi, E.W. Thomas, S. Kamra, A.K. Bhat, *J. Electrochem. Soc*. **142**, 254 (1995).

66. S.E. Asher, R.C. Reedy, Jr., R. Dhere, T.A. Gessert, M.R. Young, *NCPV Progr. Rev. Meeting 2000*, April 2000, Denver, CO, p.275

67. E.Kucys, J. Jernot, K. Bertulis, and V. Bariss, *Phys. Stat. Sol.***A 59**, 91 (1980).

68 H.C. Chou, A. Rohatgi, N.M. Jokerst, E.W. Thomas, S. Kamra, *J. Electron. Mater*. **25,** 1093 (1996).

69 M.K. Herndon, A. Gupta, V. Kaydanov and R.T. Collins, *Appl. Phys. Lett.* **75**, No. 22, pp. 3503-3505 (1999).

70. W. Song, D. Mao, J.U. Trefny, R.K. Ahrenkiel, D.H. Levi, and S. Johnston, *NCPV PV Progr. Rev. 15th Conf.,* Denver, Colorado, Sept 1998, p. 188.

71. W. Song, D. Mao, V. Kaydanov, T.R Ohno, J.U. Trefny, R.K. Ahrenkiel, D.H. Levi, S. Johnston, B.E. McCandless, Ibid, p.194.

72. C.Narayanswamy, T.A. Gessert, and S.E. Asher, Ibid. p. 248

73. S.E. Asher, R.C. Reedy, Jr., R. Dhere, T.A. Gessert, M.R. Young, Ibid. p.275

74. S.E. Asher, F. Hasoon, P. Sheldon, J. Sites, J. Hiltner, in *National CdTe R&D Team Meeting Minutes,* Golden, CO, January 2000, Appendix 17, Part II.

75. S.W. Townsend, T.R. Ohno, V. Kaydanov, A.S. Gilmore, J.D. Beach, *Transactions of MRS Meeting,* San Francisco, CA, April 16-20, 2001, (in press).

76. N.S. Bogdanyuk, *Semiconductors* **29**, 181 (1995).

7. ACKNOWLEDGEMENTS

Many people, in addition to those at the Colorado School of Mines, have contributed to this work over the past three years. We are thankful to Rick Powell, Doug Rose, Victor Karpov, Don Grecu, and Upali Jayamaha of First Solar, LCC., for supplying us with the materials for CdTe/CdS cells preparation and for thin film studies. It is hard to underestimate the value of discussions of our research approach and results that we have had with the individuals mentioned above and also Bolko von Roedern, Tim Gessert, Dave Albin, Peter Meyers, James Sites, Alan Fahrenbruch, and other scientists involved in fabrication and studies of thin film solar cells. We greatly appreciate the encouraging interest in our activities, discussions and suggestions we get constantly from Kenneth Zweibel, Harin Ullal, and especially from our contract monitor, Bolko von Roedern.

8. APPENDICES

8.1 Personnel

The names, titles, and representative responsibilities of the individuals contributed to this work are summarized below.

Timothy R. Ohno, Associate Professor of Physics: Photovoltaic Development, Surface Physics, Principal Investigator

Victor I. Kaydanov, Research Professor of Physics: Photovoltaic Development, Electron Transport Phenomena, Principal Investigator

Reuben T. Collins, Professor of Physics: Electronic and Optical Properties of Semiconductors

Don L. Williamson, Professor of Physics: Structural Properties of Materials, XRD

Thomas E. Furtak, Professor of Physics: Optical Properties of Semiconductors, Ellipsometry

Colin Wolden, Assistant Professor of Chemical Engineering: APCVD System Design

Dr. Timothy J. Coutts (NREL): Electronic and Optical Properties of Semiconductor Materials and devices

Dr. Richard K. Ahrenkiel (NREL), Adjunct Professor of Physics: Electronic and Optical Properties

Dr. Dean H. Levi (NREL): Electronic and Optical Properties of Semiconductor

Dr. Uri Laor, Visiting Scientist: Impedance Spectroscopy of Thin Polycrystalline Films

Dr. Akhlesh Gupta, Post. Doc.: CdTe Cell Processing and Characterization

Tinjung Wen, Research Associate: TCO Processing and Characterization

Dr. Jianping Xi (Green Development, LCC): APCVD System Design, TCO Processing

Dr. Lianghuan Feng (Green Development, LCC.): TCO Processing and Characterization

Wenjie Song, Graduate Research Assistant: CdTe Electrodeposition and Cell Optimization. (defended PhD thesis January 1999)

M. Hasan Aslan, Graduate Student: Photoluminescence, Interdiffusion Studies (defended PhD thesis January 1999)

Ahmed Alkaoud, Graduate Student: Tin Oxide Processing and Studies (defended PhD thesis April 1999)

Mary K. Herndon, Graduate Research Assistant: Near Field Scanning Optical Microscopy (defended Ph.D. thesis November 1999)

Ahmed Balcioglu, Graduate Student: Deep Level Transient Spectroscopy (defended Ph.D. thesis August 2000)

David L. Young, Graduate Student: Electron Transport Phenomena in Semiconductors (defended Ph. D. thesis August 2000)

Don Morgan, Graduate Research Assistant: Degradation of Solar Cells (Defended MS thesis July 2000)

Yoxa Mahathongdy, Graduate Research Assistant: CdTe Solar Cell Processing (Defended MS thesis 1999)

Angelo S. Gilmore, Graduate Research Assistant: Impedance Spectroscopy, Hall effect, Ellipsometry

Scott Townsend, Graduate Research Assistant: ZnTe Back Contact, Cell Stability

Brian Egaas, Graduate Research Assistant: Thin Film Solar Cell Fabrication

Wendi Batchelor, Graduate Research Assistant: Thin Film Solar Cell Fabrication

Don Robb Sparks, undergraduate student, degradation chamber design

8.2 Laboratory Improvements

Significant laboratory improvements occurred during this subcontract that have permitted more thorough materials characterization. In particular the following equipment was added to that we had at the beginning of the project:

1. A Hewlett-Packard LCR meter, Model 4285 (75KHz-30MHz) for Impedance/Admittance Spectroscopy of polycrystalline thin films and solar cells. Computer interfacing with a graphical programming language, HPVee, provides great flexibility in the type of automated measurements and analysis available.

2. A Hewlett-Packard LCR meter, Model 4284A (20 Hz - 1 MHz). Broadening of the frequency range provided more opportunities for studying electronic properties of grain boundaries, detecting and studying deep traps.

3. Building of the near field scanning optical microscope was completed, which enabled studying and mapping optical and electronic properties of the cell with the spatial resolution of ~100 nm.

4. A new tunable Ti-spphire laser from SpectraPhysics is being used for energy dependent near-field scanning microscopy studies.

5. A new Nanoscope probe microsope has been used, under the DOE University PV Research Equipment Program, award No. AAD-8-18669-04.

6. A gas phase optical monitoring system was chosen from Ocean Optics in support of subcontract ZAK-8-17619-13, Atmospheric Pressure Chemical Vapor Deposition for High Efficiency Thin Film PV.

7. The Lake Shore's Hall Effect/Electronic Transport Measurement System , Model 7507, with the close cycle refrigerator, switching and high sensitivity option provides an opportunity to measure resistivity, Hall coefficient, mobility and magnetoresistance in bulk and thin film samples in the temperature range from 15K to 350K. The samples could be measured in the resistance range of 100μΩ-200GΩ, with carrier concentration up to $6x10^{23}$ cm^{-3} (in thin films).

8. The MMR computer-controlled Seebeck Measurement System measures the thermopower voltage with a resolution of 50 nV over the precisely-controlled temperature rang 80-730K.

The Lake Shore and MMR systems were acquired under the DOD University Research program, award No. DAAD 19-00-1-0149.

8.3 Publications

1. A.S Gilmore, A. Al-Kaoud, V. Kaydanov, T.R. Ohno, “Mobility in SnO_2:F Thin Polycrystalline Films”, Transactions of MRS Meeting, San Francisco, CA, April 16-20, 2001, (in press).

2. A.S. Gilmore, V. Kaydanov, T.R. Ohno, D. Grecu and D. Rose, “ Impedance Spectroscopy and Hall Measurements on CdTe Thin Polycrystalline Films”, Ibid.

3. S.W. Townsend, T.R. Ohno, V. Kaydanov, A.S. Gilmore, J.D. Beach, “The Influence of Stressing at Different Biases on the Electrical and optical Properties of CdS/CdTe Solar Cells”, Ibid.

4. T.R. Ohno, E. Sutter, J. Kestner, A.S. Gilmore, V. Kaydanov, C.A. Wolden, P.V. Meyers, L.Woods, M.J. Romero, M.M. Al-Jassim, S.Johnston, “Microscopic Characterization of Polycrystalline APCVD CdTe Thin Film PV Devices”, Ibid.

5. V.I. Kaydanov, T.J. Coutts, and D.L. Young, “Studies of Band Structure and Free-Carrier Scattering in Transparent Conducting Oxides based on Combined Measurements of Electron Transport Phenomena” (invited paper), in *Proc. of the MRS Workshop ”Transparent Conducting Oxides (TCOs)”*, June 19-20, 2000, Denver, CO, 20 pages

6. A.S. Gilmore, V. Kaydanov, U. Laor, A. Gupta, T.R. Ohno, B. McCandless, “AC Characterization of the Grain Boundary Electronic Properties in CdTe Thin Films”, *Proc. of NCPV Progr. Rev. Meeting 2000*, Denver, Colorado, April 2000, pp. 259-260.

7. A. Gupta, S. Townsend, V. Kaydanov and T.R Ohno, “Comparison of Degradation in Vapor Transport- and Electro-Deposited CdTe Solar Cells with ZnTe:Cu/Au and Cu/Au Back Contacts”, Ibid, pp.271-272.

8. D.L. Young, T.J. Coutts, V.I, Kaydanov, “Density-of-states effective mass and scattering parameter measurements by transport phenomena in thin films”, *Rev. Sci. Instr.* **71**, No.2, 462 (2000).

9. D.L. Young, T.J. Coutts, V.I. Kaydanov, “ Density-of-States effective mass and scattering parameter measurements by transport phenomena in thin films”, *Rev.Sci. Instr.* **71**, 462 (2000).

10. D.L. Young, T.J. Coutts, V.I. Kaydanov, W.R. Mulligan, “Direct Measurement of Density-of-States Effective Mass and Scattering Parameter in Transparent Conducting Oxides Using Second-Order Transport Phenomena” *J. Vac. Sci. Technol.* **A 18(6)**, 1 (2000).

11. M.K. Herndon, A. Gupta, V. Kaydanov and R.T. Collins, “Evidence for Grain Boundary Assisted Diffusion of Sulfur in Polycrystalline CdS/CdTe heterojunctions”, *Appl. Phys. Lett.* **75**, No. 22, pp. 3503-3505 (1999).

12. W. Song, D. Mao, J.U. Trefny, R.K. Ahrenkiel, D.H. Levi, and S. Johnston, “Influence of $CdCl_2$Treatment on the Electrical and Optical Properties of CdS Thin Films”, *NCPV PV Progr. Rev. 15th Conf.,* Denver, Colorado, Sept 1998, p.p 188-193.

13. W. Song, D. Mao, V. Kaydanov, T. R. Ohno, J.U. Trefny, R.K. Ahrenkiel, D.H. Levi, S. Johnston, B.E. McCandless, “Effect of Optimization of CdS/CdTe Interdiffusion on CdTe Electrical Properties and CdS/CdTe Cell Performance”, Ibid. pp. 194-199.

14. D. Morgan, J. Tang, V. Kaydanov, T.R. Ohno, and J.U. Trefny, “Degradation Mechanism studies in CdS/CdTe Solar Cells with ZnTe:Cu/Au Back Contact”, Ibid. pp.200-205.

15. A. Al-Kaoud, T. Wen, A. Gilmore, V.Kaydanov, T.R. Ohno, C. Wolden, L. Feng, J. Xi, “Atmospheric Pressure Chemical Vapor Deposition of SnO_2: Processing and Properties”, Ibid. pp. 212-217.

16. L.M. Woods, D.H. Levi, V. Kaydanov, G.Y. Robinson, and R.K Ahrenkiel, “Electrical Characterization of Etched Grain-Boundary Properties from As-Processed px-CdTe-Based Solar Cells”, Ibid. pp. 499-504.

17. L.M. Woods, D.H. Levi, V. Kaydanov, G.Y. Robinson, R.K. Ahrenkiel, “Electrical Characterization of CdTe Grain-Boundary Properties from As Processed CdTe/CdS Solar Cells”, *Proc. of the 2nd World Conf. on Photovoltaic Solar Energy Conversion*, July 1998, Vienna, Austria, pp. 1043-1046.

8.4 Presentations at the Natonal CdTe R&D Team Meetings

January 25-26, 2001, Colorado School of Mines, Golden, Colorado

1. A.S. Gilmore, V. Kaydanov, T.R. Ohno, "Admittance Spectroscopy on CdTe Cells".

2. S.W. Townsend, T.R. Ohno, V. Kaydanov, A.S. Gilmore, " Hall Effect and Photoluminescence Studies of Cu Doped Films and Bias Degraded CdS/CdTe Cells".

January 27-28, 2000, NREL, Golden, Colorado

3. A.Gupta, S. W. Townsend, T. R.Ohno, V. Kaydanov, "Degradation of CdS/CdTe Solar Cells:
Cu/ZnTe/Au vs. Cu/Au Back Contact, Electrodeposited CdTe vs. First Solar CdTe",

4. T. R. Ohno, V. Kaydanov, R. T. Collins, A. Gupta, M. Herndon, U. Laor, "Grain Boundary Properties: Observations at the Colorado School of Mines".

5. V. Kaydanov, P. Meyers, "Some Possible Effects of Grain Boundaries on Thin Film Cell Performance",

May 6-7, 1999, NREL, Golden, Colorado

6. U. Laor, V. Kaydanov, T. Ohno, A. Gupta, B. McCandless," AC Characterization of Polycrystalline Thin Films,: Electrical Propeties of Intra-Grain and Grain-Boundary Material".

7. A.S. Gilmore, A. Al-Kaoud, T. Wen, V. Kaydanov, T.R. Ohno, J. Xi, " Mobility in SnO_2:F TCO Thin Films".

September 8, 1998, Adam,s Mark, Denver, Colorado

8. V. Kaydanov, T.R. Ohno, A. Al-Kaoud, A.S. Gilmore, "Characterization of Low Resistance and High Resistance Tin Oxide".

9. V. Kaydanov, T.R. Ohno, J. Tang, D. Morgan, " Analysis of the Back Contact Degradation Based on Minimum dV/dJ".

10. V. Kaydanov, "Possible Role of Electromigration in CdTe/CdS Solar Cells"

REPORT DOCUMENTATION PAGE

Form Approved
OMB NO. 0704-0188

Public reporting burden for this collection of information is estimated to average 1 hour per response, including the time for reviewing instructions, searching existing data sources, gathering and maintaining the data needed, and completing and reviewing the collection of information. Send comments regarding this burden estimate or any other aspect of this collection of information, including suggestions for reducing this burden, to Washington Headquarters Services, Directorate for Information Operations and Reports, 1215 Jefferson Davis Highway, Suite 1204, Arlington, VA 22202-4302, and to the Office of Management and Budget, Paperwork Reduction Project (0704-0188), Washington, DC 20503.

1. AGENCY USE ONLY (Leave blank)	2. REPORT DATE	3. REPORT TYPE AND DATES COVERED
	March 2002	Final Technical Report 15 May 1998 – 17 August 2001

4. TITLE AND SUBTITLE
Process Development and Basic Studies of Electrochemically Deposited CdTe-Based Solar Cells, Final Technical Report, 15 May 1998 – 17 August 2001

5. FUNDING NUMBERS
CF: XAK-8-17619-28
PVP25001

6. AUTHOR(S)
V.I. Kaydanov and T.R. Ohno

7. PERFORMING ORGANIZATION NAME(S) AND ADDRESS(ES)
Colorado School of Mines
Golden, Colorado 80401

8. PERFORMING ORGANIZATION REPORT NUMBER

9. SPONSORING/MONITORING AGENCY NAME(S) AND ADDRESS(ES)
National Renewable Energy Laboratory
1617 Cole Blvd.
Golden, CO 80401-3393

10. SPONSORING/MONITORING AGENCY REPORT NUMBER
NREL/SR-520-31777

11. SUPPLEMENTARY NOTES
NREL Technical Monitor: Bolko von Roedern

12a. DISTRIBUTION/AVAILABILITY STATEMENT
National Technical Information Service
U.S. Department of Commerce
5285 Port Royal Road
Springfield, VA 22161

12b. DISTRIBUTION CODE

13. ABSTRACT *(Maximum 200 words)* This report describes the long-term research and development issues related to polycrystalline thin-film solar cells. Our general research approach is based on combining activities aimed at improvement of cell performance and stability with activities aimed at increasing our fundamental understanding of the properties of materials making up the cells: CdTe, CdS, multi-layer back-contact, and transparent conducting oxide (TCO) front-contact. We emphasize the relation between structural and electronic material properties and various processing procedures, as well as the microscopic mechanisms responsible for the cell performance and its degradation. There is a lack of knowledge and understanding of basic issues behind the CdTe/CdS cell performance and stability, such as the nature and electronic properties of impurities and defects that control the majority-carrier concentration, mechanisms of the dopant compensation, recombination centers, their nature and properties, diffusion, electromigration and transformation of defects under various processing, stress, and operating conditions. We believe that better basic understanding of the specific influence of polycrystallinity, especially for fine-grain materials characteristic of CdTe-based cells, is now one of the most important issues we must address. We need to clarify the role of grain boundaries in forming the film electronic properties, as well as those of the p-n junction. It is important to study and understand the influence of the grain boundaries on the spatial distribution and migration of impurities and electrically active defects. To fulfill these tasks, one needs to develop new methods and techniques (or adjust existing ones) for material characterization, as well as develop more sophisticated approaches to data analysis and modeling.

14. SUBJECT TERMS: PV; polycrystalline thin-film solar cells; impedance spectroscopy; grain boundaries; space charge density; illumination intensity; transparent conductive oxides; near-field scanning optical microscopy; deep traps; carrier concentration profile; electromigration; cadmium telluride (CdTe)

15. NUMBER OF PAGES

16. PRICE CODE

17. SECURITY CLASSIFICATION OF REPORT	18. SECURITY CLASSIFICATION OF THIS PAGE	19. SECURITY CLASSIFICATION OF ABSTRACT	20. LIMITATION OF ABSTRACT
Unclassified	Unclassified	Unclassified	UL